Origami-inspired honeycombs as energy absorbing materials

Jianyu GAO

Lincoln College

A thesis submitted for the degree of Master of Science by Research

Department of Engineering Science

University of Oxford

Trinity Term, 2019

Abstract

Origami-inspired honeycombs as energy absorbing materials

Jianyu Gao, Lincoln College, Oxford

A thesis submitted for the degree of Mater of Science by Research in the Department of Engineering Science, University of Oxford. Trinity Term, 2019.

This thesis proposed a type of origami-inspired honeycombs for energy absorption. The major findings of this thesis were as follows.

First, a novel design of origami-inspired honeycomb with self-locking and stiffness gradient was proposed. The design used the concept of Miura-ori pattern to create the unique Miura-ori honeycomb, with a core layer being at the middle sandwiched by two secondary flange layers. The self-locking feature realized by the prior densification of the flanges increased the overall energy absorption whilst keeping the peak load low. It was found that properly designed honeycombs could reduce the peak force by more than 50% and meanwhile possess good specific energy absorption (SEA) in comparison with conventional square honeycomb.

Second, derivative Miura-ori-based honeycomb cores were used to create a family of hybrid origami honeycombs. Experimental and numerical results were presented to study the energy absorption capacity of the hybrid honeycombs. It was found that the hybridization could notably affect the peak load and SEA when compared to the individual cores that was constructed in the same form. Especially, it was seen that the hybridization built in a weak-strong-weak manner could reduce the peak force and meanwhile increase the energy absorption efficiency.

Third, the effects of dynamic loading on origami honeycombs were investigated numerically. The mechanical behaviors of derivative Miura-ori-based honeycombs, including the hybrid origami-honeycombs were studied under different compressive loading conditions. It was found that under dynamic loading condition, the hybrid origami-honeycomb with stiffness gradient in weak-strong-weak order could noticeably reduce the impact and transmitted force, and increase the energy absorption efficiency at the same time.

In conclusion, this thesis presented new paths for creating programmable energy absorbing materials with controllable mechanical properties.

Keywords: Origami, honeycomb, energy absorption.

Acknowledgements

I dedicate this work to those who have assisted and supported me during my Master research at the University of Oxford. First of all, my deepest gratitude goes to my supervisor Prof. Zhong You, for his constant encouragement and guidance. Without his patient instructions, insightful criticism and expert guidance, the completion of this work would not have been possible.

Secondly, I would like to express my heartfelt gratitude to all my friends from Lincoln College, Oxford, and those around the world. I want to thank them for their help, support and joyful company. Thank you for leaving me with all those sweet memories.

Most importantly, my thanks must be extended to my parents for their love and selfless support in all these years. Without them, I would never be able to come so far in my life.

Contents

List of Figures

List of Tables

Nomenclature

a	Pattern constant: zigzag side length.
a_k	Kink determining parameter.
b	Pattern constant: straight side length.
c_{el}	Elastic wave speed.
c, d	Elliptical curve scale parameters.
c_s	Shock speed.
d	The depth of the center of the material which carries the axial load.
e, g	Elliptical curve shift parameters.
f	Friction coefficient.
h	Height.
h_d	Crushing densification distance.
l_0	Honeycomb length.
m	Mass.
m_0	Mass of the graded honeycomb.
n	Number of the honeycomb layers.
t	Wall thickness.
u, v	Cartesian coordinate system for elliptical curve vertices.
v	Material Poisson's ratio, impact velocity,
v_y	Yield velocity.
w	Crush distance.
x	Deformed length.
A, A_0	Cross-section area.
B_s	Width of the strut cross section.

C	Core layer.
D	Half-length of the strut.
E	Young's Modulus.
E_d	Energy-absorbed by the graded honeycomb under dynamic load.
E_q	Energy-absorbed by the graded honeycomb under quasi-static load.
F	Flange layer.
G	Mass of the impinging plate.
H	Height of the strut cross section.
M	Bending moment.
M_p	Maximum bending moment, mass of projectile.
P	Crush force.
P_{avg}	Average force.
P_m	Mean crushing force.
P_{max}	Peak force.
R	Radius.
S	Elliptical arc length.
SEA	Specific energy absorption.
V , V_0	Impact velocity.
X_1, X_2, X_3	3D Cartesian coordinate system for pattern vertices.
σ	Engineering stress.
σ_y	Yield stress.
σ_d	Dynamic stress.
σ_{pl}	Quasi-static plateau stress.
σ_{avg}	Average yield stress.
Θ	Yield stress gradient.
ε	Engineering strain.

ε_d	Densification strain.
ϕ	Pattern constant: Sector angle.
ζ	Pattern constant: Edge angle.
η	Pattern constant: Side angle.
φ	Pattern constant: Elliptical curve gradient.
δ	Crushing distance.
δ_D	Densification crushing distance.
δ^E_{pinned}	Elastic crushing distance of pin-ended strut.
δ^P_{pinned}	Plastic crushing distance of pin-ended strut.
ρ, ρ_o, ρ_d	Density.
Ψ	Energy ratio.
Γ	Mass ratio.
λ	Density ratio.

Chapter 1

Introduction

1.1 Energy absorbing structures and materials

In the UK, the statistical data from the Department for Transport (2019) shows that there were 39.59 million vehicles licensed by the end of June 2019. Accompanied to it is more and more road accidents. According to the latest 2017 statistical annual report, there were 24,831 serious injuries and a total of 170,993 casualties in reported road traffic accidents in Great Britain alone (Department for Transport, 2018). With the objective of maximizing human safety, much research attention has been given to the design of more efficient energy absorbing structures and materials over the recent decades, in order to design and modify optimized future transport structures that can withstand impacts and crashes. The energy absorbing structure or material is a system that is capable to convert kinetic energy in a collision into other sort of energy so as to reduce the impact loads to a safe level. Energy conversion can be either reversible, like pressure energy in compressible fluids and elastic strain energy in solids, or irreversible (Alghamdi, 2001). The mechanisms of irreversible and collapsible energy absorbing systems involve utilization of friction, fracture, plastic deformation, metal cutting, extrusion etc. Common shapes of collapsible energy absorbing system include tubes, frusta, struts, sandwich plates and honeycomb structures.

1.2 Conventional honeycombs for energy absorption

The conventional honeycomb structures consist of an array of polygonal cells which nest together to fill a plane, epitomizing a cellular solid in two dimensions. The cells are usually in the shape of hexagons, but they can also be triangular, or square, or rhombic (Gibson and Ashby, 1997). Example sections are shown in Fig. 1.1.

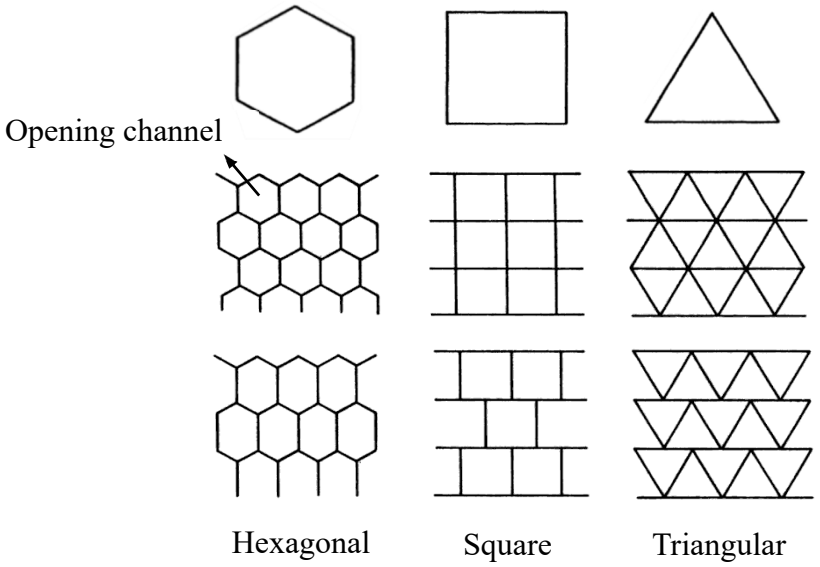

Fig. 1.1 Shapes of honeycombs

Due to their high stiffness to weight and high strength to weight ratio, the conventional honeycomb has been widely used in aerospace and automotive industry. They are also used as energy absorbing structures. For example, the feet of the Apollo 11 landing module used crushable aluminium honeycombs as shock absorbers (Gibson and Ashby, 1997).

Because of its wide applications, the energy absorption capacity of the conventional honeycomb has been widely assessed (Alghamdi, 2001; Baroutaji *et. al.*, 2017; Yu and Lu, 2003). It has been found that its energy absorption characteristics are not ideal when subjected to out-of-plane compression. (Note: the out-of-plane orientation refers to the direction parallel to the opening channel of the honeycomb, whereas the direction vertical to the opening channel of the honeycomb is often called as the in-plane orientation). A typical force-displacement diagram of a conventional honeycomb under out-of-plane compression is shown in Fig. 1.2. It is apparent that the maximum reaction force is substantially higher than the average force, hereby the load uniformity is bad. This could cause severe damage owing to the excessive force

transmission. To date, there is no report of how to modify the design of a conventional honeycomb of any shape in order to reduce the extrusive peak force whilst remaining effective in energy absorption capacity, which is why I have embarked on the mission of overcoming this particular issue by designing and creating innovative honeycombs inspired by the concept of origami.

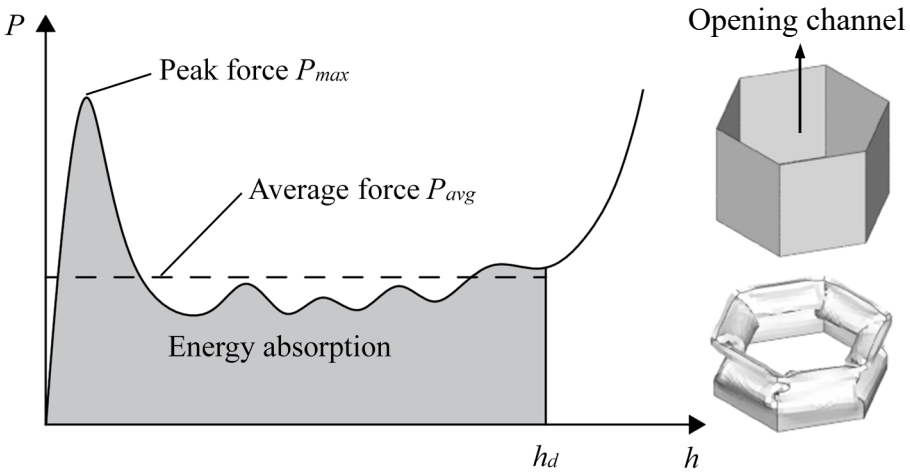

Fig. 1.2 Force-displacement curve of conventional honeycomb.

The idea of applying origami patterns to design high-performance energy absorbing devices is inspired by a well-known fact in structural engineering that structural properties critically depend on structural profiles. Through the pre-folding of a structure based on an origami folding pattern, e.g., pre-folding the vertical flat wall of a conventional honeycomb into a curved surface, a desirable failure mode with good load uniformity is expected to be achieved.

1.3 Aim, scope and layout

As mentioned previously, the load uniformity of conventional honeycomb is bad when it is subjected to out-of-plane compression. The present work aims to modify this deficiency by designing new types of honeycombs with good load uniformity whilst possessing the same or

higher specific energy absorption (SEA) when compared to the conventional honeycomb. To achieve this aim, the concept of origami was utilized to create novel origami-inspired honeycombs with graded stiffness features. The new designs have been validated by numerical analyses with the help of preliminary experimental studies.

This thesis is divided into six chapters starting with a general introduction as Chapter 1, which provides a brief background of the problem and its importance, followed by the aim and scope of the thesis and overview of the thesis structure.

A literature review is given in Chapter 2, which begins with a general description of research background and the design principles of energy absorbing structures. Typical structures and honeycombs used for energy absorption are then reviewed, followed by an overview of existing origami-inspired energy absorbing structures. Purposes of the presented work are finally identified.

Chapter 3 details the experimental study and the finite element analyses of the proposed Miura-ori honeycombs with self-locking and graded stiffness features. The creation of the FE model and mesh size study are all covered. Geometric effects on energy absorption efficiency are also discussed.

Chapter 4 covers the design, as well as the experimental and numerical study of derivative Miura-ori-based honeycombs. Hybrid origami-honeycombs with stiffness gradient are introduced. Parametric effects are studied and the structural influence of energy absorption efficiency is compared.

Chapter 5 presents the numerical analyses of various types of derivative Miura-ori-based honeycombs under dynamic compression with different velocities. Effort is made to find the possible best design for origami-inspired honeycombs under impact.

Chapter 6 summarizes the findings from the present work and suggests further research that may be conducted in the future which was not covered in the scope of the present thesis.

Chapter 2

Literature review

In the past decades, with the promotion of safety awareness, energy absorbing structures and materials are greatly developed with the aim of minimizing main structural failure and economic loss in a collision. The energy absorbing structures have their applications ranging from buildings and bridges, mines, transport vehicles such as trains, cars, aircraft and ships, to energy harvesting facilities. A lot of research has been conducted to study the energy absorption abilities of structures and materials. According to the loading condition, the research work can be divided into two categories: one under (quasi) static loading and the other under dynamic loading.

Quasi-static loading refers to loading where inertial effects are assumed to be negligible. Thus, time and inertial force are ignored. Such assumption is also valid when the impact speed is low. In quasi-static process, the negligence of inertial effects highlights the influence of structural configuration, as well as reduces the difficulties in theoretical and experimental analysis. Meanwhile, static analysis also serves as the fundament for dynamic analysis.

On the other hand, under dynamic loading condition, the load is applied at high speed. When the structure is subjected to impact, one portion of the structure is stressed while the other portion may not experience any stress as the stress wave travels through the structure. Thus, dynamic deformation involves wave propagation, whereas quasi-static deformation can be considered as a sequence of equilibrium states. Several theoretical methods for dynamic

crushing use the simplified rigid–plastic method of analysis, which often yields good agreement with experimental results (Jones, 1989).

2.1 General design principles of structures for energy absorption

Energy absorbing structures are designed to protect the main structures or installations during an impact. A large family of such structures are thin-walled structures in which the thickness is much smaller than other structural dimensions. These structures absorb kinetic energy by undergoing large plastic deformation when subjected to an impact loading. There has been in-depth research on thin-walled energy absorption structures (Alghamdi, 2001, Baroutaji *et. al.*, 2017, Ma, 2011, Muhammad, 2007). A summary of the typical examples are given by Yu and Lu (2003).

The performance of an energy absorbing structure is commonly assessed by the displacement vs. force diagram such as that shown in Fig. 2.1. In general, an ideal energy absorbing structure should possess following properties (Yu and Lu, 2003):

1) *Irreversible energy conversion*

   Energy absorption structures should convert kinetic energy to inelastic energy to avoid elastic snapback.

2) *Restricted and constant reaction forces*

   A low peak force limits peak acceleration, and a constant average force that avoids high rates of deceleration.

3) *Long stroke*

   Long crush displacement leads to an increase work done by the energy absorbing structures.

4) *High SEA*

5) *Stable and repeatable deformation mode*

Generally impacts involve uncertain external loads, so energy absorbing structures must work reliably across range of loading conditions.

6) *Low cost and ease of installation*

Typically energy absorbers are single-use devices, and need to be replaced after every accident.

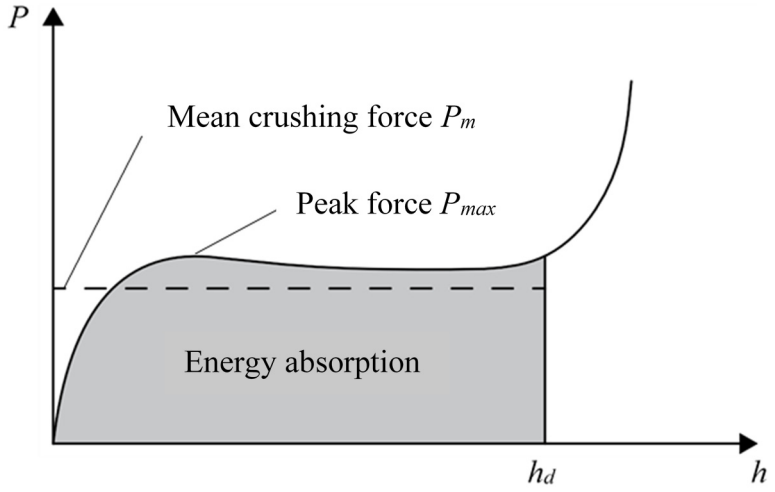

Figure 2.1 Desirable load-displacement curve for energy absorption.

In essence, an ideal energy absorbing structure should have a high mean crushing force P_m paired with a long stroke prior to reaching the densification region h_d in order to absorb a maximum amount of impact energy ($\approx P_m h_d$), and meanwhile a low maximum peak force P_{max} relative to P_m. The ratio between P_{max} and P_m is known as the load uniformity.

2.2 Structures for energy absorption

Design of sophisticated energy absorbing structures usually involve thin walled structure, in which the thickness is much smaller than its in-plane geometries. These structures are subjected to predominantly compressive loads during impact, and they can undergo large deformation that may exceed the associated wall thickness by two orders of magnitude (Alghamdi, 2001). Common thin walled structures used in energy absorbing structure design can be categorized

into steel drums, circular tubes, corrugated tubes (Elgalai, *et al*., 2004), multi-corner columns (Wierzbicki and Abramowicz, 1983), frusta, honeycomb cells (Hu and Yu, 2013), sandwich plates (Fathers, *et al*., 2015, Gattas and You, 2015, Gattas, *et al*., 2016) and some other special shapes such as stepped circular thin-walled tubes (Zahran, *et al*., 2017), graded cellular structures (Ajdari, *et al*., 2011) and their variants (Alghamdi, 2001). Their failure modes, include inversion (Chirwa, 1993), splitting (Stronge, *et al*., 1983), lateral indentation (Ma and You, 2013), lateral flattening and axial crushing (Zhang, *et al*., 2007).

2.2.1 Tubes

Thin tubes are the most widely used collapsible impact energy absorbers because of their structural simplicity. Common deformation modes for tubes include inversion (turning inside out or outside in), splitting (a special case of tube inversion where the die radius is large enough to cause the wall of tubes to split instead of inversion) (Al-Hassani, *et al*., 1972), lateral indentation, lateral flattening, and axial crushing (axial loading especially for cylindrical shell) (Alghamdi, 2001). The research was first focused on conventional tubes with circular and polygonal sections, and then some variants of tubes were introduced. Under quasi-static loading condition, inspired by corrugated design, Elgalai, *et al*. (2004) investigated the crushing behaviors of axially crushed corrugated tubes made of carbon fiber/epoxy composites. The absorbed energy per unit mass (property 4 in section 2.1) was found to be very sensitive to the increase in corrugation angle. However, the corrugation angle tends to decrease the initial crush failure load. Optimum selection of corrugation angle should balance these two aspects. Besides the axial loading mode, lateral loading mode is also a common impact mode in reality. Gupta and Abbas (2000) studied the quasi-static lateral crushing of composite cylindrical tubes between flat platens. The properties of peak force and absorbed post-collapsed load (property 2 in section 2.1) are investigated theoretically and experimentally in their paper.

Under dynamic loading condition, Karagiozova and Jones (2000) studied the effects of material properties, shell geometry, boundary and loading conditions on energy absorption and failure modes of tubes. It is reported that the development of the buckling shape depends strongly on the inertia properties of the striker and on the geometry of the shell. Karagiozova and Jones (2002) also found that a high velocity impact caused an instantaneously applied load initially with a maximum value, and whether this load caused an inelastic collapse depended on the magnitude of the initial kinetic energy. Using the finite element method (FEM), Tai, *et al*. (2010) calculated the energy absorption characteristics of tubes under axial loading, in which the effect of dynamic impact on the strain rate was also included. Chen and Ushijima (2011) investigated the effect of material properties, geometry and impact velocity on the peak load of the tube when subjected to axial impact. The plastic buckling of tubes under axial impact was investigated theoretically by Wang and Tian (2008), two types of loading were studied and the results of shortening, time duration, half-wave number and buckling shape of tubes were reported. Rajabiehfard, *et al*. (2016) studied the dynamic behavior of uniform thickness, stepped thickness and functionally graded thickness tubes under dynamic axial impact experimentally and numerically. It was found that in comparison with uniform thickness tube, the stepped thickness and functionally graded thickness tubes absorbed the same amount of energy with lower peak force.

2.2.2 Sandwich panels

Usually, a sandwich structure is constructed from a core with a skin attached to each side, and is analogous to an I-beam, where the core represents the web and the skin represents the flanges. A wide range of material options for skins and cores offer considerable flexibilities for designers. In 1970's, Gilkie and Sundararaj (1971) studied the effect of: (1) laminate thickness; (2) foam core thickness; (3) face thickness; and (4) support span on the impact strength of the sandwich. Some tests were also conducted on glass fiber laminates to provide a comparison.

They reported that sandwich panels were substantially more resistant to impact failure than simple laminates. After the development of several decades, sandwich structures are still popular in design of energy absorbers. Fan, *et al*. (2011) conducted an experimental investigation on the lateral compression of sandwich tubes made of aluminum alloy and foam. Three types of deformation modes were observed in the lateral collapse of sandwich tubes as follows: sequential collapse pattern, simultaneous collapse pattern, and simultaneous collapse pattern with fracture of the foam core. The results showed that sandwich tubes have enhanced crush strength and energy absorption behavior (property 2 in section 2.1).

Xue and Hutchinson (2003) pointed the fact that metal sandwich plates with sufficiently strong tetragonal truss cores are able to sustain substantially larger blast loads than monolithic solid plates of the same material and total mass. Nemat-Nasser, *et al*. (2007) carried out a series of experiments to investigate the dynamic response of various essential components of a class of sandwich structures with metal foam, under high-rate inertial loads. The variation of the localized deformation versus impact velocity is investigated experimentally and numerically. In addition to mechanical loadings, Xie, *et al*. (2017) studied the effects of thermal loading (temperature ranging from 22°C to 866°C) on honeycomb sandwich panels.

2.2.3 Structures with property gradient

Recently, energy absorption structures with graded (density, geometry, stiffness, *et al*.) design have been investigated to meet the engineering requirements. Liu, *et al*. (2015) developed a theoretical model for the shock front propagation in a density graded cellular rod (foam). Their study suggests a possibility to reduce the maximum impact stress (property 2 in section 2.1) transmitted to the impacted structures using a proper density gradient. Pang, *et al*. (2017) introduced the design and optimization of functionally graded tapered tube (FGTT) with variable diameter, which show of great advantages on energy absorption over the

conventionally straight/tapered circular tubes under the same weight (property 4 in section 2.1). Rawat, *et al*. (2017) simulated the collapse behavior and energy absorption in elliptical tubes with functionally graded corrugations. The simulations showed exiting reduction of 72% peak force (property 2 in section 2.1) as compared with conventional elliptical tubes. Ying, *et al*. (2017) fabricated and analyzed thin-walled square column made of hot stamping high strength steel with functionally graded strength (FGS), whose wall strength varies along the axial direction with a specific gradient, and excellent crashworthiness have been obtained.

2.3 Foams for energy absorption

Foam materials are cheap and commonly used for energy dissipation purposes due to their ideal specific strength and energy absorption capabilities (Ashby, 2000). Unlike conventional honeycombs, the force-displacement response of foam under compression is always uniform due to the continuous failure at the micro-scale of individual foam ligaments (Gibson and Ashby, 1997). Numerous studies have been conducted to investigate the energy absorption capacity of the foam. Yamada, *et al.* (2005) addressed the energy absorption capacity of foam-filled aluminium tubes, and they discovered that the energy absorption of the foam filled tubular structure was improved significantly. Zheng, *et al.* (2011) investigated the foam panels as energy absorption devices attached to the aircraft fuselage. Sun, *et al.* (2018) studied the low-velocity impact behavior of sandwich panels with stepwise graded foam cores, and they found that the critical impact energy required to cause failure to the front facesheet increased with the density of first foam core layer. Liu, *et al.* (2019) proposed an effective strategy to enhance the energy absorption and impact resistance capacities of foam materials by adding density-gradient. Wang, *et al.* (2020) conducted the computational analysis and optimization of sandwich panels with foam cores for blast resistance, and they found that the foam core with descending gradient of layer density across the thickness direction provided the highest blast resistance. However, it should be noted that it is hard to design and control the energy

absorption capacity of foam since it is very difficult to control the cell size distribution and morphological parameters of foam in foam making (Crupi, *et al.*, 2013). But for honeycombs, exact geometries of cell structures can be defined, and thus the energy absorption capacity of honeycombs can be easily controlled in manufacturing. As a result, by redesigning the unit cells of honeycomb, it is possible to create novel honeycombs with good load uniformity, high SEA and controllable quality.

2.4 Honeycombs for energy absorption

2.4.1 Conventional honeycombs for energy absorption

Santosa and Wierzbicki (1998) reported that under quasi-static loading condition, using aluminum hexagonal honeycomb core is more weight efficient than using aluminum foam filling (property 4 in section 2.1). It was also reported that the hexagonal honeycomb-filled tube absorbs higher SEA than the aluminum foam-filled tube under the bending loading (Santosa and Wierzbicki, 1999). By experimental and analytical approaches, Papka and Kyriakides (1999a, 1999b) investigated the uniaxial and bi-axial crushing behavior of polycarbonate honeycomb with circular cells in a hexagonal arrangement. In their analytical paper (Papka and Kyriakides, 1999b) the energy absorption capacity of honeycomb structures was predicted to have good accuracy.

Hu, *et al*. (2015) found that circular-celled honeycombs are less sensitive to the impact velocity comparing with tube structures, but they have a higher dynamic SEA. Similar to the cases of quasi-static loading, its energy absorption ability is also related to its cell configurations including wall thickness (Zhang, *et al*., 2014), central angle (Zhang, *et al*., 2014), thickness to edge length ratio (Xu, *et al*., 2012), and specimen dimensions (the amount of cells) (Xu, *et al*., 2012). Based on the collapse behavior of the hexagonal honeycombs revealed from the

numerical simulations, Hu and Yu (2013) established an analytical model to deduce the crushing strength of the honeycomb and the stress at the supporting end both as functions of impact velocity, which has been validated by simulations. Wang, *et al*. (2014) studied the velocity sensitivity for the hexagonal honeycomb cells via a series of experiments with impact velocity varying from 20m/s to 80m/s. They also studied the influences of structure geometries (honeycomb density) on its energy absorbing ability. Yasui (2000) investigated the dynamic impact crushing behavior of multi-layer hexagonal honeycomb sandwich panels and the impact tensile loading behavior of their material members experimentally. It is reported that, crushing for multi-layer honeycomb sandwich panels was observed to occur after the appearance of a stress peak in each layer; the stress peak and subsequent collapse progressed through the layers over time.

2.4.2 Graded honeycombs for energy absorption

Recently, (Shen *et. al.* 2013a) studied the behavior of the graded hexagonal honeycomb under in-plane dynamic load using the FEM. The superficial graded honeycomb, shown in Fig. 2.2, was designed to have a non-dimensional gradient

$$\Theta = n\frac{\Delta\sigma_y}{\sigma_{avg}} \tag{2.1}$$

where n is the number of the layers, $\Delta\sigma_y$ is the difference of the material's yielding stress between two adjacent layers, and σ_{avg} is the average yielding stress of the honeycomb block.

Shen *et.al.* (2013a) examined two loading cases. In the first case, a constant velocity was applied to the impact plate which then crushed the honeycomb. Two types of gradients were considered: one being the positive constant gradient indicating the weakest cell at the impinged end, and another the negative constant gradient with the strongest cell at the impinged end. They found that the reaction stresses at the supporting and loading ends were almost the same

under the low velocity impact regardless how the honeycomb was placed. However, under the high velocity impact, when Θ was positive (weaker end is the impinging end), the dynamic stress obtained from the loading end was marginally higher than that on the supporting end, which was equal to the quasi-static plateau stress. When Θ was negative (weaker end is the supporting end), the stress at the loading plate was much higher than that at the supporting plate due to the inertial effect. The stresses decreased with the increase of the displacement because the collapse occurred from the loading end with strong material to the supporting end with weak material. However, the overall energy absorption in both conditions remained more or less the same.

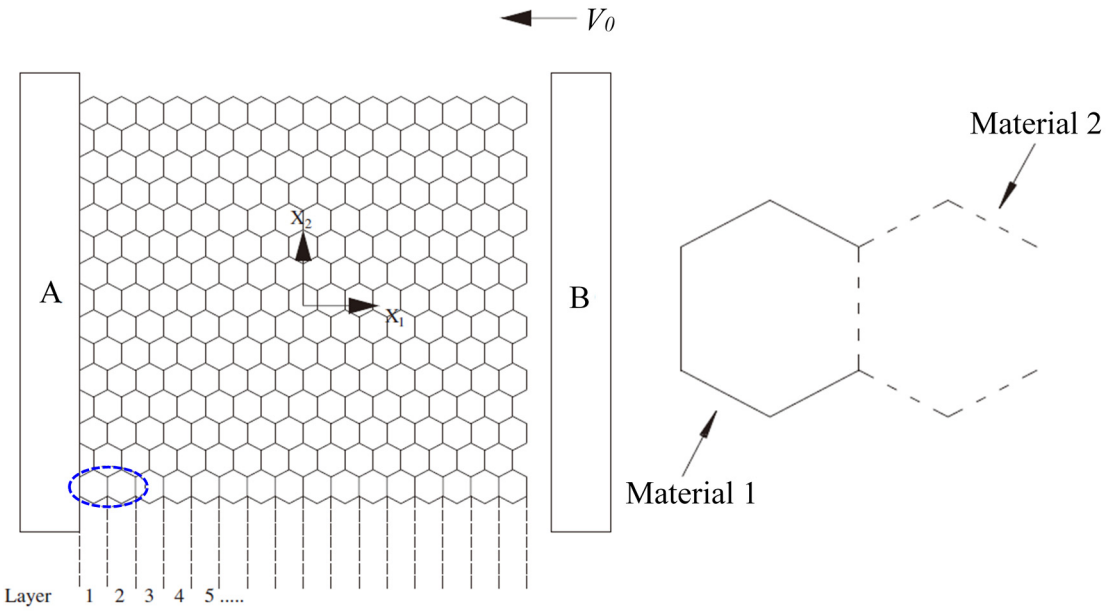

Figure 2.2 The superficial graded honeycomb (Shen *et. al.* 2013a).

In the second case, an initial densification velocity was applied to the impact plate which then crushed the honeycomb. In this case, when the velocity of the impact plate decreased to zero, the graded honeycomb became fully crushed. Both positive and negative gradient were also considered. Analytically, they derived the energy ratio ψ for the graded honeycomb as:

$$\psi = \frac{E_d}{E_q} = 1 + \frac{1}{2\Gamma} + \frac{1}{12\Gamma}\Theta \tag{2.2}$$

where E_d is the energy-absorbed by the graded honeycomb under dynamic load and E_q is that under quasi-static load, $\Gamma = G/m_0$, G is the mass of the impinging plate and $m_0=\rho_0 l_0 A$ is the total mass of the graded honeycomb, ρ_0 is the density, l_0 is the total length and A is the in-plane area of the graded honeycomb, respectively. It was found that the positive gradient could enhance the energy absorption capacity.

This particular piece of research demonstrates that the graded materials can be used not only to alter the reaction forces but also to enhance energy absorption capacities. The adjustment of the force exerted on the supporting end can be utilized to better protect the structure behind the supporting end. However, the superficial graded honeycomb examined by Shen *et. al.* (2013a) cannot be made in practice.

Shen, *et al*. (2013b) also studied the gradient effect of the graded cellular rod under impact loading using wave theory. Analytical expressions for the dynamic response of the graded cellular rod were theoretically derived using the one-dimensional shock wave theory. They showed that when the gradient was positive, the energy absorption of the rod was enhanced, which was consistent with the FE simulation results. Karagiozova and Alves (2015) made a theoretical analysis of the propagation of stress waves in cellular solids with non-uniform density under impact loading. Numerical simulations were carried out to verify the predictions of the theoretical analysis. Attention was paid to the energy absorption capacity of the materials depending on their initial density distribution when comparing their dynamic responses to the response of equivalent mass cellular block with uniform density. It was shown that the density variation had a significant effect on the history of the stresses and strains during the compaction process.

2.5 Origami-inspired structures and materials for energy absorption

2.5.1 Utilization of origami in energy absorbing structures and materials

Origami, the ancient art of paper folding, has now extended far beyond the art itself. Today, origami is applied to a wide range of engineering applications, ranging from surgical tools to deployable solar panels in space. With numerous unique folding patterns, origami has also been widely used in the design of energy absorbing structures. The most noticeable origami-inspired energy absorbing structure is the origami crush box (Ma, 2011). The origami tube is created by pre-folding a thin-walled square tube using a specific origami pattern, as shown in Fig. 2.3(a) and (b). In comparison with the square tube, the pre-folded corners reduce the peak reaction force when the tube is subjected to axial compression, extend the plastic deformations into most surface area of the structure and sustain a higher average reaction force when the tube is compressed. It channels the tube to a particular failure mode associated with a higher SEA. A comparison amongst the performances of the square tube and two designs of origami tubes is given in Fig. 2.3(c). It has been found that the origami tube with the complete diamond failure mode can achieve both over 50% increases in the mean crushing force and about 30% reduction in the peak force in comparison with those of a conventional square tube with identical surface area and wall thickness.

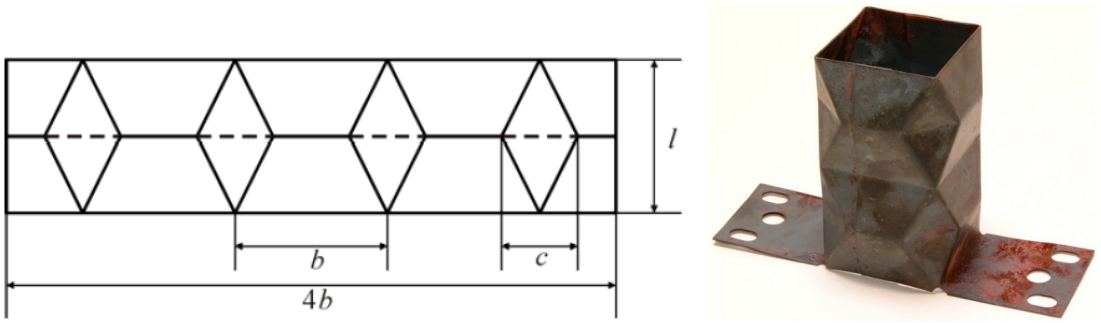

(a) (b)

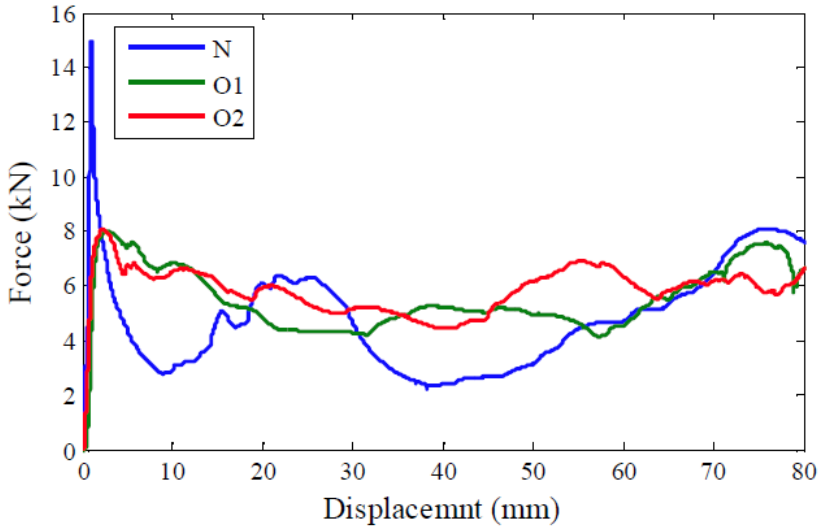

(c)

Fig. 2.3 Origami tube: (a) Origami pattern of a layer of the thin-walled square tube; (b) the origami tube; (c) displacement vs force curves of conventional (N) and origami (O1, O2) square tubes, where O1 and O2 relate to two different *c* values.

Based on traditional open-section structures, Li and You (2014) developed the beam structures with developable origami patterns which have a 20% higher SEA. Ma and You (2013a) also created the thin-walled beams with pre-folded origami design which has a better performance in the case of lateral collapse. Compared to beam structures, tube structures are more common in engineering applications. Zhang, *et al*. (2007) introduced origami design into tube structures to increase their energy absorption in the situation of axial compression. Song, *et al*. (2012) combined the thin-walled structures with origami patterns to reduce the undesirable high peak force at the initial of crushing. By parametric analysis, the relationships between the geometry design (pre-folding angle) and the initial peak force as well as the mean crushing force for the tubes with different cross-sections have been illustrated. Furthermore, Ma, *et al*. (2016) successfully extended this design concept to rigid origami energy absorbing structures. Straight-crease design are widely used in origami crush box, so in aforementioned literatures. Garrett, *et al*. (2016) introduced the curved crease design, as shown in Fig. 2.4, to the pre-folded

shape of the tube. By analytical and experimental analysis, Yang, *et al*. (2016) investigated the influence of the tube thickness on the energy absorption of the origami structures.

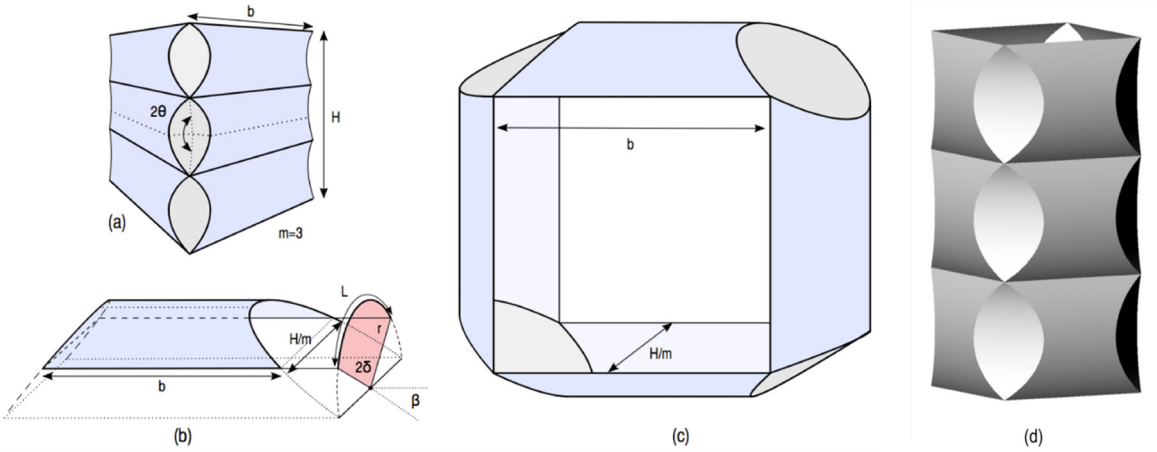

Fig. 2.4 Geometric specification of the curved crease origami tube: a) Complete tube; (b) Geometry of module wall; (c) Single tube module; (d) Tube composed of three modules (rows) (Garrett, *et al*., 2016).

Zhou, *et al*. (2015) presented the geometric design and mechanical properties of cylindrical foldcore sandwich structures. Zhou, *et al*. (2016) also carried out dozens of dynamic tests on thin-walled tubes including conventional square tubes and two types of origami crash boxes. Being validated by experiments, origami crash boxes perform better than the conventional square tubes. Li and You (2015) proposed a new origami foldcore design for a multi-corrugated indented foldcore sandwich panel used in energy absorption. Gattas and You (2015) studied the geometric assembly of rigid-foldable morphing sandwich structures and also did some analytical and experimental work to study the energy absorption performance of curved crease foldcore under low-velocity impact. The experimental analysis suggested that the complete diamond collapse mode is also more efficient in the case of impact loading. Furthermore, Gattas and You (2014a) introduced the indented foldcore into the geometry design and gained a better energy absorption performance.

2.5.2 Manufacturing techniques

An important feature of origami structures is that they are deployable and can be folded from a flat sheet without stretching of the material along the folding lines. Therefore, they can be formed by only using low-energy bending operations. Moreover, many patterns are rigidly foldable and can be folded without bending of the facets. Some manufacturing methods have been developed for origami-inspired structures in recent years.

- **Stamping**

Stamping has been a commonly used method to create metal sandwich panel cores, and it has also been adopted to fabricate origami-inspired structures. Gattas and You (2014a) used a single punch stamping method to manufacture the indented origami foldcores. Male and female steel dies were fabricated and mounted on a mechanical punch press. The aluminium sheet were place between the dies and stamped into the folded configuration, as shown in Fig. 2.5.

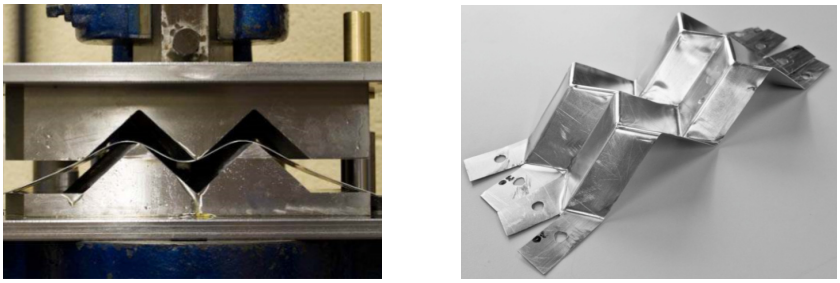

(a) (b)

Fig. 2.5 Stamping technique: (a) Stamping process; (b) stamped specimen.

- **Pattering and Gathering**

Another method for the continuous production of origami folded cores for sandwich panels is a two-step Pattering and Gathering method (Zakirov, *et al.,* 2006), as indicated in Fig. 2.6 (a) and (b). First, the pattering rollers emboss the folding pattern on the sheet material. Then, the foldcore is formed by the gathering roller. Zakirov, *et al.* (2010) used this technique and successfully manufactured the Miura-ori patterns, as shown in Fig. 2.6 (c) and (d).

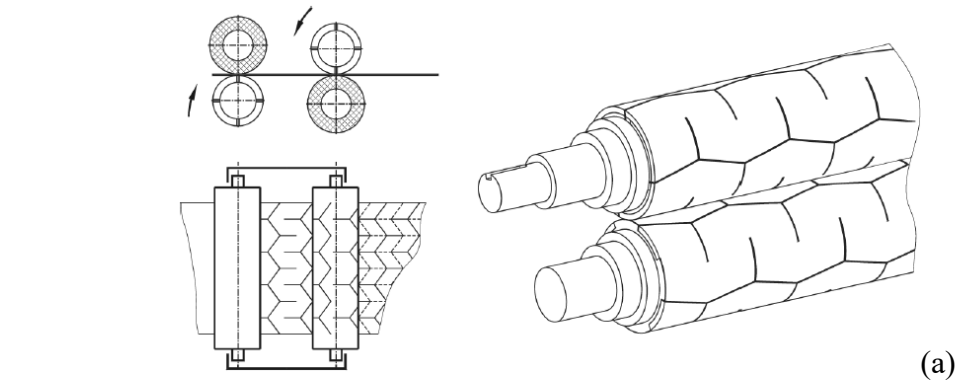

(a)

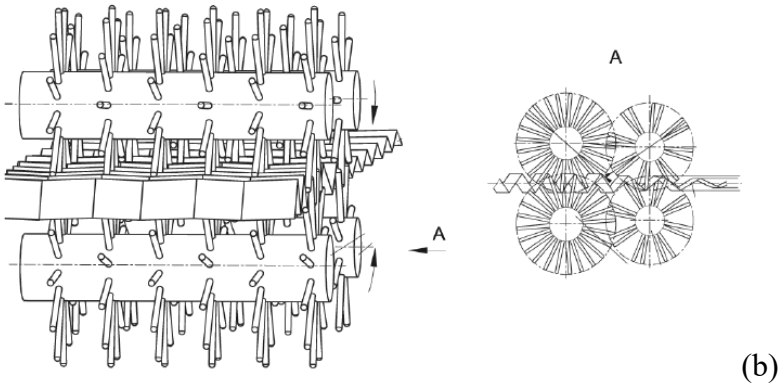

(b)

(c)

(d)

Fig. 2.6: Pattering and Gathering technique: (a) Demonstration of Pattering; (b) demonstration of Gathering; (c) & (d): demonstration of Miura-ori pattern been generated by Pattering and Gathering technique.

- **3D printing**

The traditional manufacturing techniques mentioned above are only effective in fabricating simple folding models and the geometric imperfections introduced during those processes have a significant detrimental effect on the load carrying capacity of the foldcores (Baranger, *et al.*, 2011). With the development of modern technology, more accurate and complex origami foldcores can be manufactured by 3D printing technique, which is also called as additive

manufacturing (AM). Common 3D printing techniques include: Material extrusion, Vat polymerization, Material jetting, Binder jetting and Power bed fusion. The most revolutionary 3D printing technique is metal 3D printing, and the Selective Laser Melting (SLM) process is commonly used for additive metal forming. During the SLM process, it uses a laser to scan and selectively melt the granular metal powder particles, and then the melted particles will be bonded together and a metal part will be built layer-by-layer. When the building process is finished, a post-processing procedure is often necessary in order to improve the mechanical properties, accuracy, and appearance of the printed metal specimen. Common post-processing steps include the removal of the supporting structures and thermal annealing which is used to relieve the residual stresses and improve the mechanical properties of the specimen. Nowadays, 3D printing technique has been commonly used to fabricate complicated structures for experimental purposes. Yang, *et al.* (2016) successfully validated the finite element models by using 3D-printing origami brass tubes (Fig. 2.7 (a)). Yang, *et al.* (2018) used 3D printed origami-patterned quadruple-cell tubes to validate relevant simulation results. Bates, *et al.* (2016) 3D printed polyurethane honeycombs and studied their repeated tailored energy absorption capacity (Fig. 2.7 (b)). Duan, *et al,* (2018) investigated the enhanced out-of-plane compressive strength and energy absorption of 3D printed square and hexagonal honeycombs with variable-thickness cell edges.

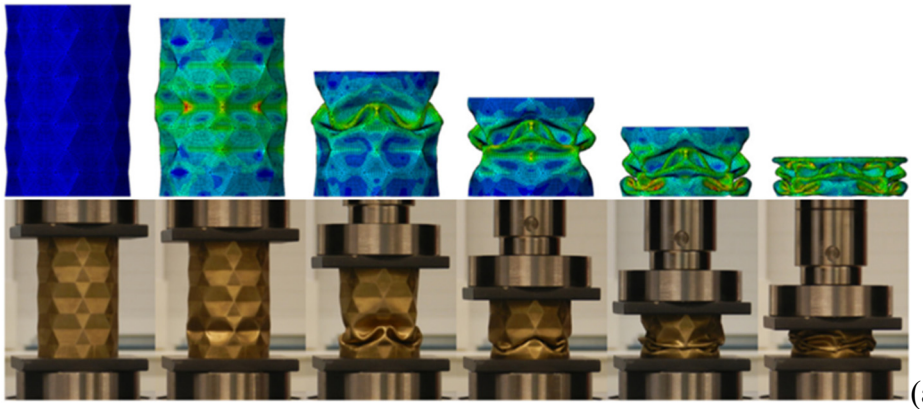

(a)

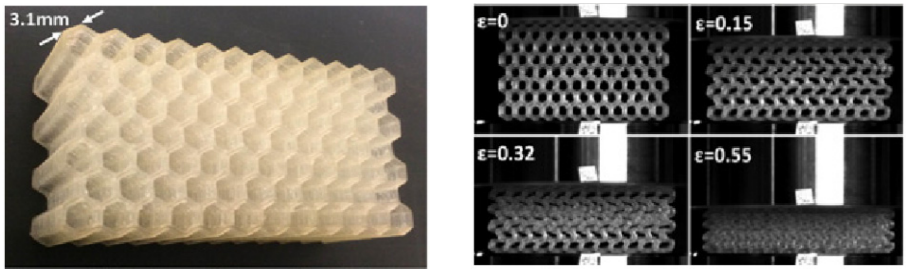

(b)

Fig. 2.7 3D printed test specimens: (a) 3D-printed brass tube; (b) 3D printed polyurethane honeycomb.

The above literatures have shown that the 3D printing technique is not only capable of manufacturing origami-inspired models, but also feasible of fabricating origami-inspired energy absorbing structures for experimental study. However, the cost of 3D printing is generally high at the moment. In the present work, the designs of origami-inspired honeycombs are quite complicated. It is difficult to accurately fabricate these origami honeycombs by using traditional manufacturing methods. Hence, the 3D printing technique was adopted for the fabrication of all experimental specimens in the present work.

2.6 Summary

The literature review above is confined to the application of energy absorbing structures and materials. The past work has shown that the structural performance can be programmed by introducing suitable configurations of origami structures. For example, the incorporation of diamond folds in the corners of thin-walled square tube can greatly increase its energy absorption capability when subjected to axial compression. This has prompted me to think that by adopting various existing origami concepts, origami-inspired honeycombs with programmable properties can be designed in order to achieve better energy absorption performance.

Chapter 3

Miura-ori honeycomb

In this chapter, the design of a novel origami-inspired tetragonal honeycomb has been proposed as an energy absorbing material. It uses the concept of Miura-ori pattern to create the unique origami- honeycomb, with the core layer being at the middle and two secondary flange layers being at the top and bottom, respectively. The Miura-ori honeycomb not only has the connectivity with open channel within the material, but also has the self-locking feature realized by the prior densification of the flanges. The self-locked flanges at both ends of the core layer are similar to the bamboo joints and also play important roles of increasing energy absorption capacity of the honeycomb.

3.1 Geometric design

3.1.1 Origami pattern

The Miura-ori origami honeycomb is designed using the Miura origami pattern (also known as the Miura-ori). Its pattern is shown in Fig. 3.1 (a), the dashed and dash-dotted lines represents hill and mountain folds, respectively. The middle section is called the core layer, and the other two sections are called flange layers. A specific restriction has been assigned to the sector angles that the value of angle ϕ_c is always larger than ϕ_f.

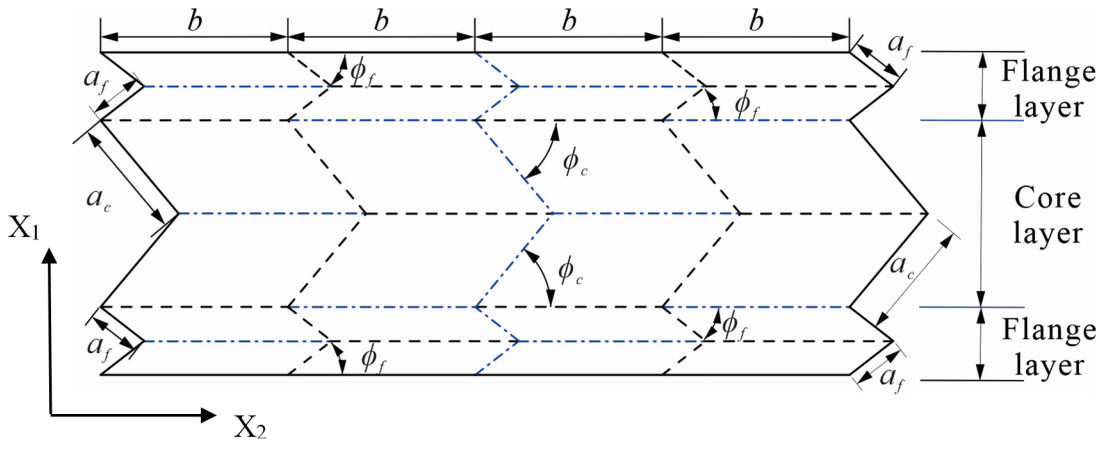

(a)

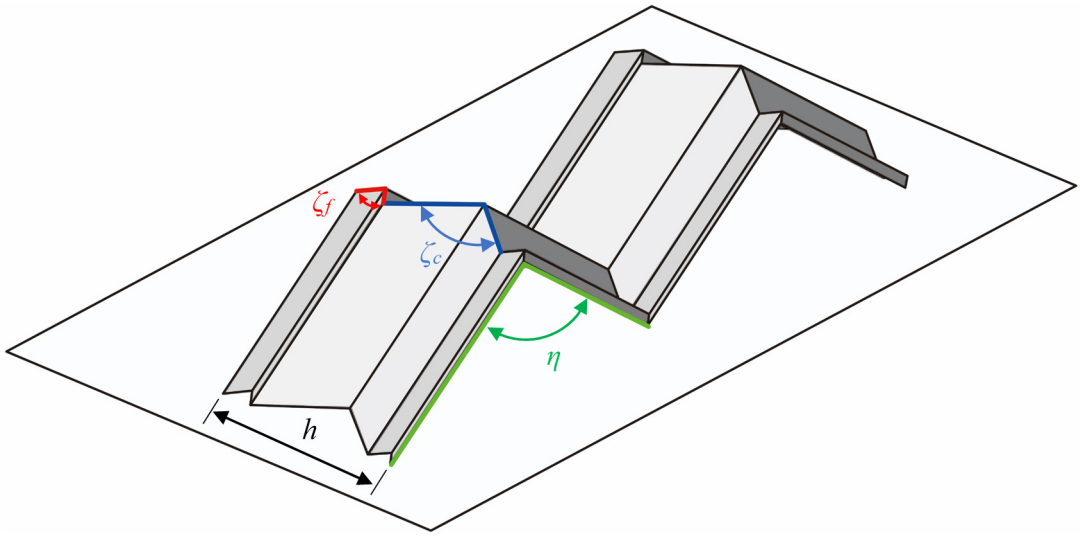

(b)

Fig. 3.1 Geometric design: (a) Miura-ori honeycomb pattern; (b) a piece of folded pattern.

Folding the sheet according to the above design gives a piece of folded object as shown in Fig. 3.1 (b), and the relationship between its 3D geometrical parameters and the pattern can be expressed and determined by the following equations (Gattas, *et al*., 2013). In addition, Eq. (3.1) is a general equation which can be adopted for both core and flange layers.

$$(1+\cos\zeta)(1-\cos\eta)=4\cos^2\phi \tag{3.1}$$

$$h=2a_c\sin(\zeta_c/2)+4a_f\sin(\zeta_f/2) \tag{3.2}$$

By folding four pieces of same-sized patterns to the same extent and connecting the ridges, as shown in Fig. 3.2 (a), a Miura-ori honeycomb unit can be established. A single tetragonal cell in this unit is called a Miura-ori honeycomb cell, as shown in Fig. 3.2 (b).

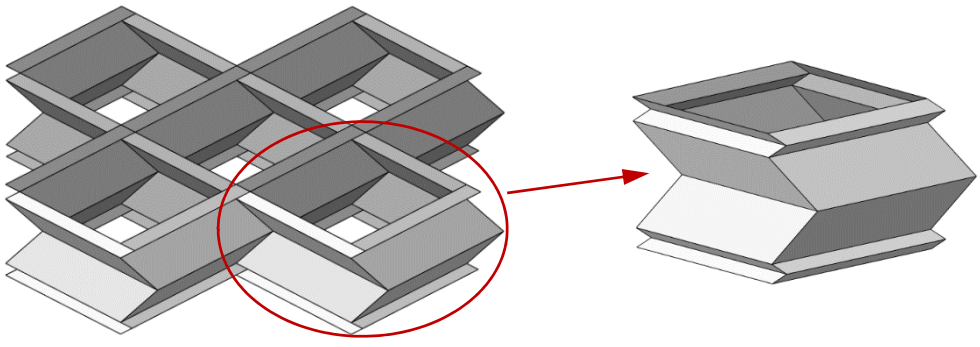

(a) (b)

Fig. 3.2 Miura-ori honeycomb: (a) Miura-ori honeycomb unit; (b) Miura-ori honeycomb cell.

In pure mechanism analysis, it is assumed that the facets divided by the folding lines in the Miura-ori honeycomb pattern are all thin rigid bodies, and all the creases are frictionless hinges. Thus, under this ideal condition, the Miura-ori honeycomb unit can be folded and deployed from a completely flat sheet, as illustrated in Fig. 3.3.

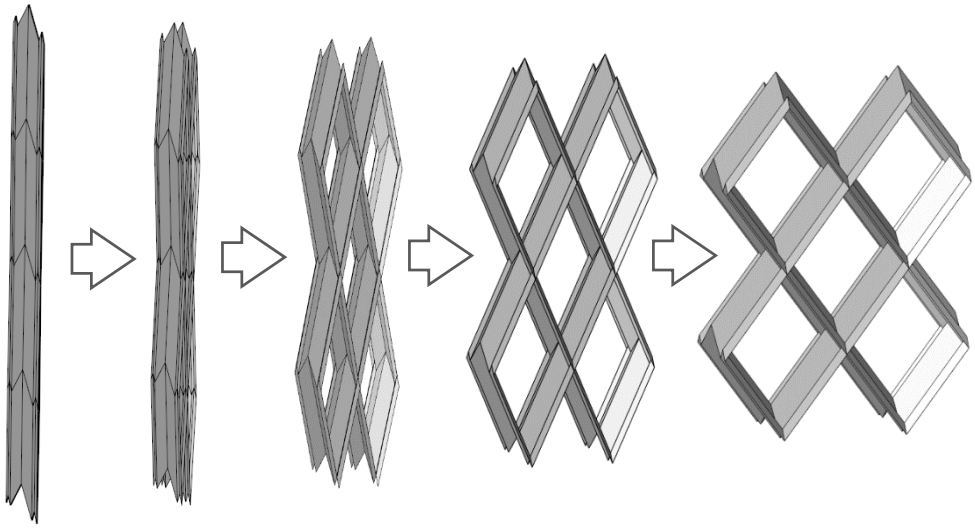

Fig. 3.3 Deployability of the Miura-ori honeycomb.

3.1.2 Self-locking

Due to the flat-foldable nature of the Miura-ori and its characteristic of 1 degree of freedom (DOF) (Miura, 1972), a single Miura-ori can be folded from the state of a completely flat pattern to another fully flat state after folding, as shown in Fig. 3.4.

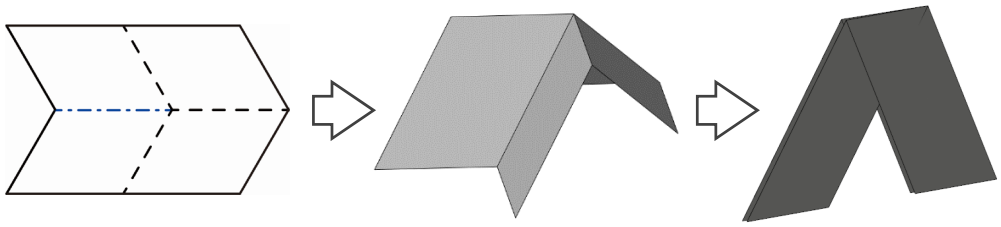

(a) (b) (c)

Fig. 3.4 Deployability of the Miura-ori fold: (a) A piece of flat sheet with pre-determined Miura-ori pattern; (b) a partially folded Miura-ori at certain extent; (c) a completely folded Miura-ori.

In the design, the value of angle ϕ_f is always smaller than angle ϕ_c. In this case, it can be proved that since ϕ_f and ϕ_c are constrained by $0 < \phi_f < \phi_c < \pi$, from Eq. (3.1), we have

$$\frac{1+\cos\zeta_f}{1+\cos\zeta_c} = \frac{\cos^2\phi_f}{\cos^2\phi_c} > 1 \tag{3.3}$$

Or

$$\zeta_f < \zeta_c \tag{3.4}$$

Therefore, when ζ_f reaches *0*°, the core layer will always remain un-flattened, as shown in Fig. 3.5. Thus, the flange layers will always be flattened prior to the core layer during the folding process. This phenomenon is called self-locking.

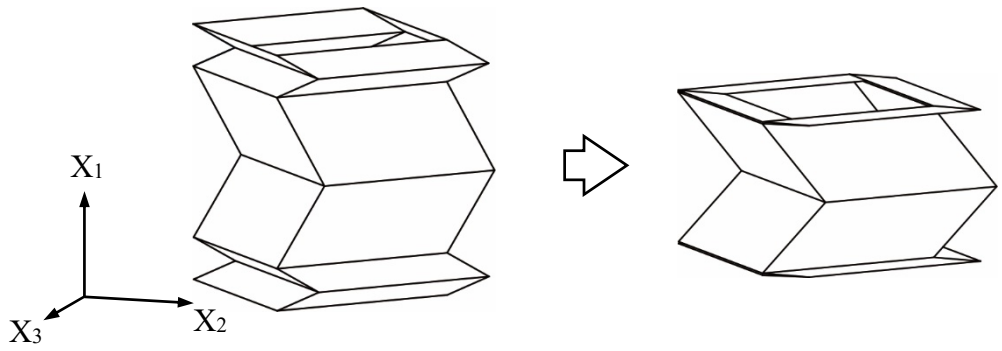

Fig. 3.5 Self-locking of the Miura-ori honeycomb cell.

3.1.3 Multiple layering of Miura-ori honeycomb

Figure 3.2 (a) shows a Miura-ori honeycomb unit with a single core layer. In fact, the Miura-ori honeycomb can be built with multiple core layers by inserting more core layers into the pattern. Also it is possible to have more different intermediate flange layers. The subsequent Miura-ori honeycombs discussed later have multiple core layers and flange layers with different geometric configurations.

3.2 Theoretical analysis

In this section, a simple strut model is used to illustrate qualitatively how the Miura-ori honeycomb can effectively reduce the peak force when it is subjected to axial compression. Functionality of flange layers that help to achieve the grading feature and increase overall energy absorption capacity will be discussed.

3.2.1 Strut model

Figure 3.6 shows an initially imperfect strut with pin joints at both ends. The magnitude of the kink is determined by the parameter a_k (Grzebieta and Murray, 1985).

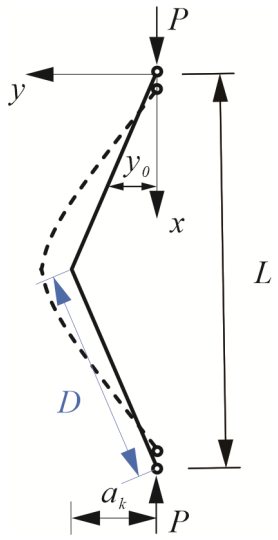

Figure 3.6 An initially kinked strut under axial compressive load.

The strut can be considered as a simplified model of the cross-section of any core layer of the Miura-ori honeycomb cell when it is cut by the plane that is parallel to the X_1-X_3 plane (Fig. 3.5). When compressive force P acts on the strut, the elastic behavior of the strut can be expressed as

$$\delta_{pinned}^{E} = \left[\frac{a_k}{L\cos\left(\frac{kL}{2}\right)}\right]^2 \left[L + \frac{\sin(kL)}{k}\right] \tag{3.5}$$

where $k^2 = P/EI$, EI is the bending stiffness and δ_{pinned}^{E} is elastic crush distance.

A post-collapse analysis can be carried out if the strut deforms to such an extent. Assuming the material behaves in a rigid-plastic manner and the stress distribution at the midpoint of the strut is illustrated in Fig. 3.7.

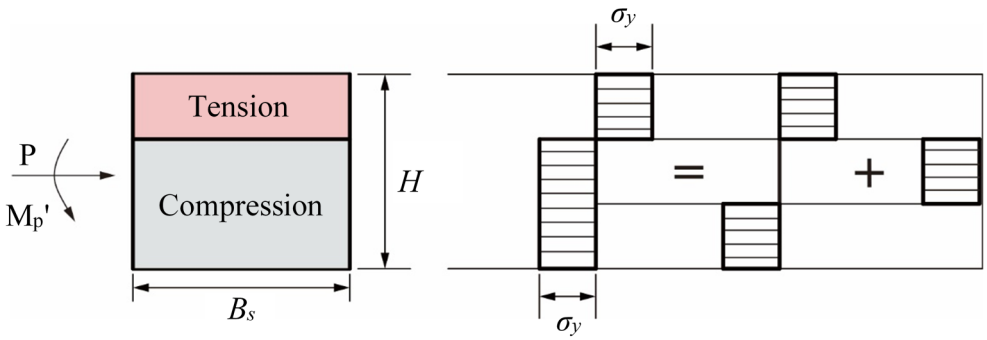

Fig. 3.7 Assumed collapse mechanism of the pin-ended strut.

The plastic behavior of the strut can be expressed as

$$\delta_{pinned}^{P} = \frac{M_p^2}{DP^2}\left[1-\left(\frac{P}{P_y}\right)^2\right]^2 \tag{3.6}$$

where $M_p' = \sigma_y B_s (H^2 - \mathrm{d}^2)/4$, $M_p = \sigma_y B_s H^2/4$, $P_y = B_s H \sigma_y$, d is the depth of the central core of material that carries the axial load, σ_y is the yield stress of the material, B and H are the width and height of the strut cross-section, δ_{pinned}^{P} is plastic crush distance.

By superimposing the theoretical curves derived from Eqs. (3.5) and (3.6), the force-displacement curve is plotted as shown in Fig. 3.8 (Murray, 1956). The total energy absorbed by the strut is the area under the curves. It is shown that the total energy is dominated by plastic deformation energy, while the peak force is dominated by the initial elastic stiffness of the strut.

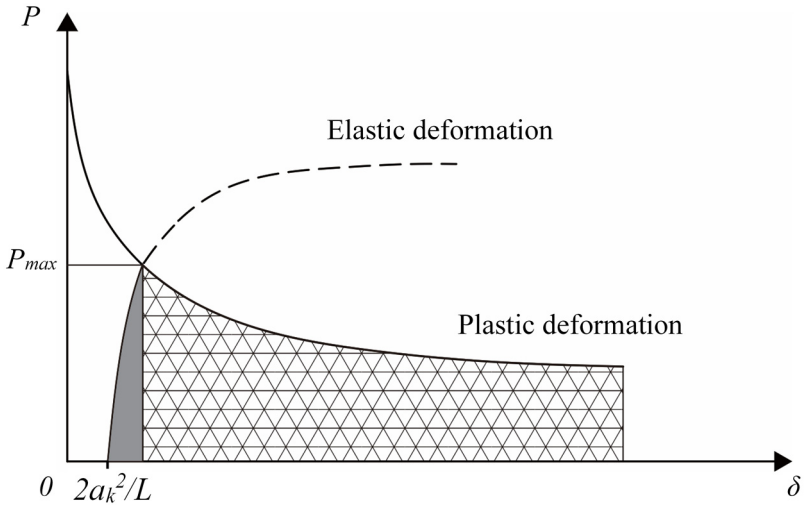

Fig. 3.8 Force-displacement curves of an initially kinked strut under axial compressive load.

It can be found from the above results that for an imperfect pin-ended strut, by increasing the size of the initial kink, it can efficiently reduce the peak force. Therefore, in the case of the Miura-ori honeycomb, by decreasing the value of edge angle ζ, it can also effectively reduce the peak load when the structure is subjected to axial compression. However, it can be also noted from the strut model that the increase of the kink size also results in the reduction of the energy absorbed by plastic deformation. In order to overcome this defect and increase the plastic deformation, the design of the flange layer plays the most important role.

3.2.2 Functionality of flanges

The flange layers of the Miura-ori honeycomb play a very important role of increasing the plastic deformation of the core layer, resulting in the increase of overall energy absorption capacity. This is due to the following two aspects.

First, the flange layer plays a role of changing the boundary condition of the core layer. For example in the previous section, if the pin constraint of the strut in Fig. 3.6 is changed to fixed ends, three plastic hinges will be induced (Fig. 3.9 (b)) and the strut with fixed ends can absorb more energy than an equivalent pin-ended strut, as shown in Fig. 3.9 (c) (where the energy stored by elastic deformation is neglected) (Murray, 1983). Therefore, when an axial compressive force is applied on a Miura-ori honeycomb unit cell in the out-of-plane (X_1) direction, the upper and lower flanges will be primarily densified and then self-locked. After self-looking, the densified flange layers create the semi-fixed (between pined and clamped) boundary condition at both ends of the core layer and sequentially change the stiffness property of the honeycomb and enhance the energy absorption capacity of the core layer.

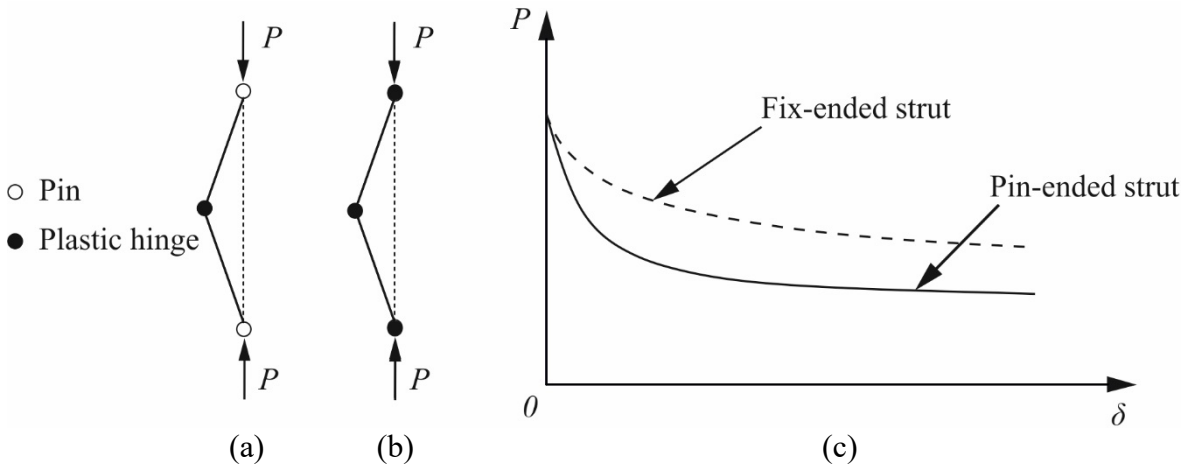

Fig. 3.9 An initially kinked strut with fixed ends under axial compressive load: (a) An initially kinked strut with pin ends; (b) an initially kinked strut with fixed ends; (c) force-displacement comparison between the kinked strut with pin and fixed ends.

Second, the flange layer helps to increase the plastically deformed area along the zig zag creases of the core layer.

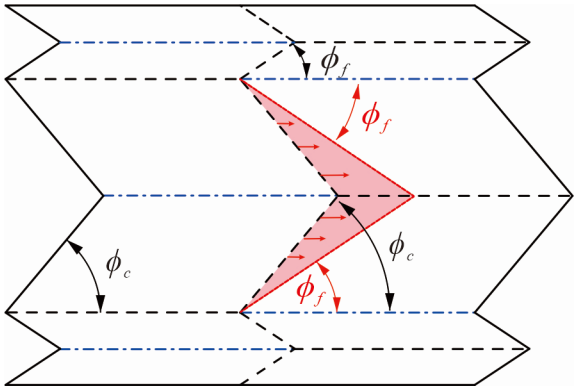

Fig. 3.10 Propagation of enhanced plastic deformation.

As mentioned above, the Miura-ori itself is flat-foldable, but the proposed Miura-ori honeycomb is not flat-foldable. Therefore, taking a Miura-ori honeycomb cell as an example, when it is compressed in the out-of-plane direction, its flange layers will be flattened first following the designed crease pattern. When the load continues to be applied, in order to be flattened, the zig zag crease in the core layer initially at an inclination ϕ_c, will swipe through an area that reaches the position with the inclination ϕ_f, as illustrated in Fig. 3.10. The highlighted area represents the plastic zone. This will increase the energy absorption capacity of the Miura-ori honeycomb substantially.

3.3 Experiments

To evaluate the mechanical behavior of Miura-ori honeycomb, quasi-static compression tests in out-of-plane direction of Miura-ori honeycomb were conducted. All experimental specimens were 3D-printed by using the machine Objet260 Connex3, and the material used for 3D printing was a hybrid plastic which was a mixture of 'VeroYellow' and 'TangoBlack' provided by the company Stratasys. Uniaxial tensile tests were performed primarily to obtain mechanical properties of the hybrid plastic.

3.3.1 Tensile test for material properties of 3D-printed hybrid plastic

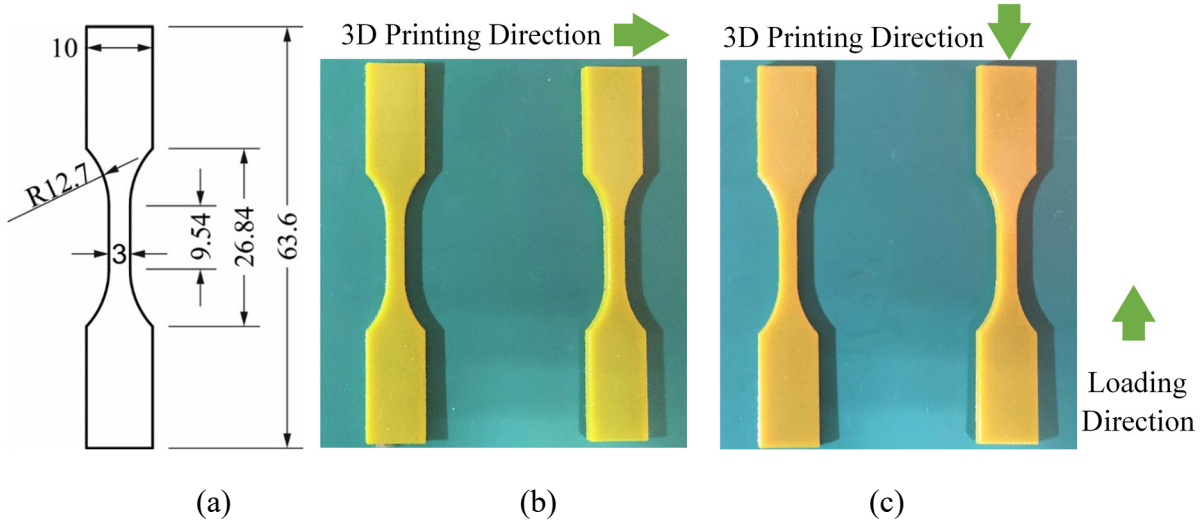

Fig. 3.11 Tensile test specimens: (a) Dimensions of the dumbbell specimen; (b) dumbbells printed in transverse direction; (c) dumbbells printed in perpendicular direction

In the present work, quasi-static tensile material tests were conducted using an Instron-5943 universal testing machine. All four specimens for tensile tests were dumbbell shaped with the thickness of 1.5mm according to ASTM D638 (2014) specification as shown in Fig. 3.11(a). In order to analyze possible material anisotropy, two specimens were 3D-printed in transverse direction and the other two were 3D-printed in perpendicular direction as indicated in Fig. 3.11(b) and (c), respectively. Before the test, two markers were manually marked in the middle

of all specimens and the distance between the markers were approximately 8mm. Once the specimen was clamped, the laser sensor of the Instron-5943 universal testing machine would capture the middle points of the markers and generate the engineering strain automatically during the test, as indicated in Fig. 3.12(a). All specimens were tested with the loading speed of 0.5mm/min till failure, specimens after the tests are shown in Fig. 3.12(b) and (c).

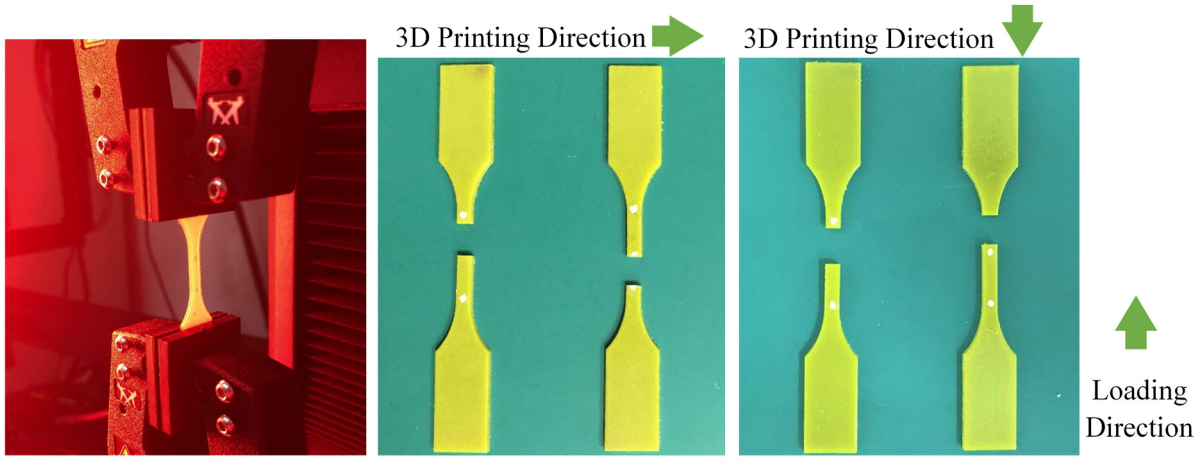

Fig. 3.12 Tensile test: (a) Test set up. (b) specimens printed in transverse direction after the test; (c) specimens printed in perpendicular direction after the test.

A comparison of typical tensile engineering stress-strain curves for 3D-printed hybrid plastic at transverse and perpendicular directions are shown in Fig. 3.13 (a), and the engineering stress was calculated by

$$\sigma = P / A_o \tag{3.7}$$

where A_o is the initial cross-section area. In the tensile test, A_o=3mm*1.5mm=4.5mm^2.

Since the stress-strain curves of the specimens printed in the transverse direction were close to that of the specimens printed in the perpendicular direction, the mechanical properties of the 3D-printed material were considered to be approximately isotropic. Because in the present work the origami-honeycomb specimens were 3D-printed in the transverse orientation and loaded perpendicularly to the printing direction, the stress-strain curves of the specimens printed in the transverse direction was chosen to describe the material. As shown in Fig. 3.13 (b), Young's

modulus was obtained by fitting the initial linear portion of the curves, and the yield stress σ_y was calculated by averaging the stress values of upper yield point A and lower yield point B. The approximate results were: E = 80 MPa and σ_y = 10.5 MPa. Because the strain-hardening was insignificant, and based on the classical theory of plasticity (Hill, 1950; Martin, 1975; Prager and Hodge, 1951), the elastic-perfectly plastic model was adopted, as the red dashed line shown in Fig. 3.13 (b). The Poisson's ratio and density was measured as v = 0.3 and ρ = 1020 kg/m^3, respectively.

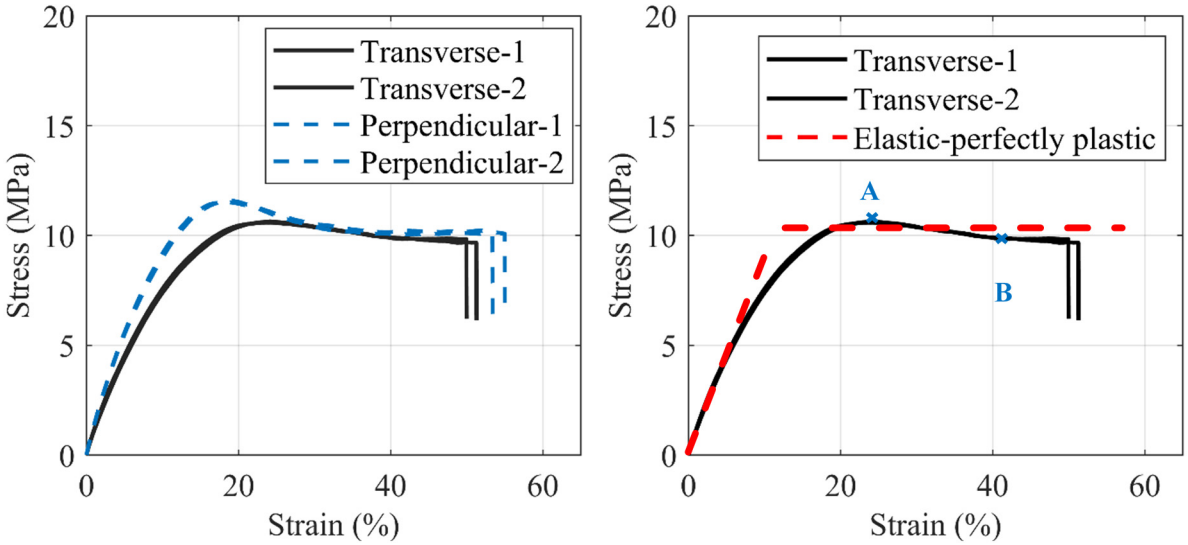

Fig. 3.13 Stress-strain results of the tensile tests: (a) Stress-strain curves of dumbbell specimens; (b) stress-strain curves of transversely printed dumbbells and the equivalent material model.

Friction coefficient of the 3D-printed plastic itself was tested for the subsequent FE analysis. The testing procedures are: 1) Place a dumbbell specimen used for the tensile test on top of a 10cm*10cm square plate. The plate is 3D-printed by using the same hybrid plastic material with the thickness of 1.5mm; 2) raise one side of the plate until the dumbbell specimen starts to slide; 3) record the angle value once the dumbbell specimen starts to slide, as indicated in Fig. 3.14; 4) the friction coefficient $f = \tan\theta$. In the present work, the value of the angle θ was tested to be 14°. Thus, $f = \tan 14° = 0.25$.

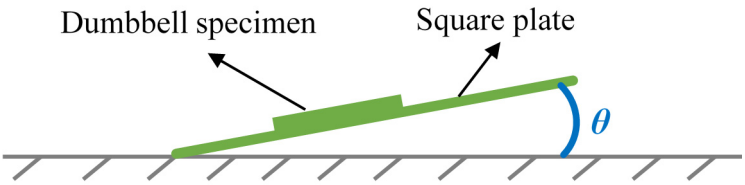

Fig. 3.14 Schematic illustration of the method used for friction coefficient test.

3.3.2 Out-of-plane compression test

The compression tests were conducted to investigate the mechanical behaviors of the Miura-ori honeycomb and to evaluate the self-locking functionality triggered by the flanges.

Before the experiment, preliminary simulations of the compression test were conducted in order to determine the minimum configuration needed for the model as the cost of 3D-printed specimens are quite high. In the preliminary simulations, five numerical models were constructed by using the core unit cells, and they were built in the configuration of 2x2x2, 3x3x3, 4x4x4, 5x5x5 and 6x6x6 units, respectively, as indicated in Fig. 3.15. The dimensions of the core unit cell are: $\phi_c = 69.3°$, $\zeta_c = 120°$, $a_c = 5.31$mm, $b = 10$mm and the wall thickness $t = 0.5$mm. The relevant FE model was the same one that used for the subsequent FE analyses which will be explained later in section 3.4 with details.

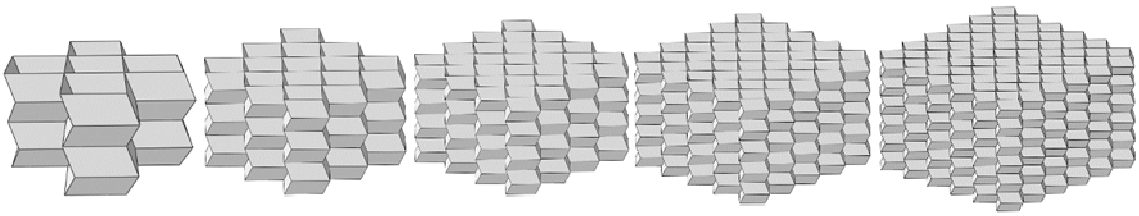

Fig. 3.15 Models used to determine minimum configuration.

The simulation results was concluded in Fig. 3.16, and it showed little difference among the specimens built with 4x4x4, 5x5x5 and 6x6x6 configurations. Hence, in order to save the cost

financially and computationally, the 4x4x4 configuration was finally chosen for all subsequent models.

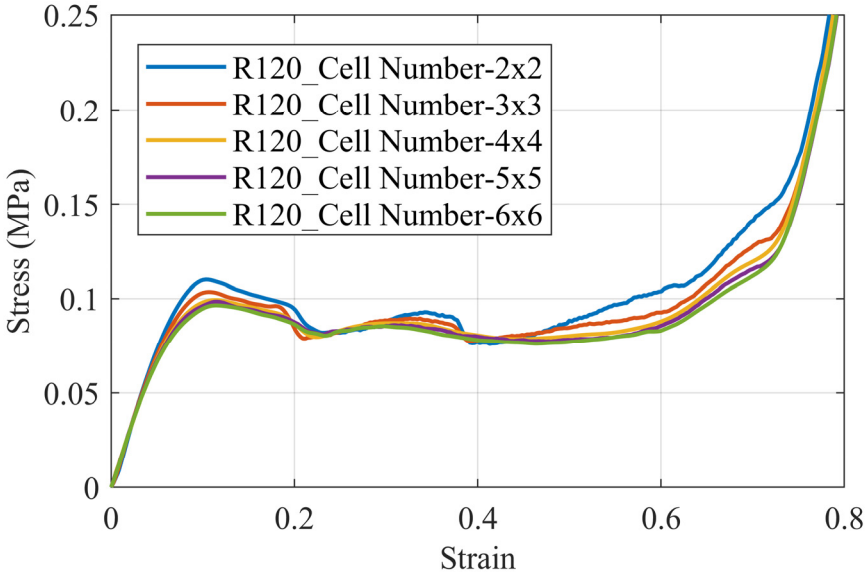

Fig. 3.16. FE results of preliminary simulations.

The test model of Miura-ori honeycomb was constructed with five flange layers and four core layers, referred to as F_1 to F_5 and C_1 to C_4 from top to bottom respectively, as indicated in Fig. 3.17. Each layer contained 16 cells built in a four by four configuration.

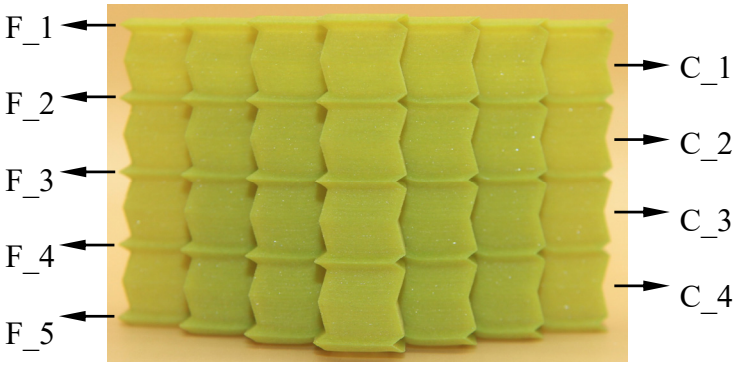

Fig. 3.17 Test model of Miura-ori honeycomb.

Three sets of experimental specimens were produced, each set contained four specimens of two types of structure: the designed model and the reference model, as illustrated in Fig. 3.18 (a) and (b) respectively. The latter had no flange layers. Dimensions of test samples are listed in Table 3.1, all specimens had thickness of 0.5mm and initial cross-section area of 2500 mm^2 along the loading direction. The initial heights of the reference and Miura-ori honeycomb

samples are 36.8 mm and 48.12 mm, respectively. The test setup is shown in Fig. 3.18 (c) and displacement controlled loading was applied with a constant loading speed of 2mm/min. Friction coefficient of the plastic and rigid loading panel was tested according to the previous method and the result was $f = 0.25$.

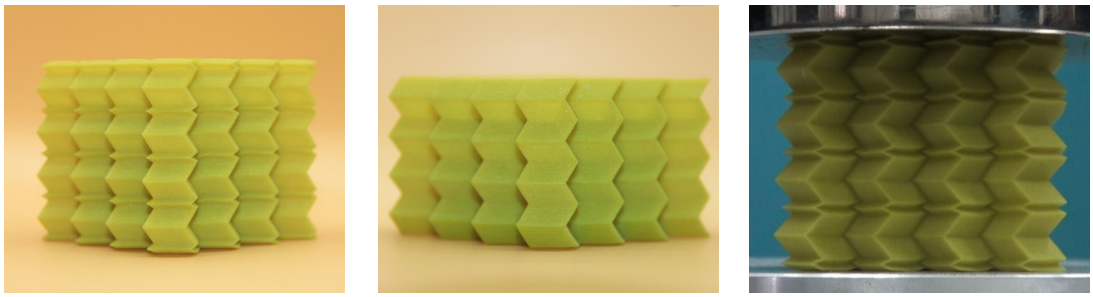

(a) (b) (c)

Fig. 3.18 Experimental specimen and setup: (a) 3D-printed Miura-ori honeycomb model; (b) reference model; (c) test setup.

Table 3.1: Dimensions of test samples.

	ϕ_c	ζ_c	a_c (mm)	b (mm)	ϕ_f	ζ_f	a_f (mm)	mass (g)	ρ_o (kg/m^3)
Model_ Set_1	63.0°	100°	6.00	10.00	50.5°	51.8°	2.59	24.61	204.6
Ref_Set_1	63.0°	100°	6.00	10.00	—	—	—	15.65	170.1
Model_ Set_2	69.3°	120°	5.31	10.00	50.5°	51.8°	2.59	22.56	187.5
Ref_Set_2	69.3°	120°	5.31	10.00	—	—	—	14.35	156.0
Model_ Set_3	76.0°	140°	4.90	10.00	50.5°	51.8°	2.59	21.24	176.6
Ref_Set_3	76.0°	140°	4.90	10.00	—	—	—	13.38	145.4

Due to the differences of the initial heights between the reference model and Miura-ori honeycomb, the load-displacement curves obtained from the experiments are converted into engineering stress-strain curves in order to directly evaluate their crushing behavior and compare the differences. The engineering stress-strain curve obtained from the test is summarized in Fig. 3.19. The engineering stress is calculate by Eq. (3.7) and the engineering strain is calculated by

$$\varepsilon = \delta / h \tag{3.8}$$

where δ is the crushing distance and h is the initial height.

The results of the reference model and Miura-ori honeycomb in 'Set_1' both contain three stages of deformation. As shown in Fig. 3.19 (a), at stage 1, starting from zero, the stress increases until a plateau is reached. At stage 2, the stress varies a little while the strain increases. During stage 3, the stress increases rapidly followed by the densification of the structure.

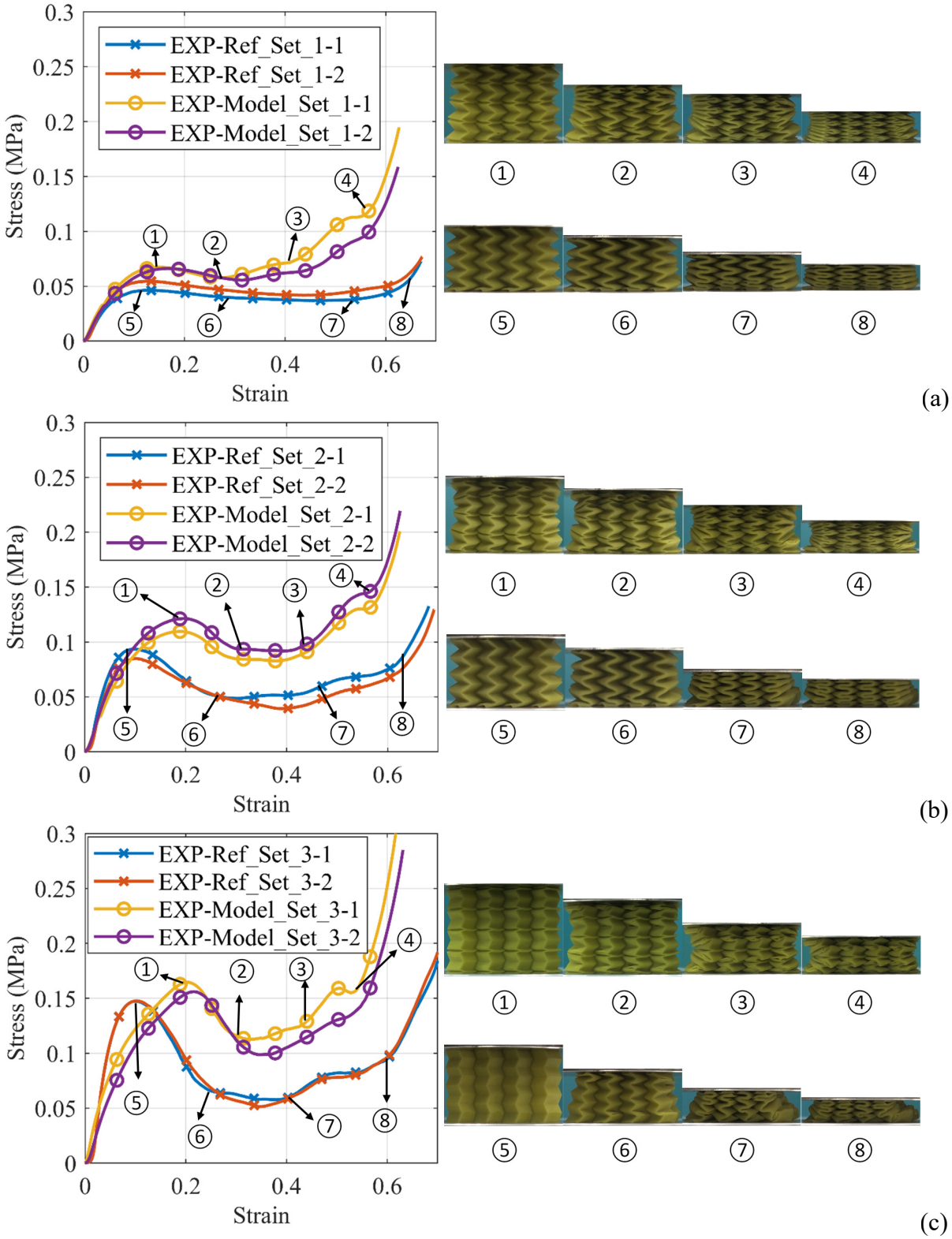

Fig. 3.19 Stress-strain curves of experimental specimens: (a) Set_1, (b) Set_2 and (c) Set_3.

The results of the reference model and the Miura-ori honeycomb in Set_2 and Set_3 both exhibit four stages, as shown in Fig. 3.19 (b) and (c). At the beginning, the stress increases until reaching a pronounced peak (stage 1). Then the stress decreases notably due to the buckling of the core layers and settles on a plateau (stage 2). At stage 3, the stress varies little in magnitude while the strain increases. During the last stage, the stress increases rapidly and reaches densification.

By comparing the stress-strain curve between the Miura-ori honeycomb and the reference model, it is obvious that the Miura-ori honeycomb is more efficient than the reference model in term of volumetric energy absorption. This result shows that flange layers help to increase energy absorption and the larger the ϕ_c is, the more energy the structure will absorb, but load uniformity is not good.

Another important standard to evaluate the energy absorption capacity is the SEA which is defined as the energy absorbed per unit mass. The amount of energy absorption is the area below the load-displacement curve. For conventional cellular material, the load-displacement curve usually consists of three stages. In stage 1, the response is linear-elastic. This stage determines when a critical load is reached and this critical load level is maintained almost constant over a relatively long range of displacement, which is called the plateau region (stage 2). Finally in stage 3, the load increases rapidly when cell walls touches and it is called the densification stage. However, the energy absorbed during the densification stage is normally trivial; thus, it is being ignored (Gibson and Ashby, 1997). Thus, the SEA can be calculated by using Eq. (3.9),

$$\mathrm{SEA} = \frac{\int_0^{x_0} P(x)dx}{m} \tag{3.9}$$

where m is the mass, $x_0 = \delta_D$ and δ_D is the effective crushing distance ─ the distance before densification starts.

From Eq. 3.9, it can be noted that the determination of the effective crushing distance plays an important rule as it will affect the valid energy absorption capacity. For typical energy absorbing cellular material, there is a clear boundary between the plateau and densification regions. Thus, the effective crushing distance can be easily defined, which is the crushing distance before the densification starts (when the load increases rapidly). When there is no obvious boundary between the plateau and densification regions, the following empirical equation Eq. (3.10) can be used to determine the densification strain for conventional cellular materials (Gibson and Ashby, 1997), and the equivalent effective crushing distance can be hereby calculated by using Eq. (3.11),

$$\varepsilon_d = 1 - 1.4\left(\frac{\rho_o}{\rho_s}\right) \tag{3.10}$$

where ρ_o is the density of the cellular material and ρ_s is the density of the solid of which the cellular material is made, and

$$\delta_D = h \times \varepsilon_d \tag{3.11}$$

where h is the initial height of the cellular material.

By using Eq. (3.10), the densification strain of the origami honeycombs of the test specimens are listed in Table 3.2. By comparing the results from Table 3.2 and Fig. 3.19, it is obvious that the calculated densification strain cannot correctly define the actual result. This means that the empirical equation (3.10) does not apply to the origami honeycombs of the present study. In the present work, a simple and unified method is given to determine the densification region and the effective crushing distance of origami honeycombs by the comparison and observation of the load-displacement curve and the actual deformation magnitude of the specimen. When the overall cell walls start to touch (jam together) and the load start to increase notably, the subsequent region is defined as densification region and the effective crushing distance is the distance before the starting point of the defined densification. For example in Fig. 3.19 (b), points ③ and ⑦ are defined as the starting points of the densification of Model_ Set_2 and Ref_Set_2, respectively. Hence, the effective crushing distances are 21.21 and 16.86 mm,

respectively.

Table 3.2: Densification strain obtained from empirical equation.

	Model_ Set_1	Ref_Set_1	Model_ Set_2	Ref_Set_2	Model_ Set_3	Ref_Set_3
ε_d	0.72	0.77	0.74	0.79	0.76	0.80

By following the above principle, the results of effective crushing distances of test specimens are summarized in Table 3.3, and the results of averaged SEA are summarized in Fig. 3.20.

Table 3.3: Effective crushing distance of test specimens.

	Model_ Set_1	Ref_Set_1	Model_ Set_2	Ref_Set_2	Model_ Set_3	Ref_Set_3
δ_D	20.18(o)	19.12(x)	21.02(o)	16.70(x)	21.37(o)	15.32(x)
(mm)	20.53(o)	19.08(x)	21.21(o)	16.86(x)	21.72(o)	15.36(x)

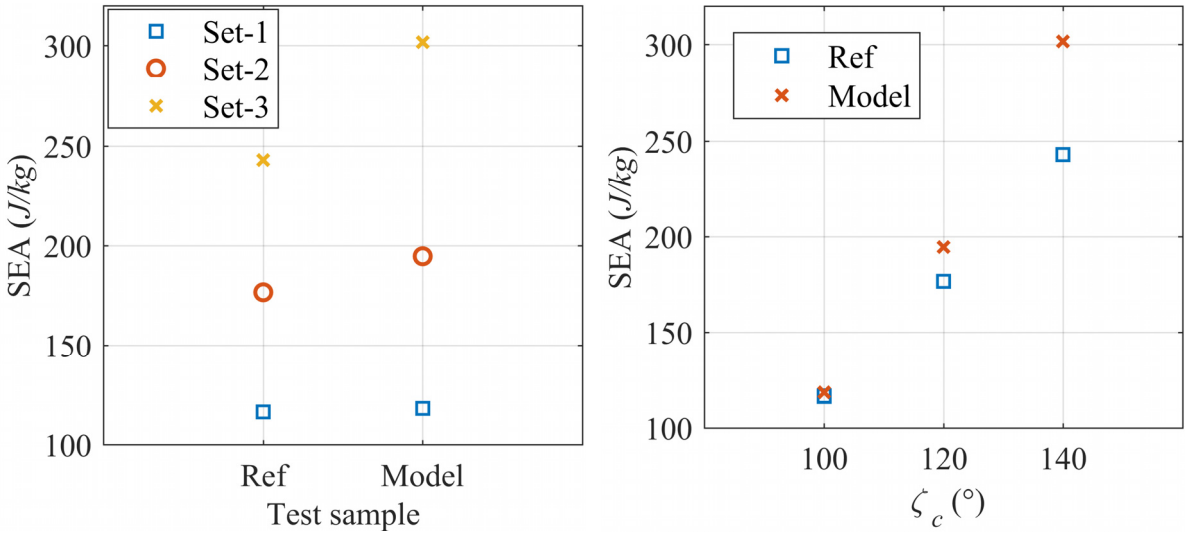

Fig. 3.20 SEA results: (a) Model comparison among each set; (b) effect of ζ_c on SEA.

It is obvious that the Miura-ori honeycomb absorbs more energy per unit mass than that of the reference model. This indicates the design of Miura-ori honeycomb with the unique self-locking feature is effective in terms of increasing the energy absorption capacity, which also verifies the simplified strut theory mentioned previously. From Fig. 3.20 (b) and Fig. 3.19, it can be found that with different structural configuration, the Miura-ori honeycomb exhibits different energy absorption capacity, as well as deformation patterns. Hence, comprehensive study of the Miura-ori honeycomb is conducted numerically and introduced in the next chapter.

3.4 Finite element analysis

The finite element analyses were conducted to study the energy absorption capacity and related mechanical properties of proposed Miura-ori honeycombs under quasi-static compression, as well as the influences of different geometric configurations. Commercial software Abaqus/explicit (2016) was employed and numerical 3D models were preliminarily built in PTC Creo (2018) and input into Abaqus for analysis subsequently.

3.4.1 Finite element model and validation

- **FE model**

The crushing scenario of the Miura-ori honeycomb was modeled by placing the numerical sample between two rigid panels with the bottom plate fixed completely, whereas all degrees of freedom of the moving upper plate were constrained except for the uniaxial loading direction, as indicated in Fig. 3.21. A small gap of 0.1mm was left between the upper plate and the specimen to avoid initial penetration. Displacement controlled boundary condition was applied to the upper plate to simulate the loading process and the crushing distance was set to be approximately 80% of the specimen height.

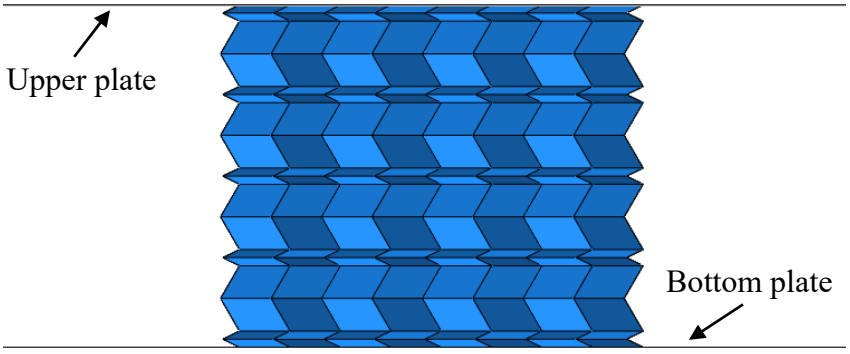

Fig. 3.21 FE model.

Preliminary finite element analyses were carried out by simulating the compression tests that conducted previously. Four-node shell elements with reduced integration S4R were employed for meshing. Self-contact was defined, which took into account hard contact and the friction coefficient $f = 0.25$. As mentioned previously in section 3.3.1, the 3D-printed material can be considered as an isotropic and elastic-perfectly plastic material under uniaxial tension. Hence,

an elastic-perfectly plastic model was implemented in Abaqus/Explicit for the assignment of material properties of the origami honeycombs. The elasticity was assigned with: $E = 80$ MPa and $\nu = 0.3$. For plasticity, Abaqus uses associated plastic flow (Abaqus, 2016). Therefore, as the material yields, the inelastic deformation rate is in the direction of the normal to the yield surface and the plastic deformation is volume invariant. The Mises yield surface was used to define isotropic yielding, and it was defined by giving the value of the uniaxial yield stress as a function of uniaxial equivalent plastic strain (Abaqus, 2016). Generally, a material's plastic flow stress σ_{pf} can be expressed as (Xu, et al., 2016),

$$\sigma_{pf} = f\left(\varepsilon_{pf}, \mathrm{T}\right) \cdot \mathrm{R}\left(\dot{\varepsilon}\right) \tag{3.12}$$

where f is the quasi-static stress-strain behavior, T is the temperature and R is the ratio of the yield stress at any strain rate to the static yield stress. Since the hardening effect can be ignored for the 3D-printed hybrid plastic material, the perfect plasticity was assigned in Abaqus with the yield stress of $\sigma_y = 10.5$ MPa.

- **Mesh sensitivity**

Different element sizes had been applied on model "Ref_Set_2" to determine mesh sensitivity, as indicated in Fig. 3.22(a) and Fig. 3.22(b) plots the force-displacement curves obtained from FE. The specimen with mesh size of 0.5 and 0.4 mm resulted in a reduction in force compared to the one with 1.0 mm of mesh size. Since the result of 0.4 mm mesh size converges with the one with 0.5 mm, an element size of 0.4 mm was selected as the default element size for all subsequent simulations. The ratio of kinetic energy to internal energy was also checked to be less than 5%, which ensures the dynamic effect is negligible.

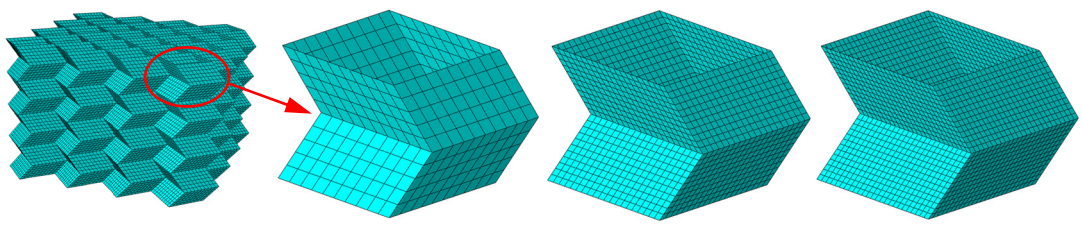

(a)

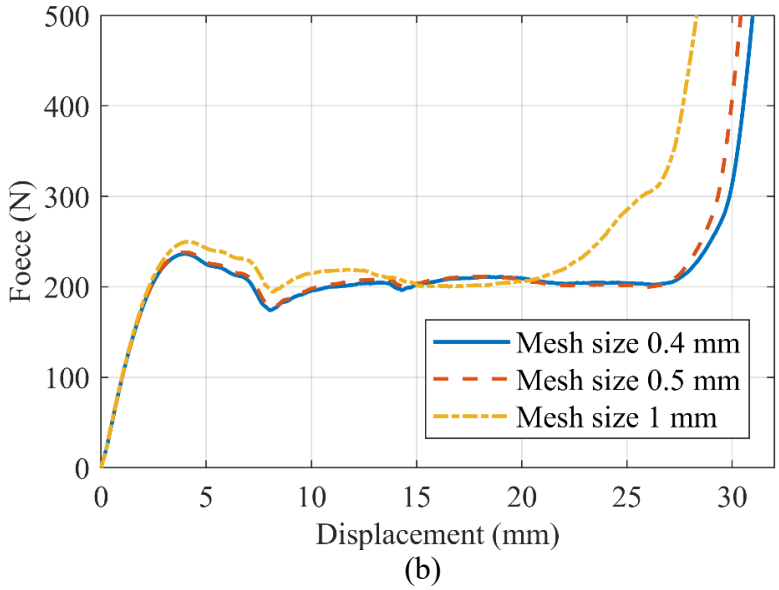

(b)

Fig. 3.22 Effect of mesh size: (a) FE models with different mesh size; (b) force-displacement curves for mesh size.

- **Model validation**

The FE model was validated by comparing the numerical results against the experimental ones, and the numerical force-displacement results along with the comparison with the experiments are shown in Fig. 3.23 (a) to (f). Due to the similarity of the structure among each Set, the experimental and numerical results of deformation patterns of Set_2 were chosen as representatives for comparison, as shown in Fig. 3.24 (a) and (b).

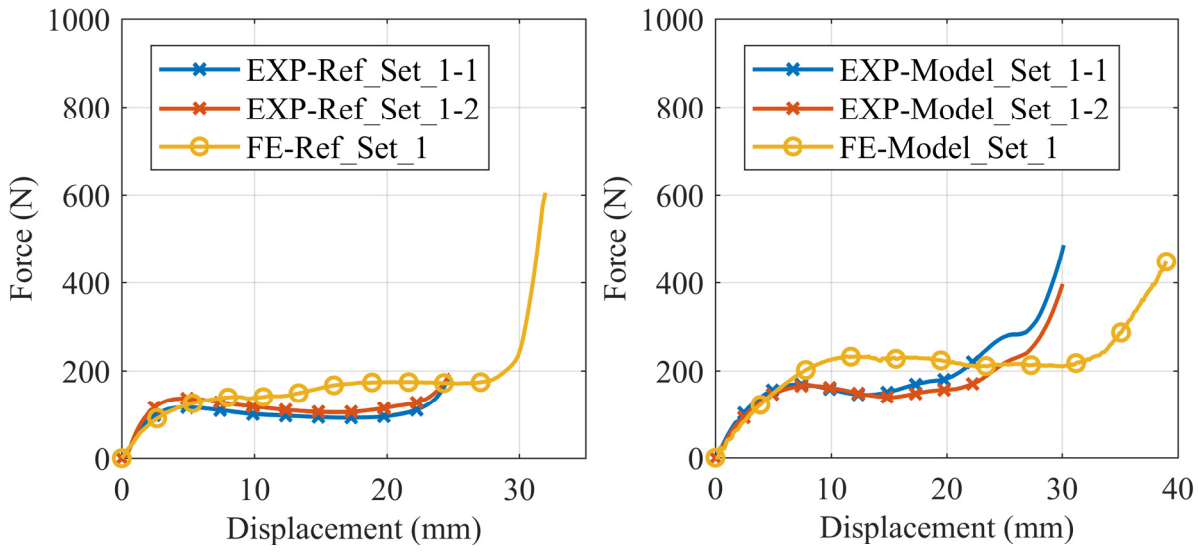

(a) (b)

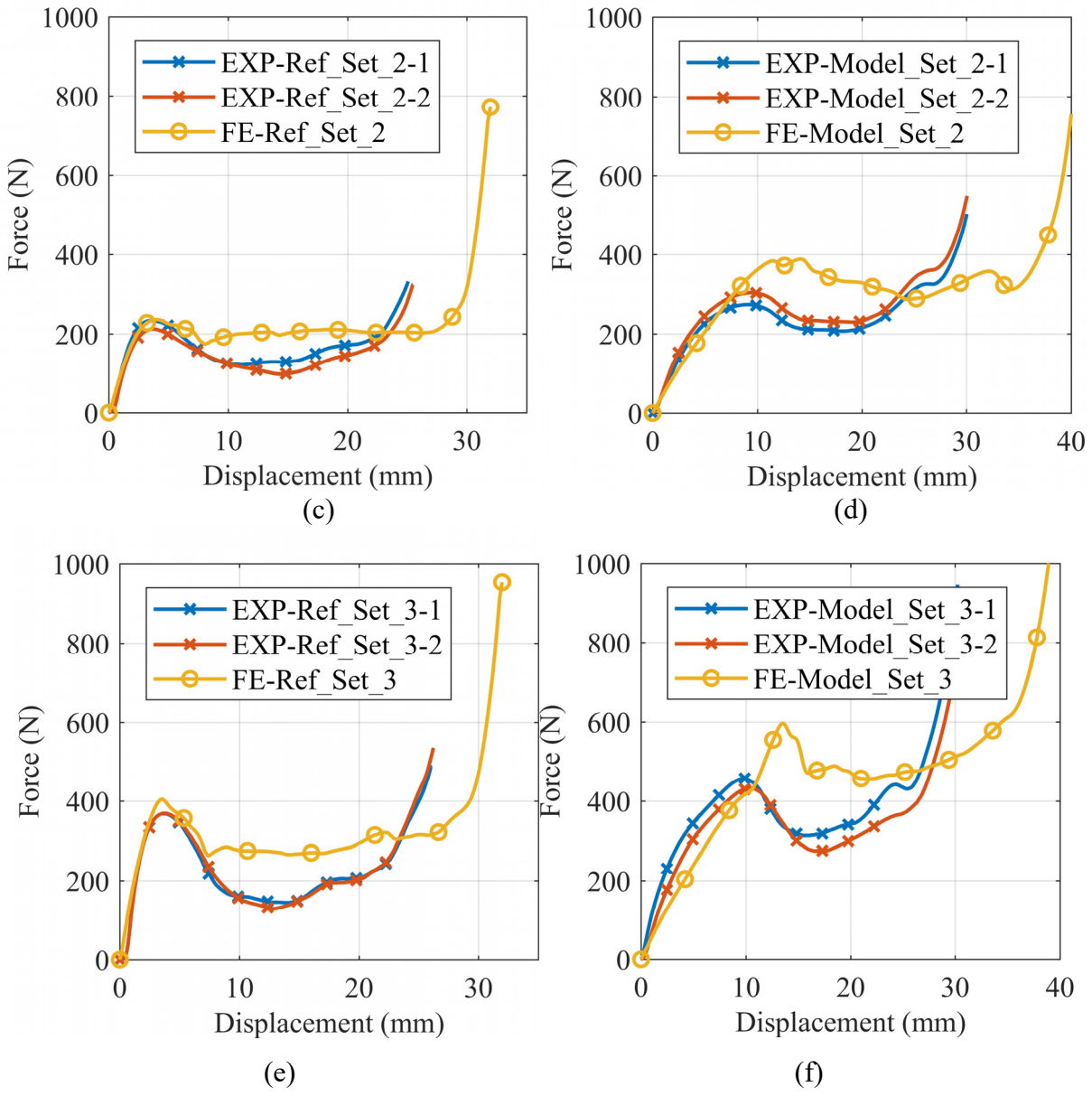

Fig. 3.23 Test and simulation force-displacement curves: (a) Ref_Set_1; (b) Model_Set_1; (c) Ref_Set_2; (d) Model_Set_2; (e) Ref_Set_3; (f) Model_Set_3.

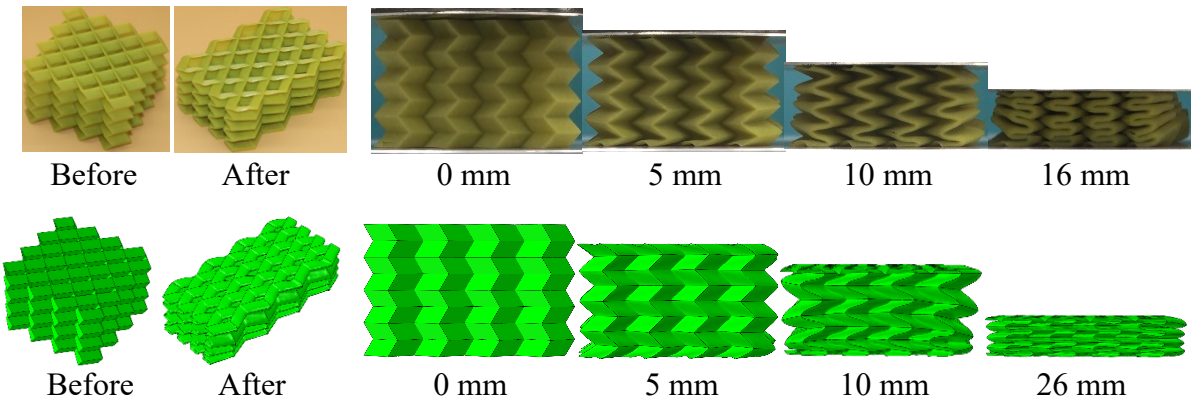

(g)

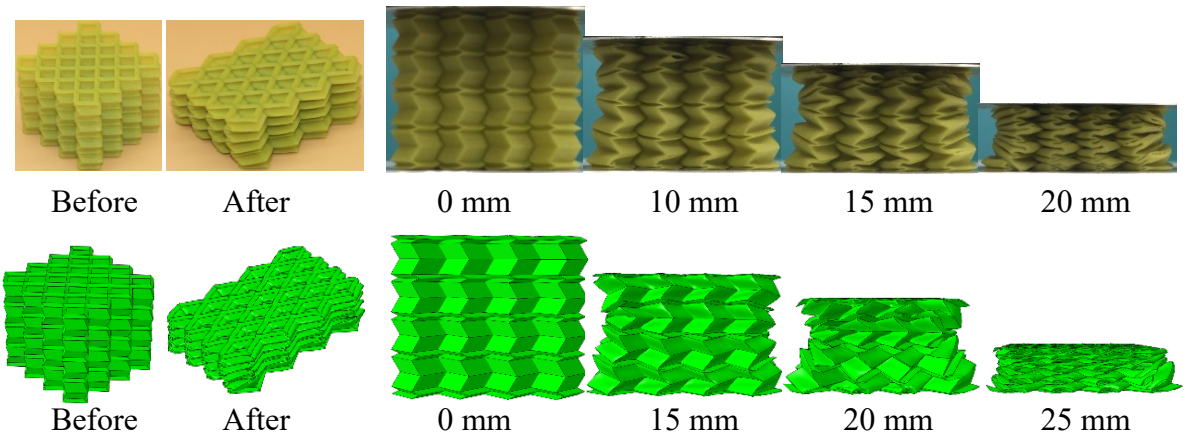

(h)

Fig. 3.24 Test and simulation deformation patterns: (a) Ref_Set_2; (b) Model_Set_2.

The simulation showed good agreement with the test up to a large value of displacement, as well as the deformation patterns. Hence, the FE model was validated to be effective in simulating the compression process of Miura-ori honeycomb.

It should be noted that in previous FE analyses, shell elements were employed to model the numerical specimens. Commonly, shell elements are used to model structures in which one dimension, the thickness, is much smaller than the other dimensions (Abaqus, 2016), and they can produce reliable results and save much more computational time when compared to the solid elements. In the present work, the wall thickness of the origami honeycomb cells is much smaller than the other dimensions, thus the shell elements were applied to model the origami honeycombs. In this case, a single simulation job of origami honeycomb under quasi-static compression (e.g. Model_Set_1) with the mesh size of 0.4mm took more than 36 hours (CPU Intel i7 7700, RAM 64GB) to run. It can be predicted that for the same case, more computational time will be cost if choosing solid elements. More importantly, the results base on the FE model with shell elements were shown to be consistent with those in test. Therefore, the shell element was chosen to model the origami honeycombs in the present work.

3.4.2 Parametric study

In order to study the geometric effects, a total of 32 different numerical models of Miura-ori honeycomb with thickness of 0.5 mm were constructed in the same form of previous test models, as shown in Fig. 3.25.

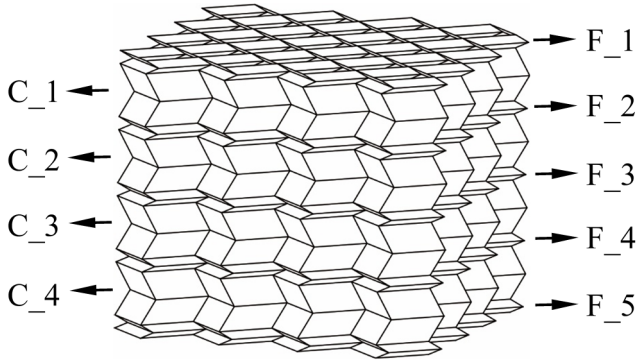

Fig. 3.25 3D model of Miura-ori honeycomb.

These models were divided into four groups and specimens of each group were constructed with identical ζ_f (ϕ_f) values but different ζ_c (ϕ_c) values. In group CAT_455, CAT_505 and CAT_555, the value of ϕ_f is 45.5°, 50.5°, and 55.5° respectively. In group CAT_GR, the flange layers were constructed with a gradient, as the values of ϕ_f are 45.5°, 48°, 50.5°, 53° and 55.5° from top to bottom respectively. This also results in a gradient of edge angle ζ_f and the values are 15.2°, 37.7°, 51.8°, 63.3° and 73.5° from top to bottom respectively. As the difference between each group is only limited by the value of ϕ_f (ζ_f), the general dimensions of numerical models in each group are listed in Table 3.4. The heights of specimens in group CAT_455, CAT_505, CAT_555 and CAT_GR are 40.51mm, 48.12mm, 51.33mm and 47.08mm, respectively. A specific specimen among each group is name in the form of 'R ζ_c_ ϕ_f', for example, 'R100_455' refers to the specimen constructed with ζ_c = 100° and ϕ_f = 45.5° in group CAT_455. Therefore, specimens of Model_Set_1, Model_Set_2, and Model_Set_3 in the previous study are hereby renamed as R100_505, R120_505 and R140_505 in the following study.

Table 3.4: General dimensions of specimens in each group.

	ϕ_c	ζ_c	a_c (mm)	b (mm)	a_f (mm)	*mass* (g)
R100	63.0°	100°	6.00	10.0	2.59	88.40
R110	66.1°	110°	5.62	10.0	2.59	86.00
R120	69.3°	120°	5.31	10.0	2.59	84.10
R130	72.6°	130°	5.08	10.0	2.59	82.70
R140	76.0°	140°	4.90	10.0	2.59	81.70
R150	79.5°	150°	4.76	10.0	2.59	80.90
R160	82.9°	160°	4.67	10.0	2.59	80.40
R170	86.47°	170°	4.62	10.0	2.59	80.10
R180	90.0°	180°	4.60	10.0	2.59	80.00

It should be noted that the pre-designed pattern of different flange layer are based on an identical rectangular frame, as illustrated in Fig. 3.26. Thus, the mass of flanges with different values of ϕ_f are the same. As a result, specimens with same ζ_c values have identical mass property. For example, the mass of R100_455, R100_505, R100_555 and R100_GR are the same.

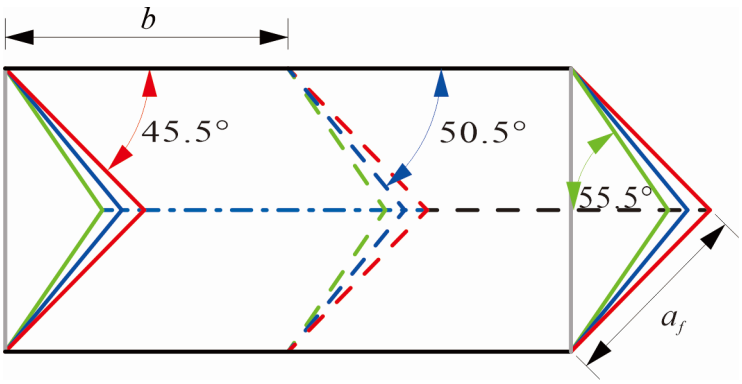

Fig. 3.26 Schematic pattern of flanges.

A conventional square honeycomb (REF_SQ) with the same thickness of 0.5mm was also modeled as a reference in order to compare with the Miura-ori honeycombs, it was built with a total of 16 cells with a four by four configuration in the out-of-plane direction. The side length of each cell is 10mm and the overall height is 48.12mm.

As mentioned above, the energy absorption capacity of the energy absorbing material mainly depends on the irreversible plastic deformation caused by the impact. Therefore, in common actual engineering applications, energy absorbing materials are generally made of metal materials. For example titanium, due to its high specific strength and high energy absorption

capacity, it is ideally suited for applications within the aerospace industry (Lefebvre, *et al.,* 2008). Therefore, in the parametric study conducted in this section, in order to be more relevant to actual engineering application, the industry level Ti-Al-4V titanium alloy (TC4) was adopted as base material for all subsequent simulations, and the elastic-perfectly plastic constitutive model was implemented in Abaqus/Explicit for the assignment of material properties. The properties are: $\rho = 4400$ kg/m^3, $E = 110$ GPa, $\sigma_y = 900$ MPa, $\nu = 0.3$ and $f = 0.28$ (ASM, 2007).

3.4.3 FEA results

FEA results obtained from the simulations, including SEA, peak load (P_{max}), mean crushing force (P_m), densification strain and deformation mode are summarized in Table 3.5. Note that P_m was calculated by using Eq. (3.13),

$$P_m = \frac{\int_0^{\delta_D} P(x)dx}{\delta_D} \tag{3.13}$$

Table 3.5: FEA results.

	P_{max} (kN)	P_m (kN)	SEA (kJ/kg)	Densification strain	Mode
REF_SQ	250.23	125.67	61.45	0.69	—
CAT_455	P_{max} (kN)	P_m (kN)	SEA (kJ/kg)	Densification Strain	Mode
R100_455	83.84	69.52	18.86	0.59	I
R110_455	94.83	79.17	22.28	0.6	I
R120_455	104.54	87.48	25.52	0.61	II
R130_455	114.6	95.67	29.65	0.63	II
R140_455	125.81	103.34	32.56	0.64	II
R150_455	143.61	111.25	35.7	0.64	III
R160_455	168.98	119.92	39.54	0.65	III
R170_455	207.08	129.49	43.75	0.67	III
R180_455	233.63	145.71	51.43	0.70	III
CAT_505	P_{max} (kN)	P_m (kN)	SEA (kJ/kg)	Densification Strain	Mode
R100_505	63.64	59.4	21.66	0.67	I
R110_505	78.4	71.3	26.41	0.66	I

R120_505	92.01	79.23	30.25	0.67	II
R130_505	104.3	83.46	33.19	0.68	II
R140_505	116.25	89.23	36.21	0.69	II
R150_505	132.27	95.99	39.95	0.7	III
R160_505	152.7	102.75	43.69	0.71	III
R170_505	183.07	110.42	47.49	0.72	III
R180_505	209.28	126.09	55.58	0.73	III
CAT_555	P_{max} (kN)	P_m (kN)	SEA (kJ/kg)	Densification Strain	Mode
R100_555	61.54	51.52	19.51	0.65	I
R110_555	70.15	61.93	24.21	0.65	I
R120_555	80.46	72.35	30.21	0.68	II
R130_555	94.05	79.8	34.15	0.69	II
R140_555	109.92	87.1	38.18	0.7	II
R150_555	123.79	93.48	42.32	0.71	III
R160_555	145.91	100.43	46.6	0.73	III
R170_555	171.93	107.9	50.62	0.73	III
R180_555	200.88	123.61	58.84	0.74	III
CAT_GR	P_{max} (kN)	P_m (kN)	SEA (kJ/kg)	Densification Strain	Mode
R100_GR	68.53	58.2	21.12	0.68	I
R110_GR	84.43	69.79	26.14	0.68	I
R120_GR	97.09	78.26	30.1	0.69	II
R130_GR	108.95	85.37	33.65	0.69	II
R140_GR	120.18	92.15	36.9	0.69	II
R150_GR	134.8	98.78	39.96	0.7	III
R160_GR	154.73	106.09	43.35	0.7	III
R170_GR	184.59	113.96	47.29	0.71	III
R180_GR	205.73	129.06	55.29	0.73	III

3.4.4 Deformation modes

Specimens of CAT_505 were chosen as representatives of Miura-ori honeycombs. When the Miura-ori honeycombs were subject to quasi-static axial crushing, they exhibited three different deformation modes owing to different values of edge angle ζ_c. Mode I appeared in specimen of R100_505 and others, see Table 3.5. The schematic crushing process was illustrated in Fig. 3.27(a1). The corresponding equivalent plastic strain (PEEQ) contour maps that represent the material's inelastic deformation, was illustrated in Fig. 3.27(a2). In addition, the PEEQ contour maps were all presented on undeformed shape of the specimen in order to clearly identify the region of plastically deformed area. It collapsed by following the pre-designed origami pattern

in which all flange layers were densified steadily prior to the core layers. Plastic strain appeared along the crease lines in the flange layers first. This was followed by each core layers which deformed simultaneously along the crease lines. Due to the sudden change of boundary condition within each layer, the facets of each core layers not only deformed along the crease patterns but also bent during further compression, resulting in larger area of plastic strain. Finally the whole specimen was densified. Its force-displacement curve is shown in Fig. 3.28(a). The first portion of the curve from 0 to 9 mm indicates the densification process of the flange layers, and the latter portion represents the densification process of the core layers. An obvious plateau in the curve can be seen in this case and in this mode.

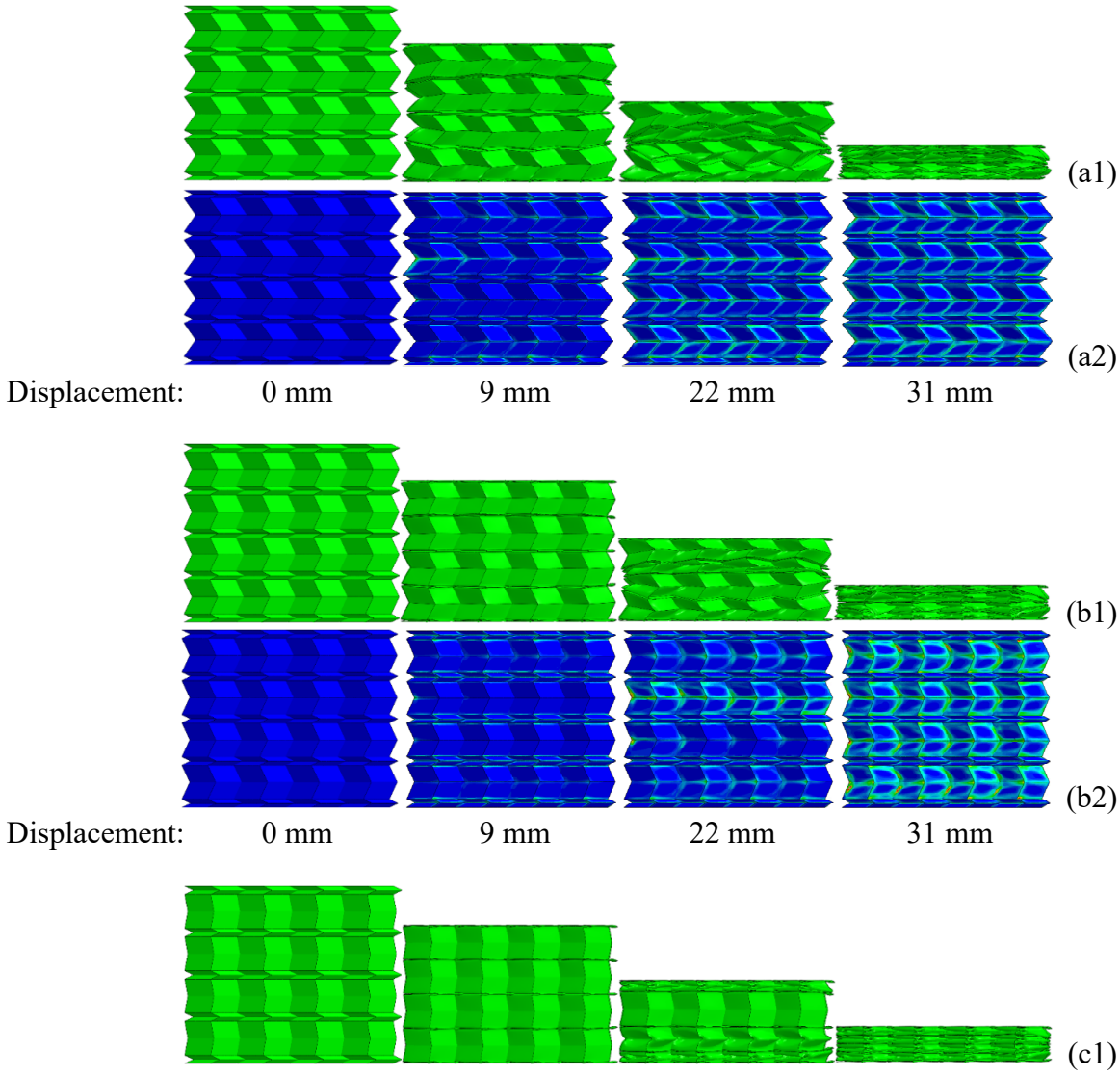

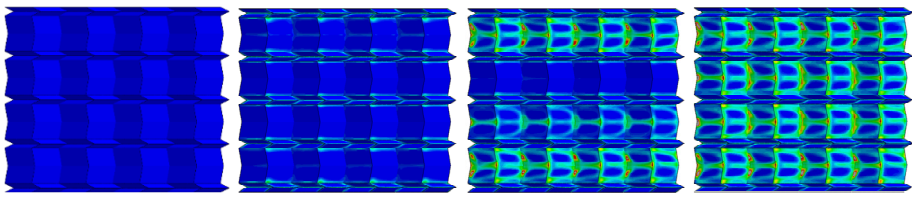

Fig. 3.27 Deformation modes and PEEQ contour maps: (a1) Crushing process of R100_505; (a2) PEEQ contour maps of R100_505; (b1) Crushing process of R130_505; (b2) PEEQ contour maps of R130_505; (c1) Crushing process of R160_505; (c2) PEEQ contour maps of R160_505.

Mode II appeared in specimens R120_505 to R140_505. Take R130_505 as an example. The deformation pattern is shown in Fig. 3.27 (b1) and the corresponding PEEQ contour maps are illustrated in Fig. 3.27 (b2). Under axial compression, the flanges layers are also densified prior to the cores. This phenomenon appears to be more palpable compared to Mode I. Major difference between Modes I and II occurred on the core layers after the densification of flanges. Instead of deforming simultaneously, the middle core layer collapsed first and tends to reach densification prior to other layers. However, this domino effect appears to be quite obscure, this is also reflected on the force-displacement curve as shown in Fig. 3.28 (a). From the plot, the beginning plateau portion (0 to 9 mm) illustrates the densification process of the flanges, followed by the force fluctuation which indicates the collapse of four core layers.

Mode III existed among specimen R150_505 to R180_505. The deformation pattern of specimen R160_505 is shown in Fig. 3.27 (c1) and (c2). When subjected to axial loading, flanges of each layers reached densification in a steady manner and obvious plastic strain occurred along the crease lines. However when compared to Modes I and II, the deformation pattern of core layers differentiated significantly after the densification of flanges. The bottom layer of the core buckled first while other three core layers remain intact. Until it reached densification, the top layer of the core started to buckle and densified. This was followed by the other two layers. In essence, the core collapse layer by layer after the densification of flanges

until the whole specimen is densified. This deformation mode is also clearly illustrated by the force vs displacement curve in Fig. 3.28 (a). Subsequent to the flat portion which indicates the densification process of the flanges, the curve exhibited a significant change in stiffness followed by four sharp waves with distinguished peak loads which indicates the densification process of each core layer, respectively. It can be also found that in group CAT_505, where the specimen is built with the same height of the reference square honeycomb, the peak load of Miura-ori honeycomb can be reduced by more than 50% when compared to the conventional square honeycomb.

It also can be found from the PEEQ contour maps in Fig. 3.27 that when the flange layers are densified, larger areas of plastic deformation occurred along the zig zag creases of the core layers, as well as the area of the connecting edges of the core and flanges layers. This proves the theoretical analysis presented in the previous section.

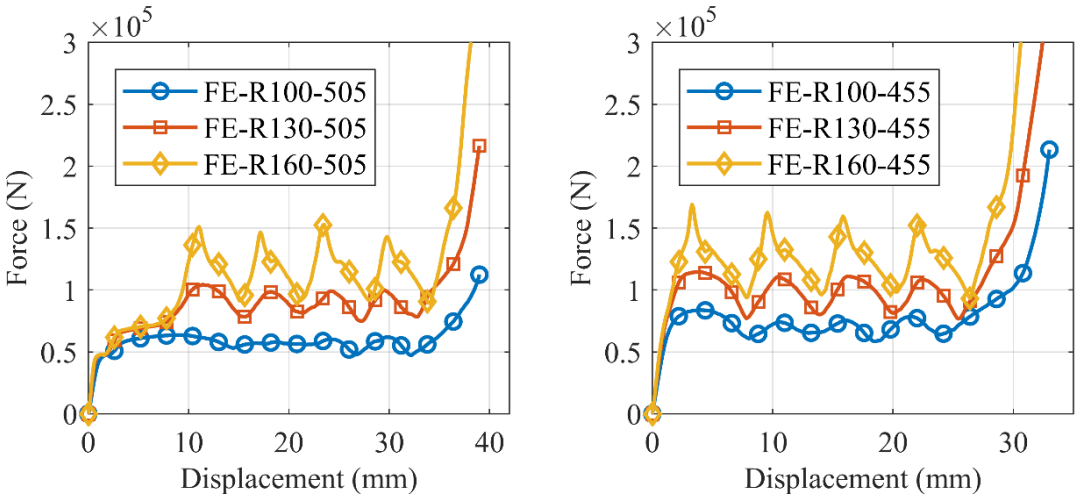

(a) (b)

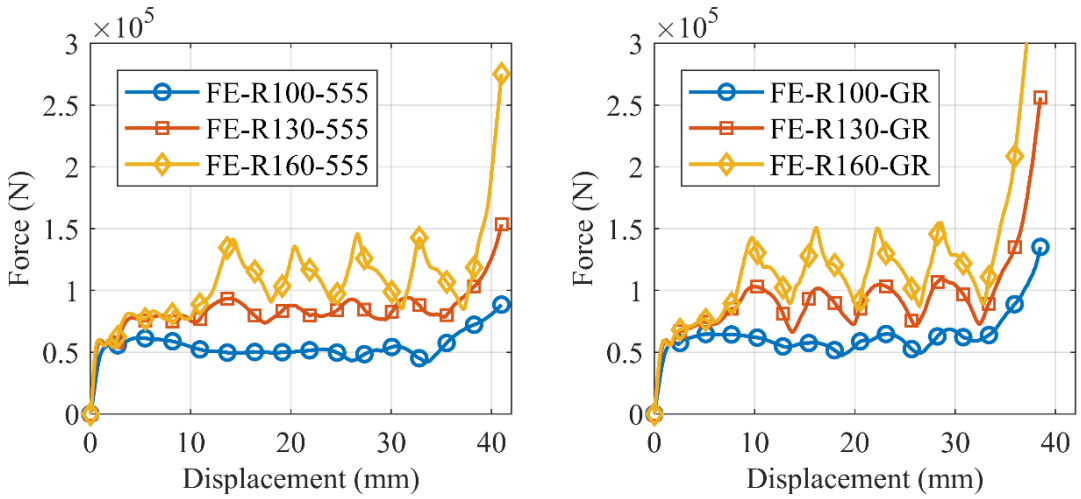

Fig. 3.28 Force-displacement curves: (a) results of representatives from CAT_505; (b) results of representatives from CAT_455; (c) results of representatives from CAT_555; (d) results of representatives from CAT_GR.

The force-displacement curves from other groups that represent relative deformation mode are plotted in Fig. 3.28 (b) to (d), respectively. Three different deformation modes also exist among CAT_455, CAT_555 and CAT_GR, and specimens categorized in each mode are also divided identically as ones in CAT_505. On the other hand, apparent differentia distributed among SEA, peak load, mean crushing force and densification strain.

3.4.5 Discussion

3.4.5.1 Edge-angle configuration of the core

As illustrated in Table 3.5 and Fig. 3.29, the value of SEA, P_m and densification strain increases with the increase of ζ_c. This also happens to the value of P_{max}, which was reflected by the previous theoretical 2D strut model.

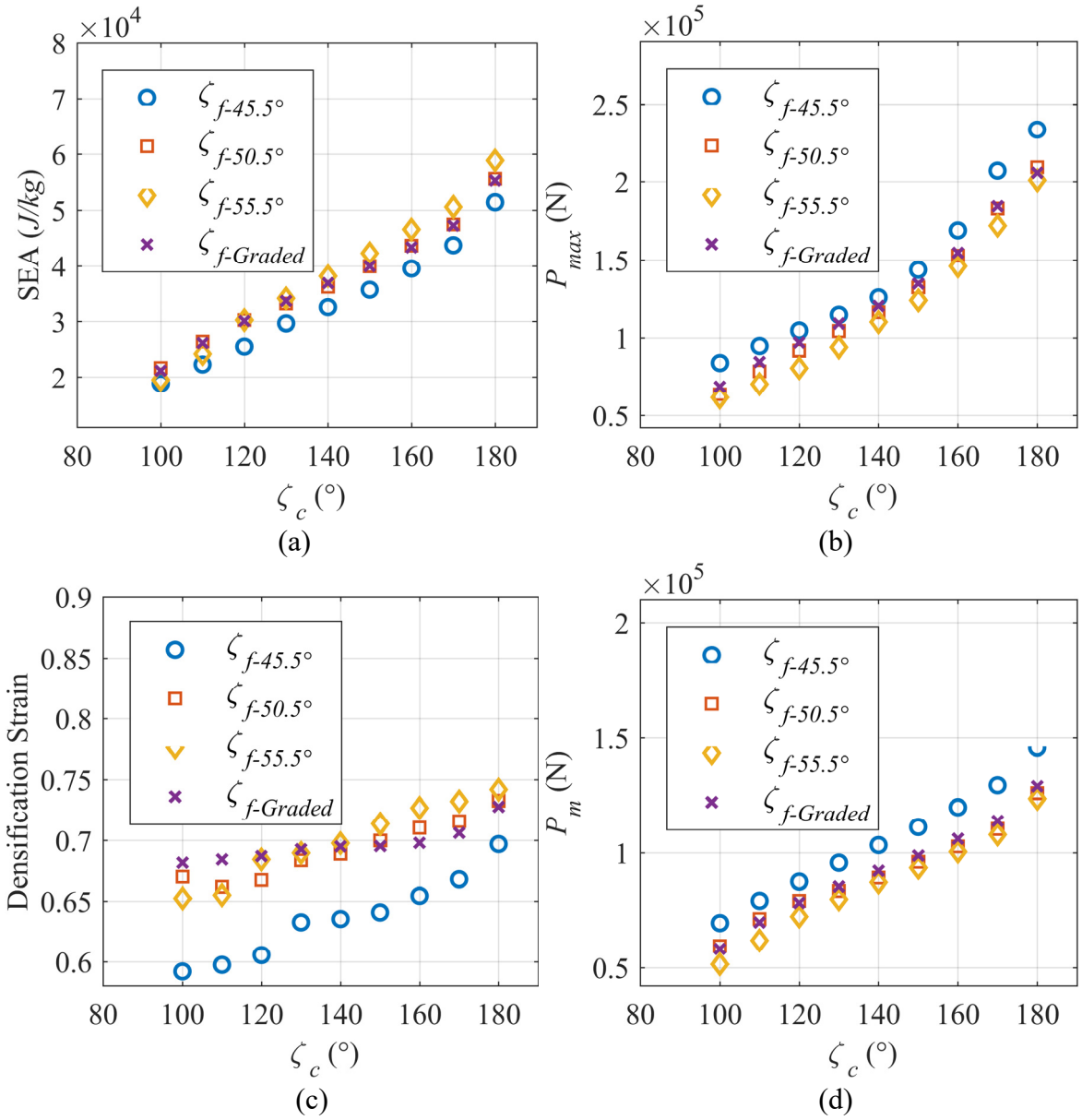

Fig. 3.29 Effect of ζ_c: (a) SEA vs ζ_c; (b) P_{max} vs ζ_c; (c) densification strain vs ζ_c; (d) P_m vs ζ_c.

It is commonly known that reducing P_{max} and increasing P_m at the same time tends to be contradictory, but the Miura-ori honeycomb managed to decrease the peak force by a relative large scale when proper ζ_c is adopted accordingly, as shown in Table 3.5. This means that in terms of actual engineering application, for cases when the force transmission during the crush is vital and need to be minimized, Miura-ori honeycombs built with smaller ζ_c values should be adopted. On the other hand, when energy absorption capacity is priority, Miura-ori honeycombs constructed with greater ζ_c values should be used.

3.4.5.2 Sector-angle configuration of the flange

As shown in Fig. 3.30 (a), the SEA tends to increase with ϕ_f except for the case of R100, and the effect of graded-flange is minor. Fig. 3.30 (b) and (c) illustrate that the P_{max} and P_m tends to decrease with the increase of ϕ_f and the specimens with graded flanges tends to increase the values of P_{max} and P_m compared to the case when ϕ_f = 55.5°. It can be observed from Fig. 3.30 (d) that the flanges possess a major effect on the densification strain, which increases evidently with ϕ_f, in addition to the case of R100.

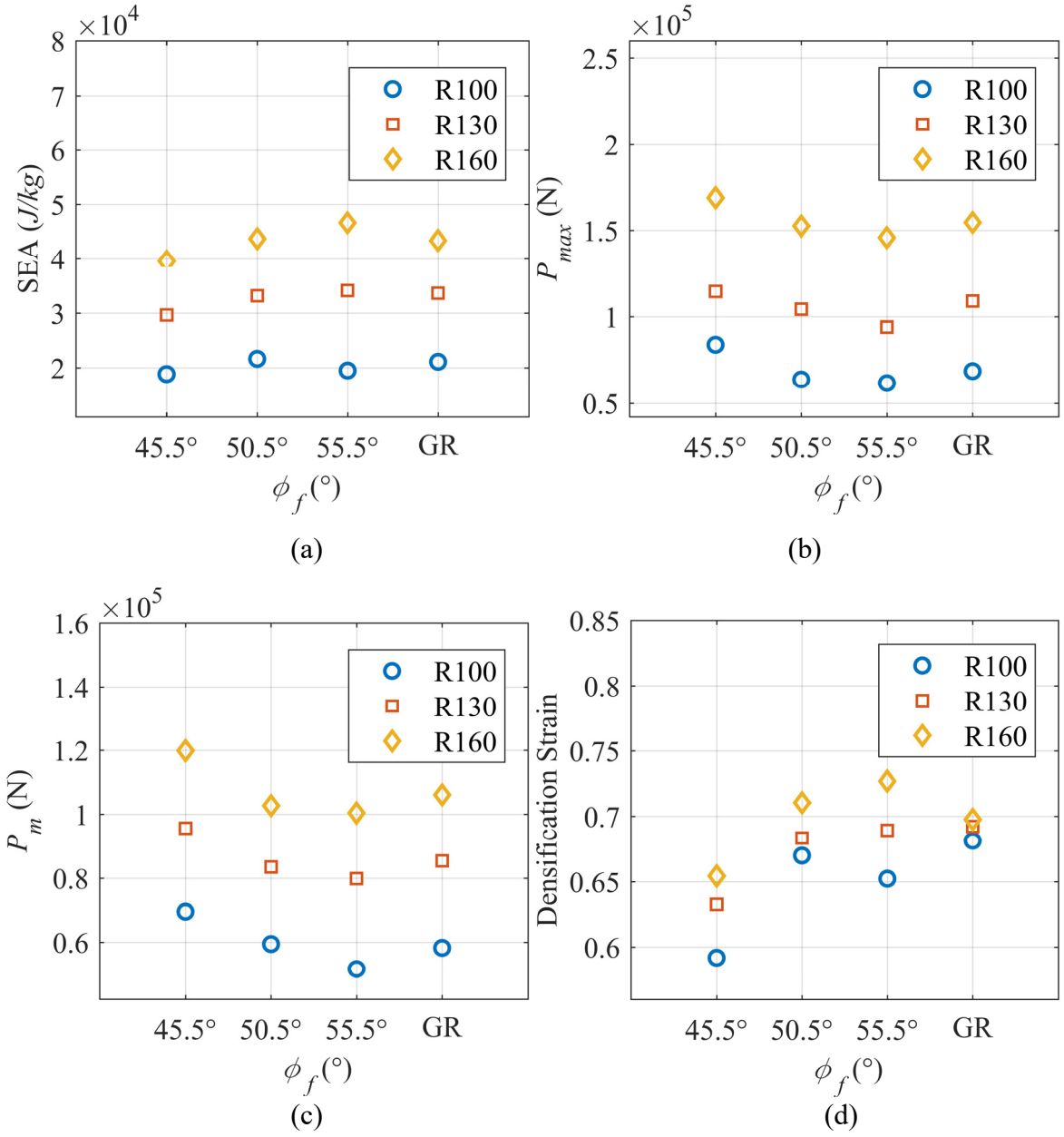

Fig. 3.30 Effect of ϕ_f: (a) SEA vs ϕ_f ; (b) P_{max} vs ϕ_f ; (c) P_m vs ϕ_f ; (d) densification strain vs ϕ_f.

It can be noted from the PEEQ contour maps of specimen R100_455 and R100_555 in Fig. 3.31 that larger areas of plastic deformation spread along the zig zag creases of the core layers, as well as the area of the connecting edges between the core and flanges layers. According to the previous discussion, R100_455 should have swiped more plastic area along the zig zag creases of the core layers than R100_555. However, by comparing the plastic deformation regions in Fig. 3.31, the above assumption did not occur. This can be explained by the following discussion.

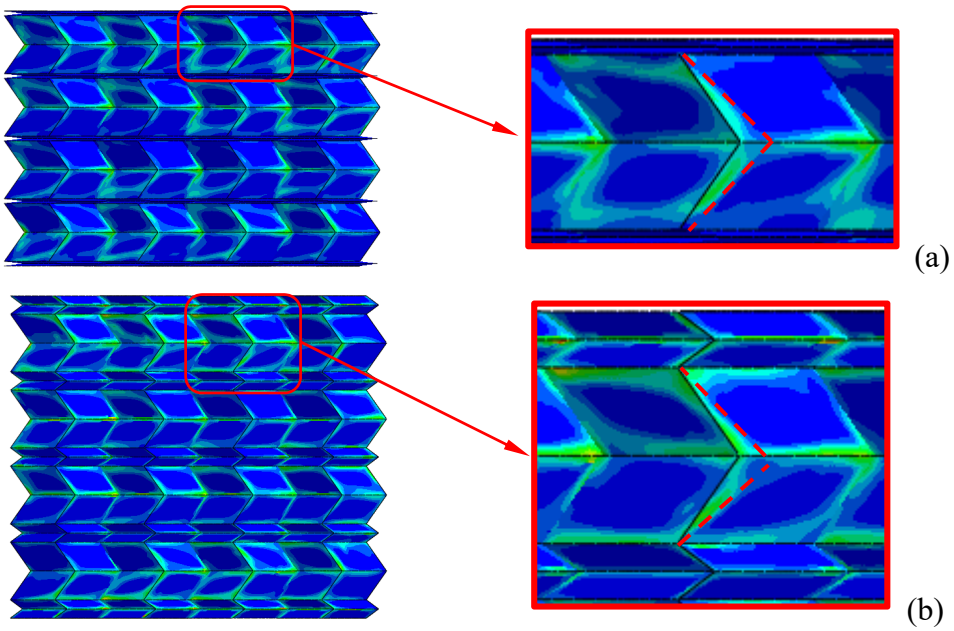

Fig. 3.31 PEEQ contour maps: (a) R100_455; (b) R100_555.

First of all, the flange layers of the specimen R100_455 are basically in a flattened state at the very beginning. Thus, it reduces the influence of ϕ_f on the plastic deformation along the zig zag regions of the core layers. Secondly, also due to the initially almost flattened flange configurations of R100_455, there is no noticeable plastic deformation in the flange layers. However in the case R100_555, the plastic deformation region is quite obvious. Because the flanges are built with same mass, it is obvious that the design of flange configurations with a larger value of ϕ_f is more ideal, meanwhile it is also easier for manufacturing process.

3.4.5.3 Wall thickness

In order to study the effect of wall thickness on the deformation mode, specimens of R100_505, R130_505 and R160_505 with identical TC4 material properties are chosen as representatives of Mode I-III from CAT_505, and wall thickness of *0.25mm* and *1mm* is assigned to each specimen, respectively. The results of numerical simulations are summarized in Fig. 3.32 and Table 3.6.

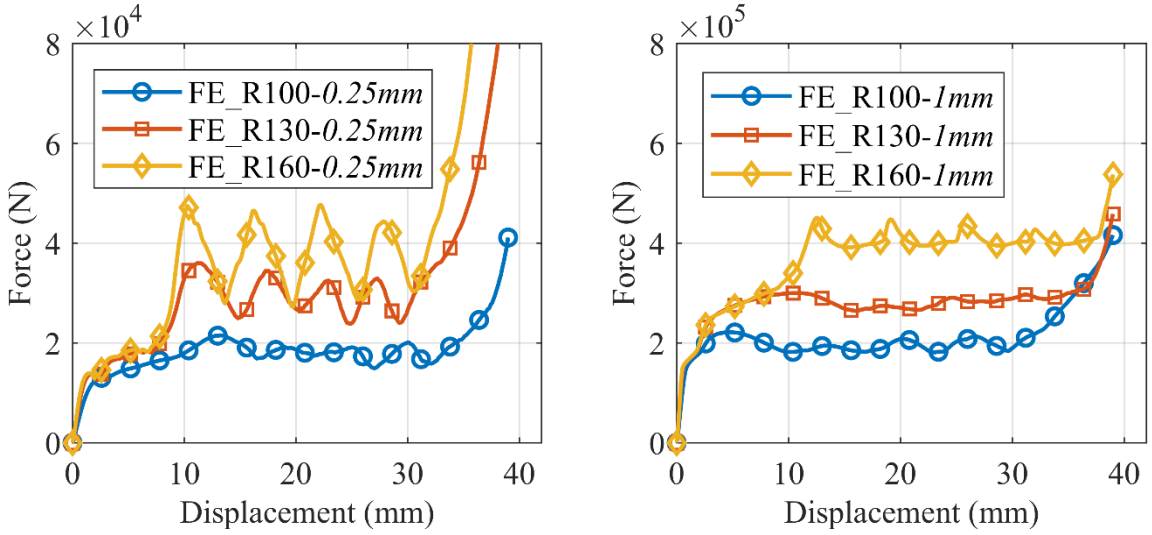

(a) (b)

Fig. 3.32 Force-displacement curves (thickness effect): Results of representatives with thickness of (a) 0.25 mm and (b) 1 mm.

Table 3.6: FEA results of thickness effect.

	P_{max} (kN)	P_m (kN)	SEA (kJ/kg)	Densification Strain	Deformation mode
R100-0.25mm	21.54	17.06	12.44	0.67	I
R130-0.25mm	36.03	25.53	18.12	0.61	II
R160-0.25mm	47.66	31.81	24.38	0.64	III
R100-1mm	229.51	193.98	36.05	0.68	I
R130-1mm	314.71	274.26	61.15	0.76	I
R160-1mm	450.8	364.26	85.59	0.79	II

It can be noted that when the wall thickness is reduced by two times, the structure of corresponding mode remains deforming in the same mode before the change, and the change is

only correspondingly reduced in the magnitude of load. However, when the thickness is increase by two times, the deformation pattern of all specimens remain relative constant, that is, an obvious long plateau region exists in each curve instead of obvious fluctuations compared to the other cases. This phenomenon indicates that by increasing the thickness, it will decrease the influence of the boundary effect which resulting in a more flat and ideal force-displacement relation. Moreover, by comparing Table 3.5 and Table 3.6, it can be seen that the SEA of specimens with wall thickness of 1mm have been increase significantly, especially in the case of R130-1mm and R160-1mm. In essence, by increasing the wall thickness of the Miura-ori honeycomb, it will optimize the deformation pattern and increase the energy absorption capacity. Therefore, the wall thickness of Miura-ori honeycomb can be appropriately increased to adjust the energy absorbing capacity in order to adapt to the actual needs.

3.4.5.4 Property of base material

In order to study the effect of base material properties on the Miura-ori honeycomb, specimens of R100_505, R130_505 and R160_505 from CAT_505 are chosen as representatives and properties of typical aluminum and 3D-printed plastic are assigned to each specimen, respectively. The aluminum was modelled as an elastic perfect-plastic material with $\rho = 2700$ kg/m^3, $E = 70$ GPa, $\sigma_y = 290$ MPa, $\nu = 0.35$ and $f = 0.25$ (Horrigan, *et al*., 2000, Besant, *et al*., 2001, Chen, *et al*., 2001). The results of numerical simulations are summarized in Fig. 3.33 and Table 3.7.

Table 3.7: FEA results of material effect.

	P_{max} (kN)	P_m (kN)	SEA (kJ/kg)	Densification Strain	Deformation mode
R100-*Al*	22.43	20.15	12.15	0.68	I
R130-*Al*	36.48	29.22	19.29	0.7	II
R160-*Al*	53.2	36.3	25.56	0.72	III
R100-*Hyb*	0.24	0.2	0.32	0.69	I
R130-*Hyb*	0.51	0.38	0.71	0.74	I
R160-*Hyb*	0.71	0.48	0.88	0.71	I-II

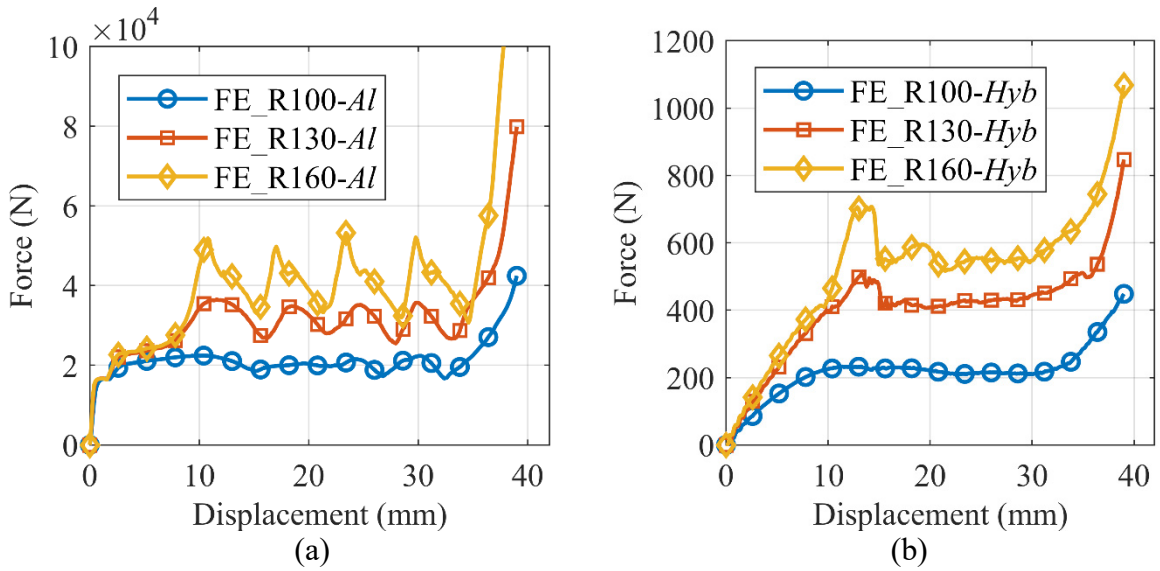

Fig. 3.33 Force-displacement curves (material effect): (a) Results of aluminum representatives; (b) results of hybrid-plastic representatives.

It can be noted that the representatives made of aluminum deform in same respective modes as those made of TC4. However, when the material of 3D-printed plastic is assigned to the representatives, the Miura-ori honeycombs tend to deform only in Mode I and II, where a relatively long plateau region is followed after the peak. By comparing Table 3.5 and Table 3.7, it is obvious that the SEA of specimens made of 3D-printed plastic have been decreased dramatically, however the load uniformity is better. This indicates that choosing proper materials is vital for the Miura-ori honeycomb.

3.5 Summary

A unique origami-inspired Miura-ori honeycomb has been designed in order to obtain low peak force and high energy absorption capacity. Experimental and numerical results are presented to study the mechanical behaviors of the honeycomb. Especially, it is found that with proper design, this unique honeycomb with special self-locking feature can reduce the peak force by more than 50% when compared to the conventional square honeycomb, and remain efficient in the SEA. Effects of design parameters can be summarized as follows:

1) The flange layer plays a very important role of increasing the energy absorption capacity of the core layer. By changing the boundary condition of the core, it can not only increase the area of plastic deformation along the connecting edges between flanges and cores, but also increase a larger area of plastic deformation around the zig zag creases of the core layers.
2) The sector angle ϕ_f controls the triggering of the self-locking feature of the Miura-ori honeycomb as ϕ_f is designed to be always smaller than ϕ_c. However, the sector angle ϕ_f with an aptly large value is beneficial for increasing the SEA.
3) The edge angle ζ_c (sector angle ϕ_c) plays the most important role of controlling the deformation pattern as well as SEA and peak force. It is apparent that the greater value of ζ_c is, the higher SEA will be, but the peak force will be also increased at the same time. In order to maintain reasonable high SEA and achieve relatively lower peak force, proper design such as adjusting the wall thickness of the structure and using more suitable material can be considered.
4) The wall thickness of Miura-ori honeycomb can influence the deformation mode, as well as the SEA in a great manner, the results have shown that properly increasing wall thickness can optimize the deformation pattern of the structure and increase the SEA significantly.
5) The mechanical properties of the base material also play an important role in terms of deformation mode and peak force P_{max}. It seems that the Miura-ori honeycomb made of 3D-printed plastic materials has better load uniformity. However, typical metal materials are more efficient in term of SEA.

In conclusion, this chapter has proposed a novel concept of origami-inspired honeycomb that optimizes the drawbacks of conventional honeycombs which exhibits exceedingly high peak force with inefficient deformation pattern during crush. This work proves that the concept of Miura-ori can be efficiently adopted to design an ideal energy absorbing material, and numerous

origami patterns created by origami artists could also be potentially beneficial for the design of innovative energy absorbing metamaterials, as presented in the next chapter.

Chapter 4

Derivative Miura-ori-based honeycombs

This chapter presents the study of the energy absorption capacity and relevant mechanical properties of derivative Miura-ori-based tetragonal honeycombs under quasi-static compression. Parametric studies were conducted in order to investigate the geometric influence on derivative cores, and the effect of the hybridization of derivative cores are discussed.

4.1 Geometric design

4.1.1 Miura-ori core

The first derivative Miura-ori-based honeycomb is the essential Miura-ori core. It is built on the conventional Miura-ori pattern as illustrated in Fig. 4.1 (a), the dashed and dash-dotted lines represents hill and mountain folds, respectively. According to the design, a piece of folded pattern is shown in Fig. 4.1 (b).

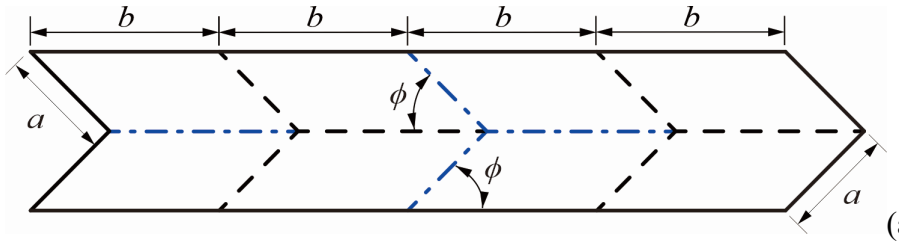

(a)

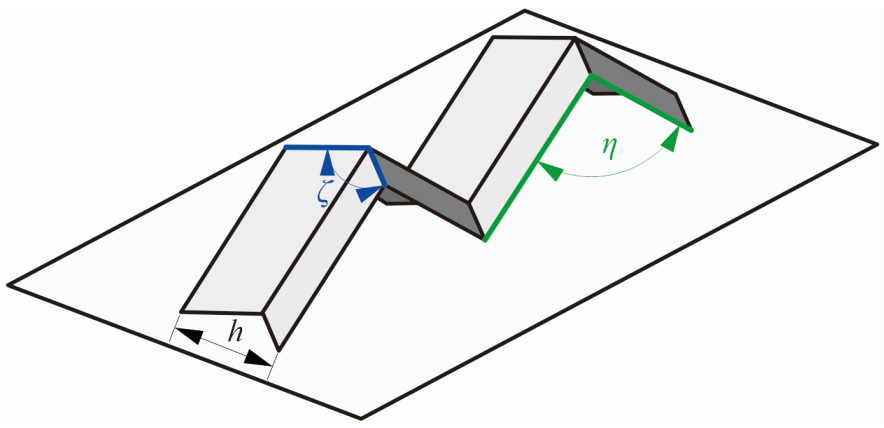

(b)

Fig. 4.1 The pattern of Miura-ori core: (a) Miura-ori pattern; (b) a piece of folded pattern.

The geometric relations can be explained by the following equations,

$$(1+\cos\zeta)(1-\cos\eta)=4\cos^2\phi \tag{4.1}$$

$$h=2a\sin(\zeta/2) \tag{4.2}$$

where, a and h represent the side length and height of unit cell, respectively. ζ and η denote edge angles.

By folding four pieces of the above pattern to the same extent and connecting the ridges, as shown in Fig. 4.2 (a), a unit of Miura-ori core can be created. A single tetragonal cell in this unit is shown in Fig. 4.2 (b).

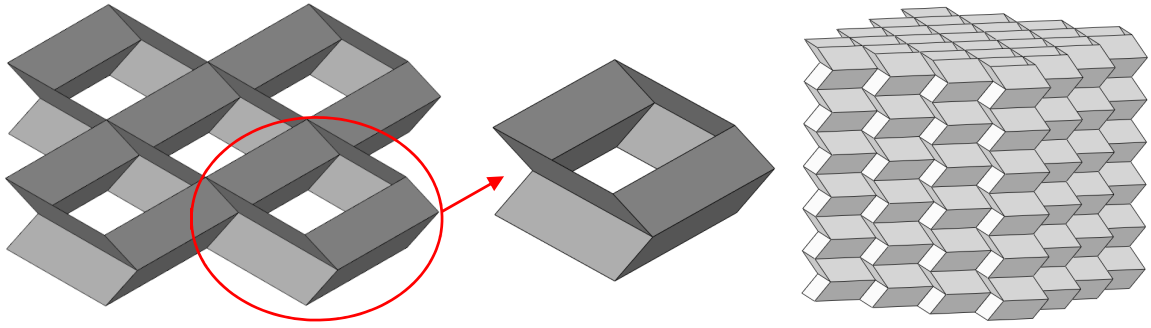

(a) (b) (c)

Fig. 4.2 Miura-ori core: (a) A unit of Miura-ori core; (b) Miura-ori cell; (c) Miura-ori core.

All honeycombs studied in this chapter are built with six layers, and each layer is composed of 16 identical cells in a four by four configuration. Hence, the configuration of a Miura-ori core studied in this chapter is indicated in Fig. 4.2 (c).

4.1.2 C-crease core

The design of derivative C-crease core is based on the Miura-ori core. The shape of C-crease is created by replacing the zig zag crease in the Miura-ori core to a c-shaped curve. This c-shaped curve is not formed arbitrarily, instead it is a determinable elliptic curve constructed according

to a specific geometric design. The following explains how C-crease core is created and how c-shaped crease is determined.

First, based on a folded pattern of Miura-ori core, a coordinate system u'-v' is created in the plane of the zig zag crease. Then, create an ellipse based on the vertex (A, B and C) of the zig zag, as indicated in Fig. 4.3 (a). The elliptical curve intercepted by these vertices is the required C-crease. By using the same method, replace other zig zag creases with this C-crease, and use curved surfaces to connect the neighbouring C-creases between different planes, a piece of C-crease core can be obtained, as shown in Fig. 4.3 (b).

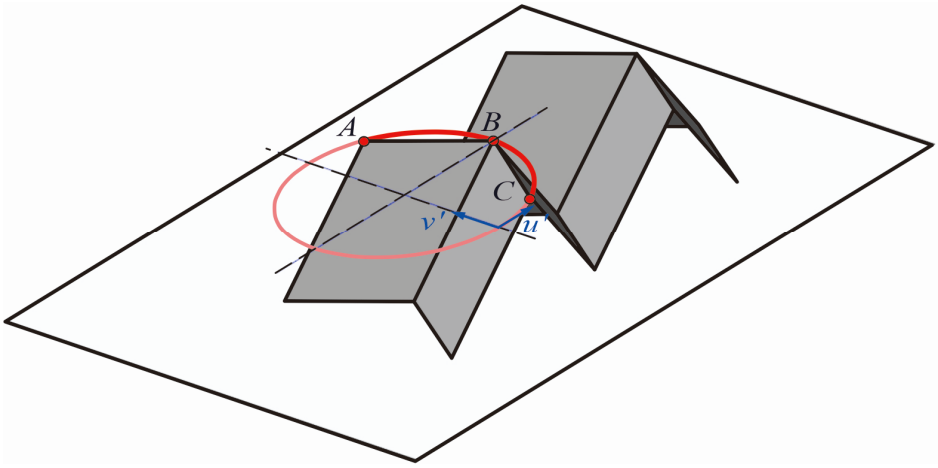

(a)

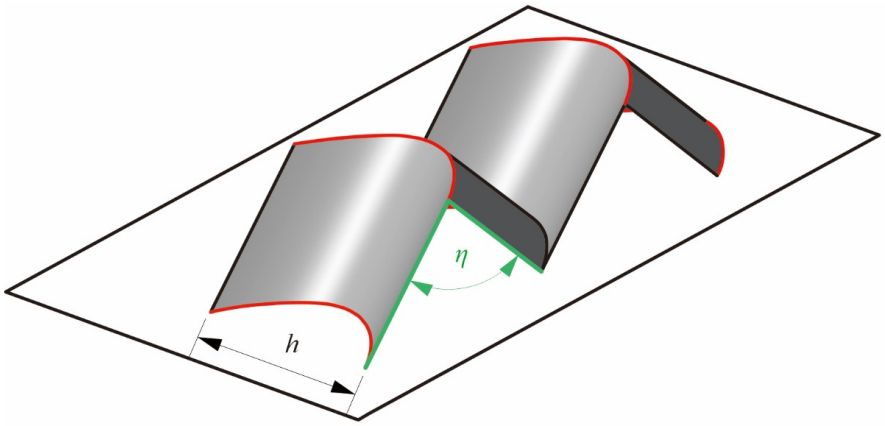

(b)

Fig. 4.3 Realization of C-crease: (a) Foundation of C-crease; (b) a piece of C-crease core.

By using the same method and connecting four identical pieces of this C-creased structure as shown in Fig. 4.3 (b), a unit of C-crease core can be established, as illustrated in Fig. 4.4 (a). A

single C-crease cell is indicated in Fig. 4.4 (b). The configuration of a C-crease core is depicted in Fig. 4.4 (c).

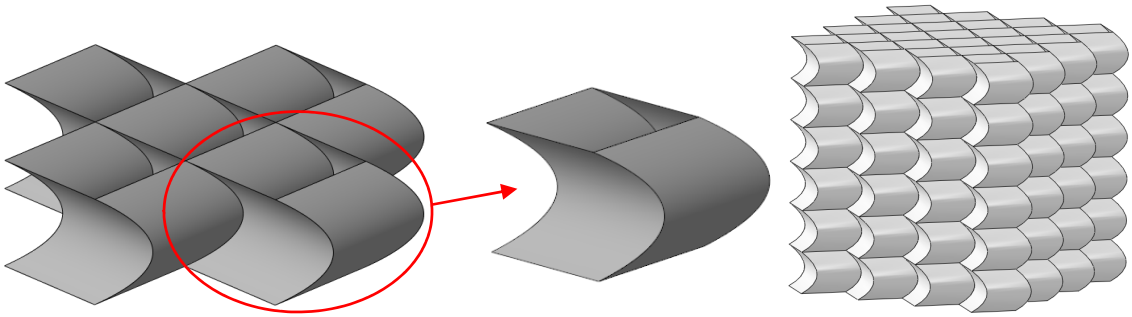

(a) (b) (c)

Fig. 4.4 C-crease core: (a) A unit of C-crease core; (b) C-crease cell; (c) C-crease core.

The process of determining the ellipse is explained as following (Gattas and You, 2014b).

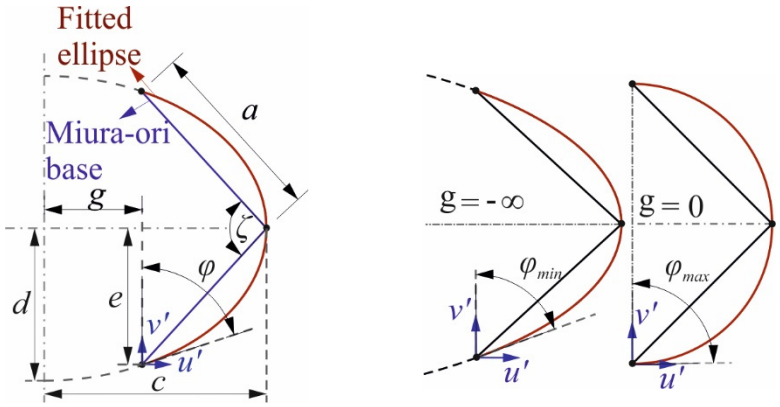

(a) (b)

Fig. 4.5 Determination of the C-crease elliptical curve: (a) Ellipse configuration; (b) minimum and maximum gradient parameter.

The $u'-v'$ plane is coplanar to that formed by vertices along the zigzag folds, and the ellipse in this plane can be generally defined as:

$$\frac{(u'-g)^2}{c^2}+\frac{(v'-e)^2}{d^2}=1 \tag{4.3}$$

where c, d, g, and e are the ellipse coefficients.

In order to determine theses 4 ellipse coefficients and the relevant ellipse, an additional parameter is specified as the gradient parameter φ, which is the initial gradient of the elliptical curve in the $u' - v'$ plane, as shown in Fig. 4.5 (a). Then the ellipse can be determined by the following equations.

$$e = B/2 \tag{4.4}$$

$$g = \frac{2C^2}{[4C - B\tan\varphi]} \tag{4.5}$$

$$c = C - g \tag{4.6}$$

$$d = B/2\sqrt{1/(1-\frac{g^2}{c^2})} \tag{4.7}$$

where

$$B = 2a\sin(\zeta/2) \tag{4.8}$$

$$C = a\cos(\zeta/2) \tag{4.9}$$

The gradient parameter φ has a maximum and minimum limit (φ_{max} and φ_{min}) which corresponds to maximum and minimum values of coefficient g, at g = -∞ and g = 0, respectively, as shown in Fig. 4.5 (b). By substituting these values of g into equation (4.5), it allows these limits to be determined as follows.

$$\varphi_{\max} = \pi/2, \text{ when } g = 0 \tag{4.10}$$

$$\varphi_{\min} = 4C/B, \text{ when } g \to -\infty \tag{4.11}$$

The ellipse can also be express as a parametric function of t, where $-t_{\lim} \le t \le t_{\lim}$,

$$u' = g + c\cos t \tag{4.12}$$

$$v' = e + d\sin t \tag{4.13}$$

$$t_{\lim} = \arctan\frac{cB}{2dg} \tag{4.14}$$

Thus, the length *S* of the c-shaped curve (arc) can by calculated by integral approximation of Eq. (4.15).

$$S = 2\int_0^{t_{\lim}} \sqrt{c^2 \sin^2 t + d^2 \cos^2 t}\, dt \tag{4.15}$$

This c-shaped elliptical curve that was projected on the frame of a folded Miura-ori pattern can be unrolled to a flat surface in order to obtain a pattern. This can be achieved in the following two steps (Gattas and You, 2014b).

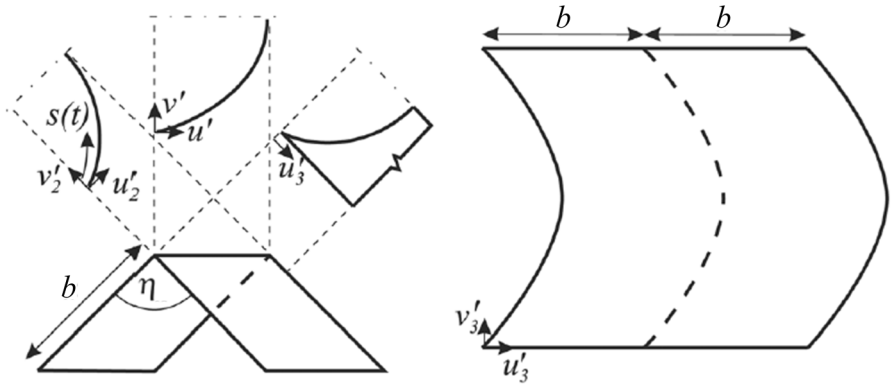

(a) (b)

Fig. 4.6 Unrolling of C-crease: (a) Ellipse projection; (b) unrolled pattern.

First, along the axes of each folding direction, the original ellipse is projected as shown in Fig. 4.6 (a). A new ellipse is obtained in the $u_2' - v_2'$ plane which is the perpendicular section of the deployable surface, the coordinate in the *v* direction is unchanged but a scale factor is applied in the *u* direction which can be expressed as Eq. (4.16),

$$u_2' = u' \frac{\cos(\eta/2)}{\sin\eta} \tag{4.16}$$

$$v_2' = v' \tag{4.17}$$

For the second step, unroll the projected ellipse onto the $u_3' - v_3'$ plane, the coordinate in the u direction is unchanged, but in the v direction the coordinate now equals to the $u_2' - v_2'$ elliptical arc length $S(t)$ up to coordinate u.

$$u_3' = u_2' \tag{4.18}$$

$$v_3' = S(t) \tag{4.19}$$

4.1.3 S-crease core

The derivative S-crease core can be built on a special Miura-ori pattern, which is illustrated in Fig. 4.7 (a). According to the design, a piece of folded pattern is shown in Fig. 4.7 (b) and there geometric configurations can also be determined by using Eq. (4.1) and (4.2).

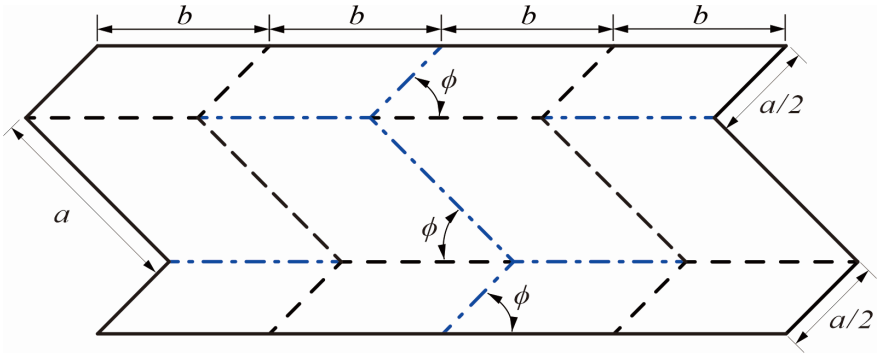

(a)

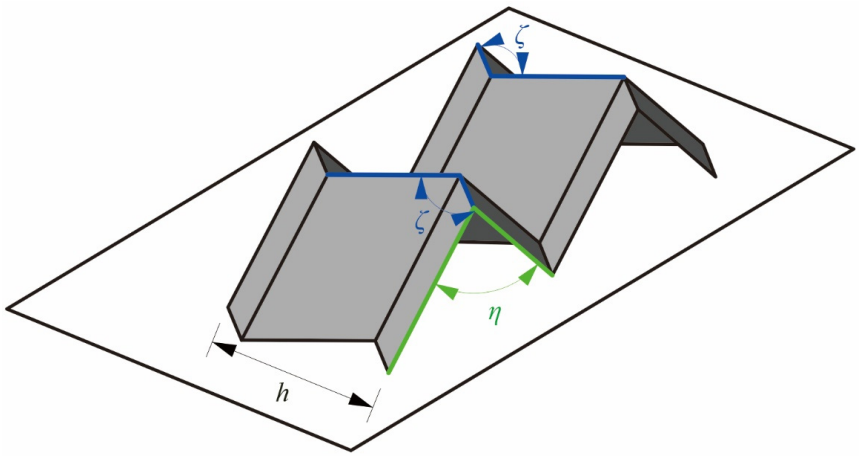

(b)

Fig. 4.7 A special Miura-ori: (a) Pattern; (b) a piece of folded pattern.

Then, use the same method as before to create ellipses on the zig zag creases and obtain relevant c-shaped elliptical curves. By connecting two adjacent c-shaped elliptical curves on the same plane, a s-shaped crease is then formed, as indicated in Fig. 4.8 (a) (point C is the midpoint of the crease line BD). By employing the same method, replace other zig zag creases with this S-crease, and use curved surfaces to connect the neighbouring S-creases between different planes, Fig. 4.8 (b) can be obtained.

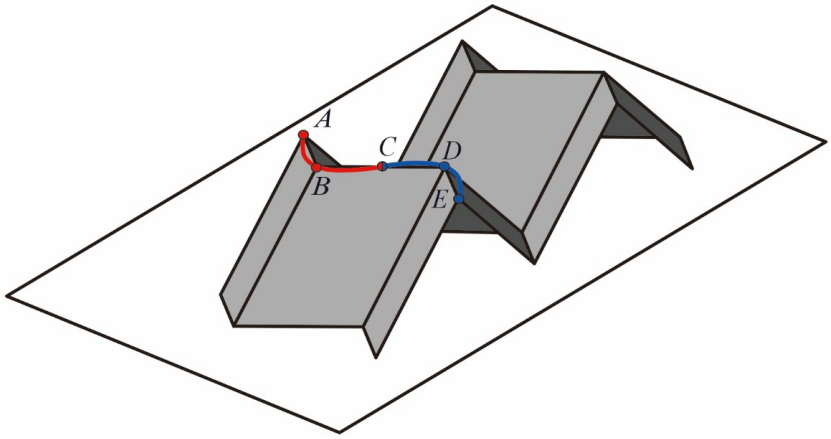

(a)

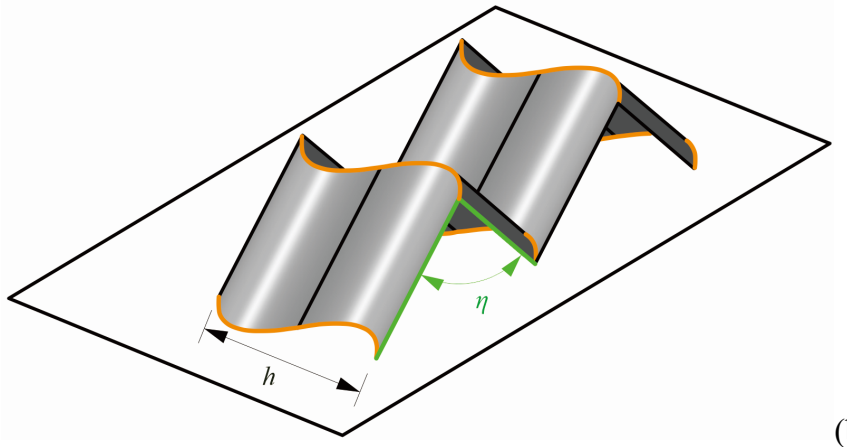

(b)

Fig. 4.8 Realization of S-crease: (a) Foundation of S-crease; (b) a piece of S-crease core.

By connecting four identical pieces of this S-creased structure by using previous method, a unit of S-crease core can be established, as shown in Fig. 4.9 (a). A single S-crease cell is illustrated in Fig. 4.9 (b) and a S-crease core is indicated in Fig. 4.9 (c).

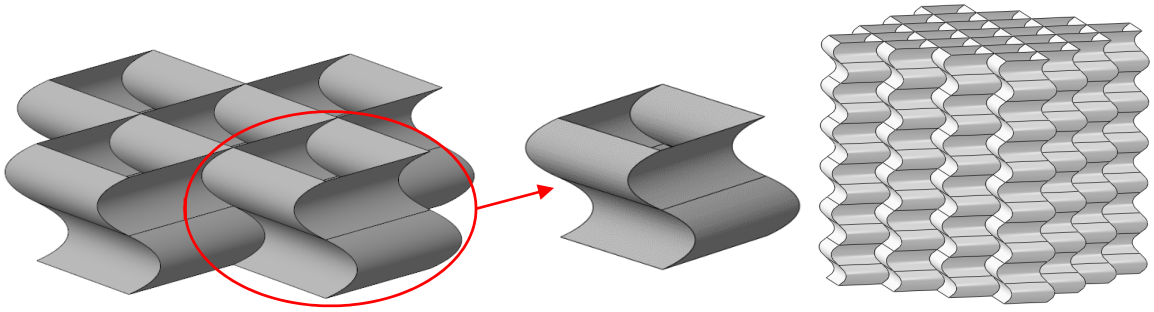

(a) (b) (c)

Fig. 4.9 S-crease core: (a) A unit of S-crease core; (b) S-crease cell; (c) S-crease core.

Since the design principle of S-crease is substantially the same as that of the C-crease, its geometric parameters can be determined by using the same method as explained in previous section. It should be noted that because the shorter side length of the frame of the S-crease core equals *a/2*, the length of the S-crease is hereby equal to the length of the C-crease.

4.1.4 Hybrid origami-honeycombs

The hybrid origami-honeycomb designed in this section is created by combining layers of Miura-ori, C-crease and S-crease honeycomb units that proposed previously. Since the cross-sections of each unit in the out-of-plane direction can be designed with identical configurations, they can be arbitrarily combined in this direction when the cross-sections are the same. Figure 4.10 shows an example of a hybrid origami-honeycomb built by layers of Miura-ori, C-crease and S-crease honeycomb units. Each layer consists of 16 identical cells of derivative cores. As the stiffness of each layer is different, the hybrid origami-honeycomb can possess different stiffness gradient with relative assembly.

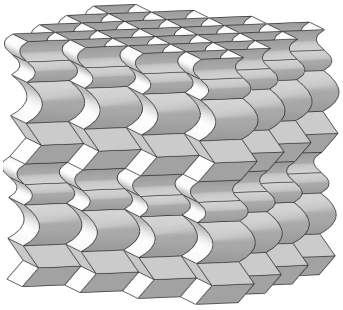

Fig. 4.10 Example of hybrid origami-honeycomb

4.2 Experiments

To evaluate the actual characteristics of derivative cores preliminarily, quasi-static compression tests in out-of-plane direction were carried out on samples of derivative cores. Experimental specimens were 3D-printed by using the same 3D-printed plastic as adopted preciously. All specimens were constructed with six layers and each layer contains 16 cells built in a four by four configuration, as indicated in Fig. 4.11.

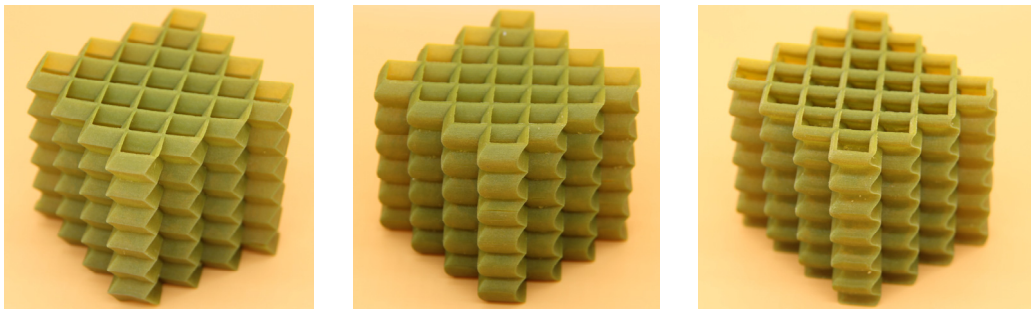

(a) (b) (c)

Fig. 4.11 Test model of derivative Miura-ori-based honeycomb cores: (a) Miura-ori core; (b) C-crease core; (c) S-crease core.

Four sets of experimental specimens were 3D-printed and each set contained two identical samples. Sets 1, 2 and 3 consist specimens of Miura-ori, C-crease and S-crease cores, respectively, whereas set 4 comprises of two conventional square honeycombs (R_SQ) as the reference. Dimensions of test samples are listed in Table 4.1 and all specimens were built with thickness of 0.5mm. In addition, for the C-crease and S-crease core, the value of φ was defined to be 60°. The displacement controlled loading condition was applied with a constant crushing speed of 2mm/min.

Table 4.1: Dimensions of experimental samples.

Cores	ϕ	ζ	η	a (mm)	b (mm)	height (mm)
Miura-ori	63.00°	100.00°	90.00°	6	10	55.2
C-crease	63.00°	100.00°	90.00°	6	10	55.2
S-crease	63.00°	100.00°	90.00°	3	10	55.2

The force-displacement curve obtained from the test is summarized in Fig. 4.12. The results from sets 1 to 3 illustrates three stages of deformation. At the beginning, the force increased linearly until a plateau was reached (stage 1). At stage 2, the load remained more or less constant and the structure deforms uniformly. During the last stage, the force increased rapidly because of the densification of the structure. For the conventional square honeycomb (set 4), it also had three stages. For stage 1, the load increased rapidly until reaching a relatively high peak force. In stage 2, the load dropped considerably until reaching approximately the magnitude of half of the peak load. In the final stage, the force started to increase again steadily as the structure further collapsed with some facets touched the bottom platen and densification occurred.

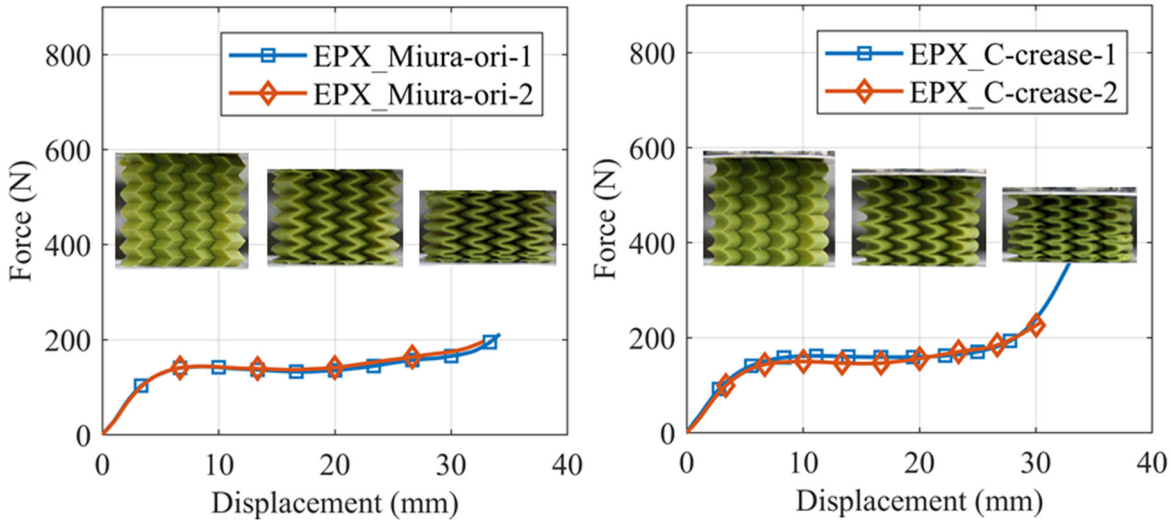

(a)

(b)

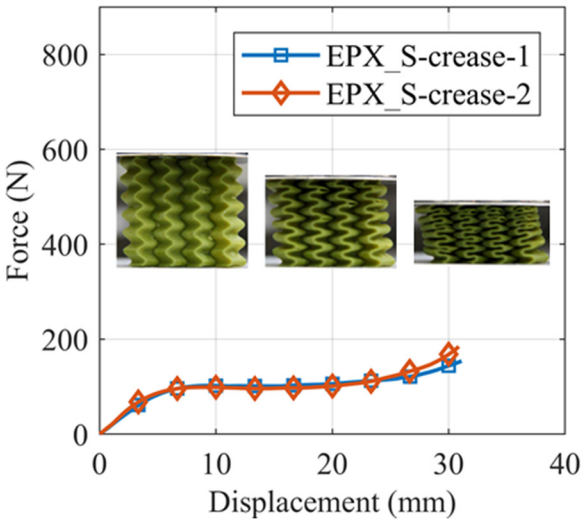

(c)

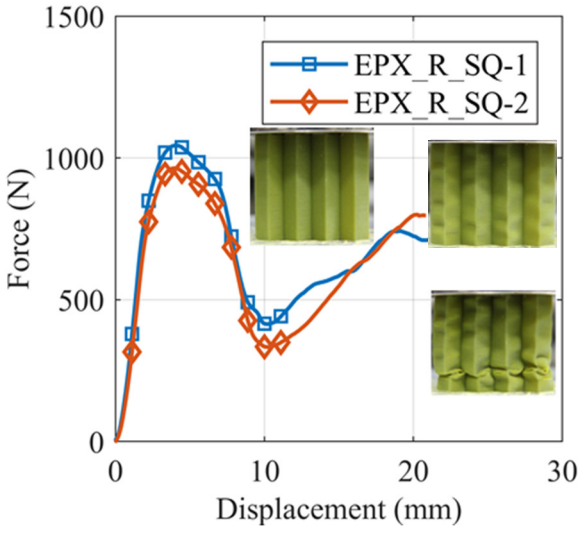

(d)

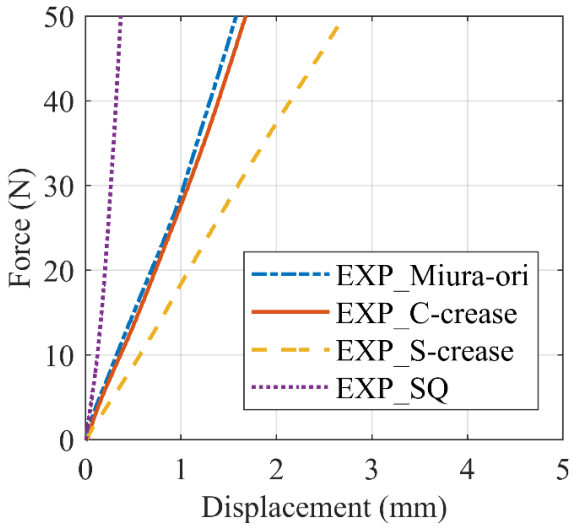

(e)

Fig. 4.12 Force-displacement curves of experimental specimens: (a) Miura-ori core; (b) C-crease core; (c) S-crease core; (d) reference square honeycomb; (e) illustration of initial stiffness variation among different honeycombs.

It can be found that the derivative Miura-ori-based honeycomb cores are effective in reducing the peak load comparing to the conventional honeycomb. Also the shapes of the force-displacement curves are desirable as energy absorption structures. Furthermore, each core type exhibited different stiffness as shown in Fig. 4.12 (e). In order to further explore the influence and benefits of the derivative cores and their hybridization in energy absorption, comprehensive study is conducted numerically and introduced in the next section.

4.3 Finite element analysis

The finite element analyses in this chapter were conducted to study the energy absorption capacity of derivative Miura-ori-based honeycombs under quasi-static compression, as well as geometric influences. Abaqus/explicit (2016) and PTC Creo (2018) were employed for numerical modeling.

4.3.1 Finite element model and validation

The crushing scenario was modeled in the same way of previous Chapter. The derivative Miura-ori-based honeycomb was placed between two rigid panels with the bottom plate fixed completely, whereas all degrees of freedom of the moving upper plate were constrained except for the uniaxial loading direction. A small gap of 0.1mm was left between the upper plate and the specimen to avoid initial penetration. Displacement controlled boundary condition was applied to the upper plate to simulate the loading process and the crushing distance was set to be approximately 80% of the specimen height. Four-node shell elements with reduced integration, S4R, was employed for meshing. Self-contact was defined, which took into account hard contact and friction between panels and honeycomb samples.

Primary finite element analyses were conducted by simulating the previous compression tests, and the FE model was validated by comparing the numerical results against the experimental ones. An elastic perfect-plastic material constitutive model of the 3D-printed plastic are implemented in Abaqus/explicit. The material properties are: $\rho = 1020$ kg/m^3, $E = 80$ MPa, $\sigma_y = 10.5$ MPa, $\nu = 0.3$, and $f = 0.25$. The ratio of artificial strain energy to internal energy, and the ratio of kinetic energy to internal energy were checked to be both less than 5% to ensure the accuracy of simulation. Figure 4.13 shows the force-displacement curves and deformation pattern from the simulation and test.

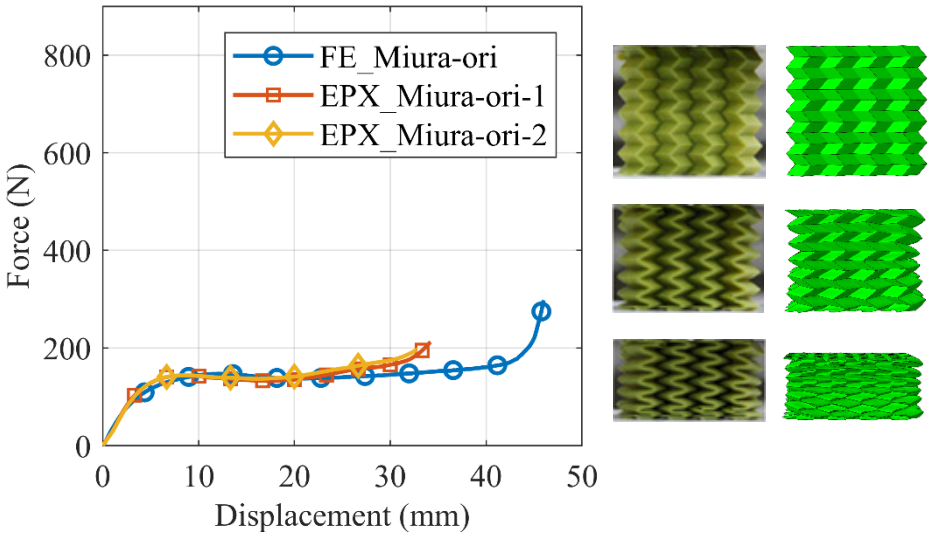
FE_Miura-ori
EPX_Miura-ori-1
EPX_Miura-ori-2
Force (N)
Displacement (mm)
0
200
400
600
800
0
10
20
30
40
50

(a)

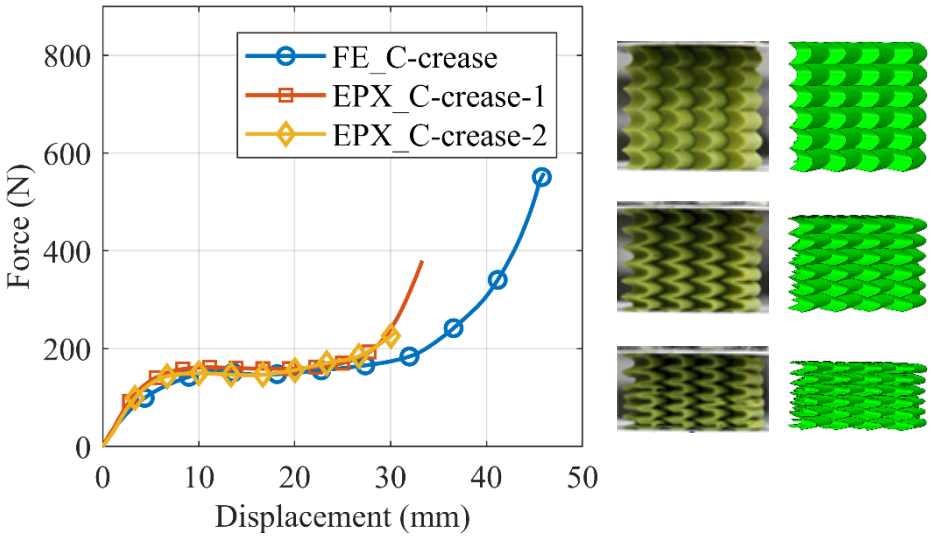
FE_C-crease
EPX_C-crease-1
EPX_C-crease-2
Force (N)
Displacement (mm)
0
200
400
600
800
0
10
20
30
40
50

(b)

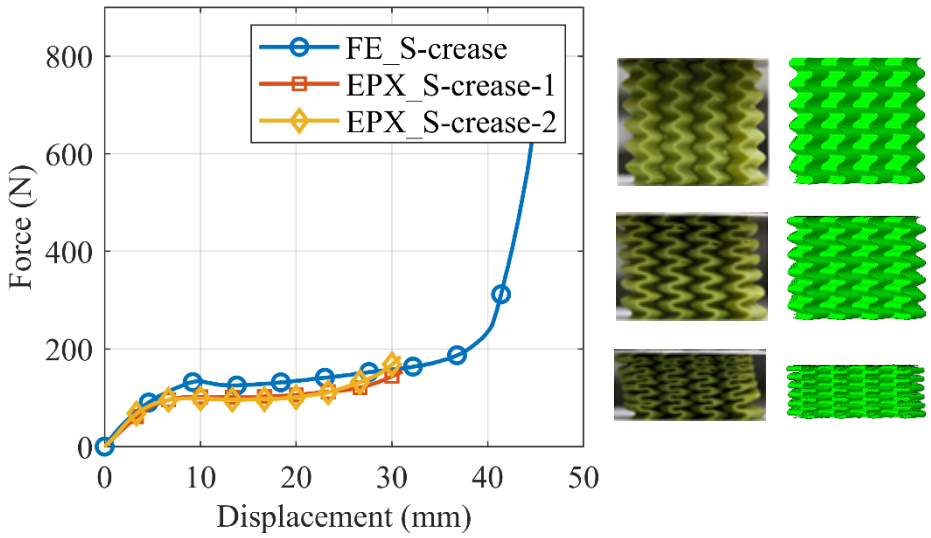
FE_S-crease
EPX_S-crease-1
EPX_S-crease-2
Force (N)
Displacement (mm)
0
200
400
600
800
0
10
20
30
40
50

(c)

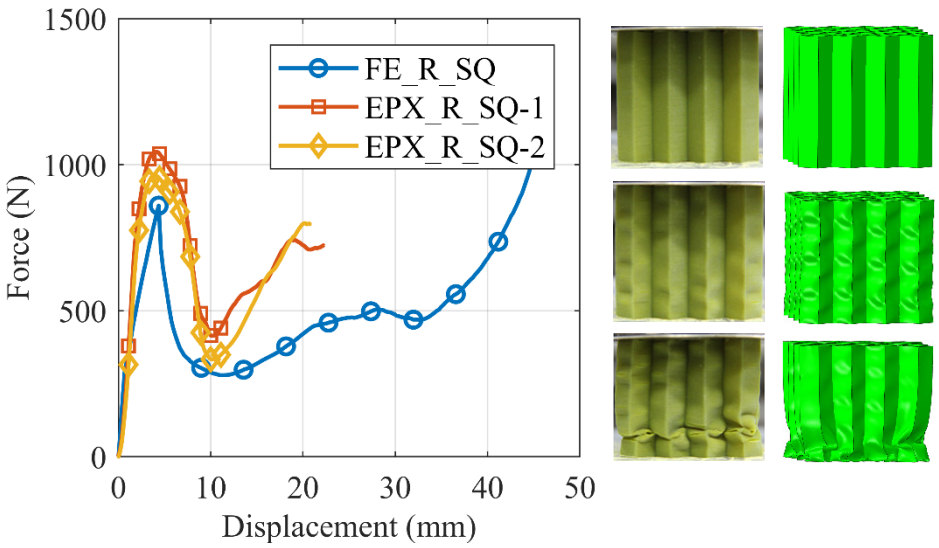

(d)

Fig. 4.13 Force-displacement curves and deformation pattern from the simulation and test: (a) Result comparison of Miura-ori core; (b) result comparison of C-crease core; (c) result comparison of S-crease core; (d) result comparison of reference square honeycomb.

The simulation shows good agreement with the test up to a large value of displacement. Hence, the FE model was validated to be effective in simulating the compression process of derivative Miura-ori-based honeycomb cores.

4.3.2 Parametric study

In the parametric study conducted in this section, same as previous Chapter, industry level Ti-Al-4V titanium alloy (TC4) was adopted as base material for all subsequent simulations. The mechanical and physical properties are: $\rho = 4400$ kg/m^3, $E = 110$ GPa, $\sigma_y = 900$ MPa, $\nu = 0.3$ and $f = 0.28$ (ASM, 2007).

In order to study the geometric effects, a total of 31 different numerical models with thickness of 0.5 mm were built with six layers and each layer contains 16 identical cells built in a four by four configuration. These models were divided into three groups. Group 1 consists 15 specimens, including five Miura-ori, five C-crease and five S-crease honeycomb cores. They

all share same values of side edge a, b and sector angle ϕ but different values of edge angle η, in order to study the effect of η when ϕ is fixed. Hence, specimens in Group 1 were studied when the relevant Miura-ori cores were deployed at different stages, as shown in Fig. 4.14 (a). Group 2 also consists 15 specimens, including three reference models in Group 1. They all share same values of side edge a, b and edge angle η but different values of sector angle ϕ, in order to study the effect of ϕ when η is fixed, as indicated in Fig. 4.14 (b). Group 3 contains three hybrid origami-honeycombs, they are designed with different stiffness gradients fulfilled by different combinations of Miura-ori-based honeycomb layers, as illustrated in Fig. 4.14 (c). The specimen MMCCSS was built with two layers of Miura-ori cells, two layers of C-crease cells and two layers of S-crease cells from bottom to top. Thus, its stiffness gradient is built in the manner of strong-to-weak from bottom to top. Accordingly, specimen SCMMCS was built in a weak-strong-weak manner and specimen MCSSCM was built in a strong-weak-strong manner. The geometric dimensions of Miura-ori, C-crease and S-crease cells adopted in the hybrid origami-honeycombs are the same of relevant reference models.

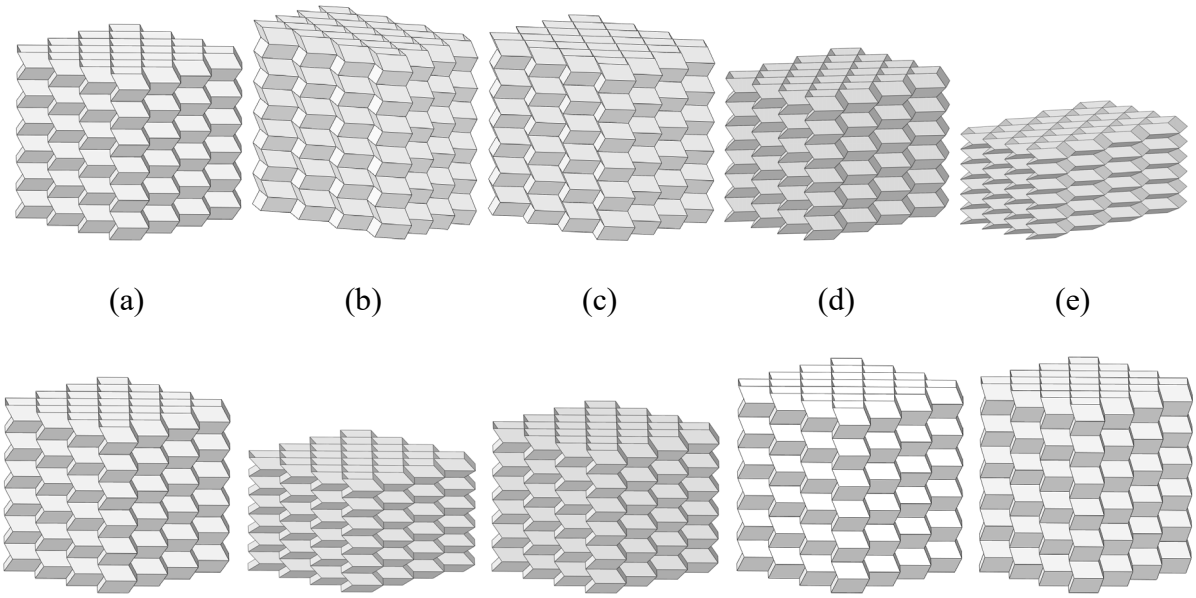

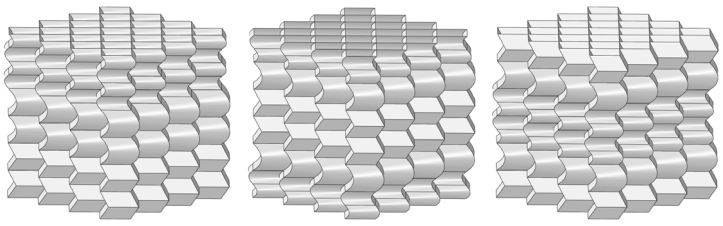

(k) (l) (m)

Fig. 4.14 Indication of numerical models in Group 1, 2 and 3: (a) M_core-Ref; (b) M_core-C1-2; (c) M_core-C1-3; (d) M_core-C1-4; (e) M_core-C1-5; (f) M_core-Ref; (g) M_core-C2-2; (h) M_core-C2-3; (i) M_core-C2-4; (j) M_core-C2-5; (k) MMCCSS; (l) SCMMCS; (m) MCSSCM.

Dimensions of all numerical models are listed in Table 4.2. Note that the Miura-ori, C-crease and S-crease cells adopted for hybrid origami-honeycombs in Group 3 are built with same configurations of the reference models, respectively. In addition, as each type of the specimens in Group 1 were initially created by a same Miura-ori pattern but deployed into different stages, the mass of all Miura-ori cores were the same. Hence, in order to keep the mass of C-crease core and S-crease cores in Group 1 unchanged, the lengths of the C-creases and S-creases of all C-crease and S-crease cores in Group 1 were designed to be the same of the reference model. Therefore, to determine the C-crease and S-crease cores in Group 1, the value of φ was defined to be φ_{min} for the reference models, and software PTC CREO was used to generate the rest c-shaped and s-shaped creases that fixed with the same length automatically. Detailed parameters to determine the C-creases and S-creases are listed in Table 4.3.

Table 4.2: Dimensions of specimens.

Group 1 (C1)	ϕ	ζ	η	a (mm)	b (mm)	mass (g)	height (mm)
M_core-Ref	63.00°	100.00°	90.00°	6.00	10.00	90.30	55.20
M_core-C1-2	63.00°	116.80°	120.00°	6.00	10.00	90.30	61.20
M_core-C1-3	63.00°	110.20°	105.00°	6.00	10.00	90.30	59.04
M_core-C1-4	63.00°	83.60°	75.00°	6.00	10.00	90.30	48.00
M_core-C1-5	63.00°	49.50°	60.00°	6.00	10.00	90.30	30.00

C_core-Ref	63.00°	100.00°	90.00°	6.00	10.00	93.20	55.20
C_core-C1-2	63.00°	116.80°	120.00°	6.00	10.00	93.20	61.20
C_core-C1-3	63.00°	110.20°	105.00°	6.00	10.00	93.20	59.04
C_core-C1-4	63.00°	83.60°	75.00°	6.00	10.00	93.20	48.00
C_core-C1-5	63.00°	49.50°	60.00°	6.00	10.00	93.20	30.00
S_core-Ref	63.00°	100.00°	90.00°	3.00	10.00	93.20	55.20
S_core-C1-2	63.00°	116.80°	120.00°	3.00	10.00	93.20	61.20
S_core-C1-3	63.00°	110.20°	105.00°	3.00	10.00	93.20	59.04
S_core-C1-4	63.00°	83.60°	75.00°	3.00	10.00	93.20	48.00
S_core-C1-5	63.00°	49.50°	60.00°	3.00	10.00	93.20	30.00

Group 2 (C2)	ϕ	ζ	η	a (mm)	b (mm)	Mass (g)	Height (mm)
M_core-Ref	63.00°	100.00°	90.00°	6.00	10.00	90.30	55.20
M_core-C2-2	53.00°	63.30°	90.00°	6.00	10.00	81.00	37.80
M_core-C2-3	58.00°	82.90°	90.00°	6.00	10.00	86.00	47.70
M_core-C2-4	68.00°	116.00°	90.00°	6.00	10.00	94.00	61.80
M_core-C2-5	73.00°	131.20°	90.00°	6.00	10.00	97.00	65.58
C_core-Ref	63.00°	100.00°	90.00°	6.00	10.00	93.20	55.20
C_core-C2-2	53.00°	63.30°	90.00°	6.00	10.00	84.80	37.80
C_core-C2-3	58.00°	82.90°	90.00°	6.00	10.00	89.60	47.70
C_core-C2-4	68.00°	116.00°	90.00°	6.00	10.00	96.10	61.80
C_core-C2-5	73.00°	131.20°	90.00°	6.00	10.00	98.30	65.58
S_core-Ref	63.00°	100.00°	90.00°	3.00	10.00	93.20	55.20
S_core-C2-2	53.00°	63.30°	90.00°	3.00	10.00	84.80	37.80
S_core-C2-3	58.00°	82.90°	90.00°	3.00	10.00	89.60	47.70
S_core-C2-4	68.00°	116.00°	90.00°	3.00	10.00	96.10	61.80
S_core-C2-5	73.00°	131.20°	90.00°	3.00	10.00	98.30	65.58

Group 3 (C3)	ϕ	ζ	η	a (mm)	b (mm)	Mass (g)	Height (mm)
MMCCSS	63.00°	100.00°	90.00°	6&3	10.00	92.23	55.20
SCMMCS	63.00°	100.00°	90.00°	6&3	10.00	92.23	55.20
MCSSCM	63.00°	100.00°	90.00°	6&3	10.00	92.23	55.20

Table 4.3: Parameters used to determine C-crease and S-crease.

Group_1 (C1)	g (mm)	e (mm)	c (mm)	d (mm)	φ_{min}	$t_{\lim}$	length (mm)
C_core-Ref	-83.3717	4.5963	87.2285	15.6302	59.7832°	17.1014°	12.5270
S_core-Ref	-41.6859	2.2982	43.6143	7.8151	59.7832°	17.1014°	12.5270
Group_2 (C2)	g (mm)	e (mm)	c (mm)	d (mm)	φ_{min}	$t_{\lim}$	length (mm)
C_core-C2-2	-69.5467	3.1484	74.6543	8.6606	73.4435°	21.3170°	12.5495
C_core-C2-3	-81.2077	3.9718	85.7049	12.4244	66.7474°	18.6433°	12.5798
C_core-C2-4	-76.5809	5.0883	79.7604	18.2030	51.9073°	16.2322°	12.4195
C_core-C2-5	-61.1116	5.4641	63.5903	19.7637	42.7885°	16.0498°	12.2885
S_core-C2-2	-34.7734	1.5742	37.3272	4.3303	73.4435°	21.3170°	12.5495
S_core-C2-3	-40.6039	1.9859	42.8525	6.2122	66.7474°	18.6433°	12.5798
S_core-C2-4	-38.2905	2.5442	39.8802	9.1015	51.9073°	16.2322°	12.4195
S_core-C2-5	-30.5558	2.7321	31.7952	9.8819	42.7885°	16.0498°	12.2885

4.3.3 FEA results

FEA results obtained from the simulations are illustrated in Fig. 4.15. Results of SEA, peak load (P_{max}) and mean crushing force (P_m) are summarized in Table 4.4.

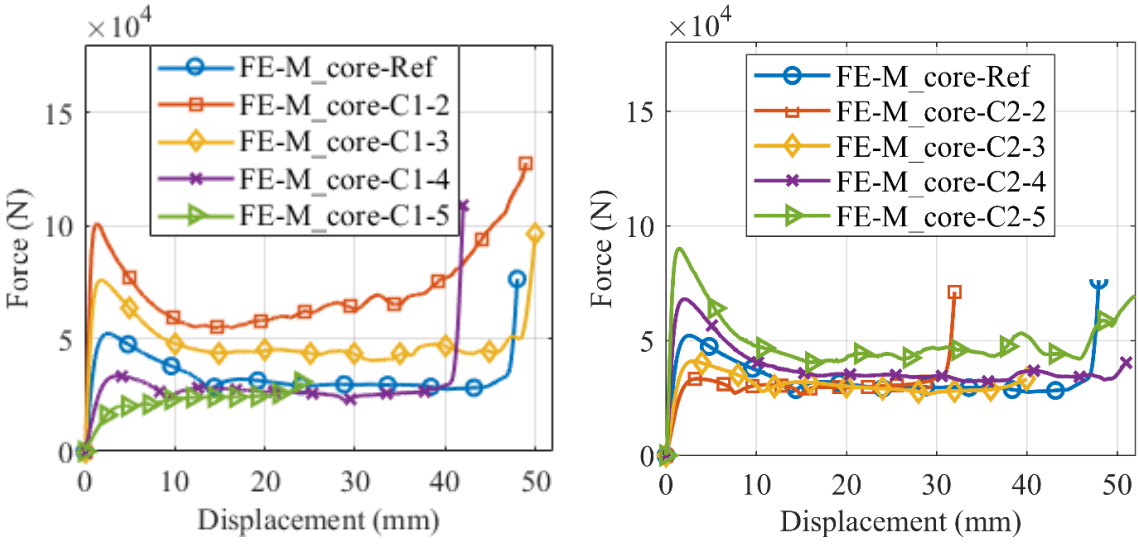

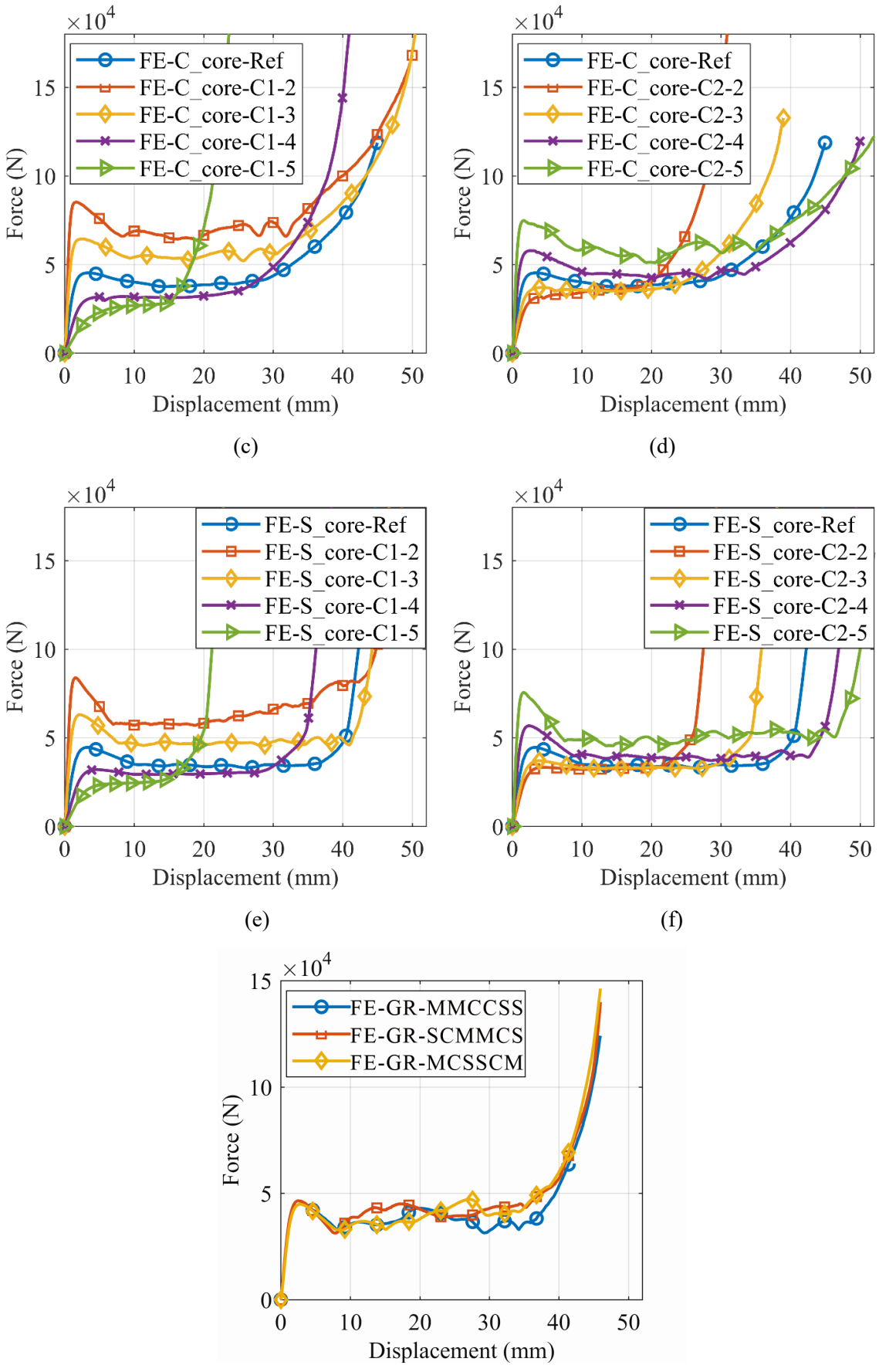

Fig. 4.15 Force-displacement curves: (a) Results of Miura-ori cores in Group 1; (b) results of Miura-ori cores in Goup 2; (c) results of C-crease cores in Group 1; (d) results of C-crease

cores in Group 2; (e) results of S-crease cores in Group 1; (f) results of S-crease cores in Group 2; (g) results of hybrid origami-honeycomb in Group 3.

It can be found from Fig. 4.15 (a), (c) and (e) that when the Miura-ori, C-crease and S-crease cores are deployed at different stages, their force-displacement responses differs notably. The peak force of all three types of cores decreases when the value of angle η decreases and the plateau force also reduces at the same time. When the value of η is larger, as the structure is at a less-deployed stage, the peak force of all three types of structures are relatively higher than the plateau and followed by a steep reduction. On the other hand, while the value of angle η is smaller, the value of peak load is relatively appealing to the plateau, which is desirable for ideal energy absorbing structure. From Table 4.4 it can be noted that the SEA of specimens in Group 1 reached the highest when the angel η is 105^o or 120^o, but the P_{max} is also the highest at the same time.

Table 4.4: FEA results.

Group 1 (C1)	P_{max} (kN)	P_m (kN)	SEA (kJ/kg)	Densification Strain
M_core-Ref	52.16	32.62	16.17	0.81
M_core-C1-2	100.93	65.30	29.24	0.66
M_core-C1-3	75.83	47.34	23.99	0.77
M_core-C1-4	33.46	26.51	11.96	0.85
M_core-C1-5	25.18	20.83	4.87	0.70
C_core-Ref	45.28	39.43	12.66	0.54
C_core-C1-2	85.20	69.66	24.29	0.52
C_core-C1-3	64.39	55.68	18.42	0.52
C_core-C1-4	35.46	30.34	8.17	0.53
C_core-C1-5	28.46	22.18	3.51	0.50
S_core-Ref	44.55	35.29	14.48	0.69
S_core-C1-2	83.85	65.26	30.53	0.70
S_core-C1-3	63.05	48.35	21.56	0.70
S_core-C1-4	31.96	28.80	8.48	0.58
S_core-C1-5	25.87	21.89	3.30	0.47

Group 2 (C2)	P_{max} (kN)	P_m (kN)	SEA (kJ/kg)	Densification Strain
M_core-Ref	52.16	32.62	16.17	0.81
M_core-C2-2	35.39	29.79	11.36	0.82
M_core-C2-3	41.01	30.69	13.49	0.79
M_core-C2-4	68.08	38.40	20.11	0.80
M_core-C2-5	90.07	48.87	23.20	0.70
C_core-Ref	45.28	39.43	12.66	0.54
C_core-C2-2	38.54	32.26	7.43	0.52
C_core-C2-3	41.58	34.71	9.82	0.53
C_core-C2-4	57.82	46.09	16.13	0.54
C_core-C2-5	74.81	59.77	21.26	0.53
S_core-Ref	44.55	35.29	14.48	0.69
S_core-C2-2	33.22	30.65	7.55	0.55
S_core-C2-3	37.01	32.74	10.94	0.63
S_core-C2-4	56.87	40.70	18.11	0.69
S_core-C2-5	75.61	51.74	24.52	0.71
Group 3 (C3)	P_{max} (kN)	P_m (kN)	SEA (kJ/kg)	Densification Strain
MMCCSS	44.92	37.11	14.53	0.65
SCMMCS	46.50	40.37	15.50	0.64
MCSSCM	47.20	38.55	14.42	0.63

The force-displacement curve of specimens in Group 2 are shown in Fig. 4.15 (b), (d) and (f). It can be found that when the value of angle ϕ increases, the peak force increases at the same time, as well as the plateau force. It can be also noted from Table 4.4 that when the angle ϕ reached the larges value, the relative SEA became also the largest, as well as the value of P_{max}.

The results of hybrid origami-honeycombs in Fig. 4.15 (g) shows that the force-displacement relation is quite ideal in terms of energy absorption, as the value of peak force is relatively constant to the plateau force. The SEA of all three hybrid origami-honeycombs also showed better results comparing to C_core-Ref and S_core-Ref, as shown in Table 4.4. Even though

the SEA of the hybrid origami-honeycombs is less than the M_core-Ref, they do not possess extrusive peak force in the force-displacement relation. Based on the above result, it is indicated that the hybrid origami-honeycomb with stiffness gradient will outperform individual reference cores as more ideal energy absorbing structure/material.

4.3.4 Discussion

4.3.4.1 Side angle

As illustrated in Table 4.4 and Fig. 4.16, the value of P_{max}, P_m and SEA increases with the increase of η when ϕ is constrained. It is commonly known that reducing P_{max} and increasing P_m at the same time tends to be contradictory, but the derivative cores managed to decrease the peak force by a relative large scale and was able to maintain a relatively high SEA at the same time. This indicates that in actual engineering application, when the force transmission during the crush event is vital and need to be minimized, origami-honeycomb cores built with smaller η values should be adopted. On the other hand, when energy absorption capacity is priority, origami-honeycomb cores constructed with larger η values should be used.

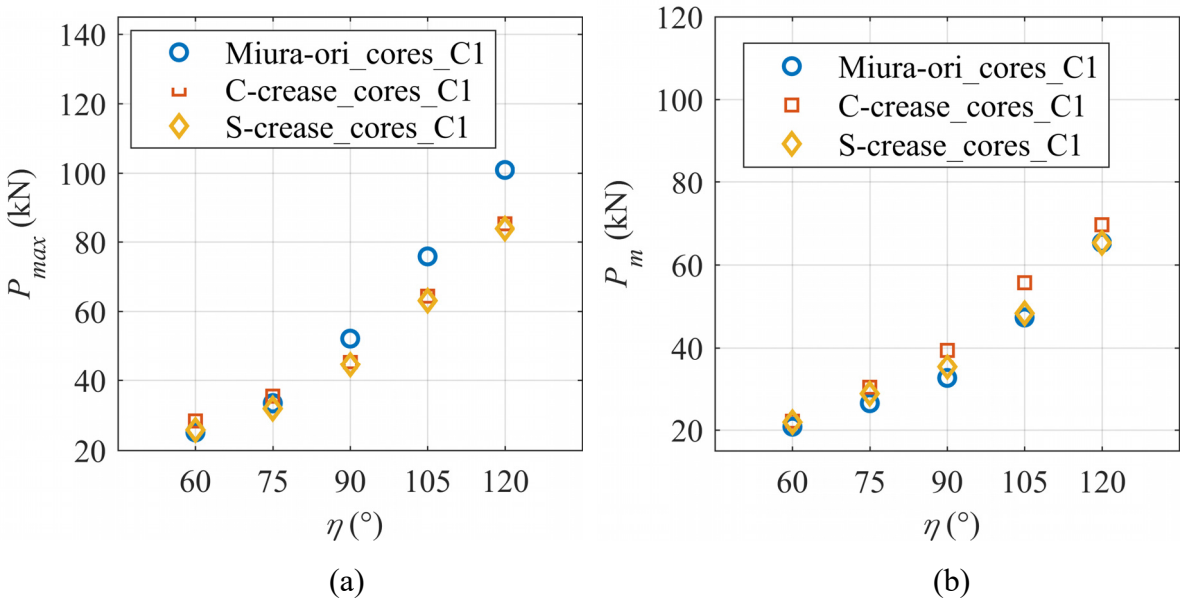

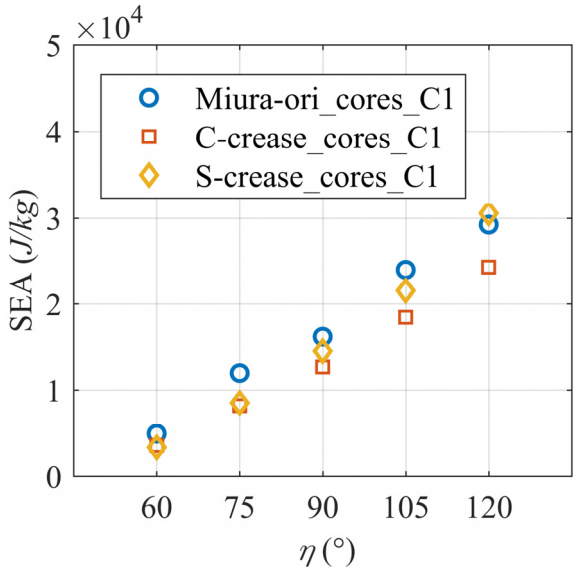

(c)

Fig. 4.16 Effect of side angle η: (a) SEA vs η; (b) P_{max} vs η; (c) P_m vs η.

4.3.4.2 Sector angle

As illustrated in Table 4.4 and Fig. 4.17, the P_{max}, P_m and SEA increases with the increase of ϕ when η is constrained. It is obvious that when the values of side edge a, b and edge angle η are fixed, the smaller the sector angle ϕ is, the 'more-deployed' the core will be (as illustrated in Fig. 4.14). Therefore, when load is applied to the core at the more-deployed stage, the structure deforms steadily by following the designed pattern and plastic deformation tends to occur in less regions only along the pattern, resulting in the reduction of P_{max}, P_m and SEA. Hence, appropriate adjustments and selections need to be made according to actual situation and the feasibility of manufacturing process.

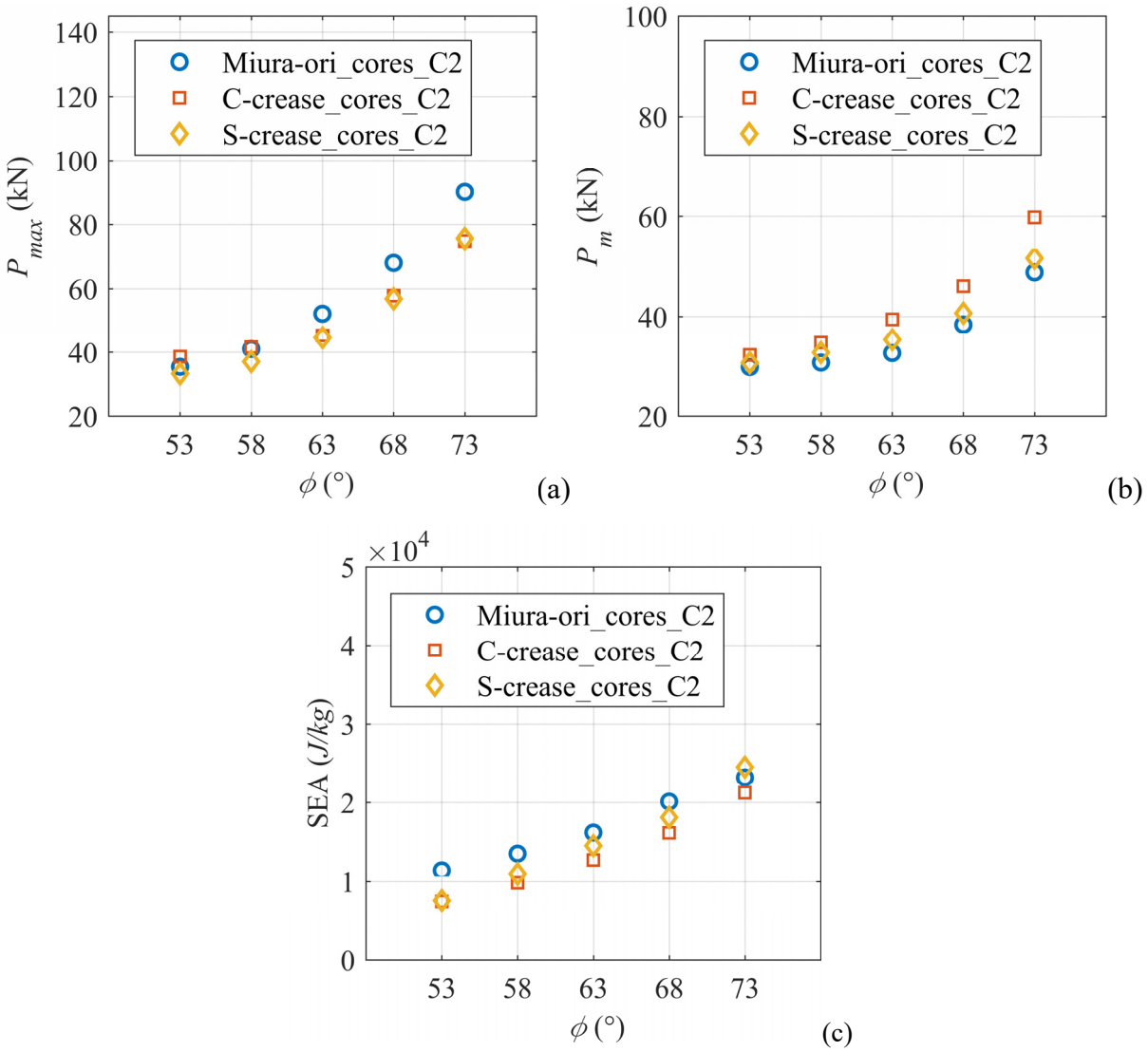

Fig. 4.17 Effect of sector angle ϕ: (a) P_{max} vs ϕ, (b) P_m vs ϕ, (c) SEA vs ϕ.

4.3.4.3 Hybridization

It can be noted from Fig. 4.18 that the reference Miura-ori core has the largest SEA and densification strain among other cores and hybrid origami-honeycombs, however the value of P_{max} is also the largest. On the other hand, all three hybrid origami-honeycombs are better at SEA than the C-crease and S-crease cores. Especially in the case of SCMMCS, the SEA is notably larger than the other ones and relatively close to the Miura-ori core, however its peak load P_{max} is significantly smaller than the Miura-ori core. Because the specimen SCMMCS was built in a weak-strong-weak manner, theoretically, when the structure is subjected to static axial compression, the bottom and upper weaker layers will be crushed and semi-densified prior to

the middle stronger ones. As a result, there will be a similarly semi-fixed boundary for the middle layers (as introduced in previous Chapter), which leads to a higher energy absorption capacity. This phenomenon can also be captured from the force-displacement curve in Fig. 4.15 (g), as for the result of SCMMCS, it can be seen that the force has firstly reached a peak followed by an apparent decrease, indicating the buckling of the weaker layers. Then, the force has increased notably before reaching a plateau owning to the increased plastic deformation of the stronger layers.

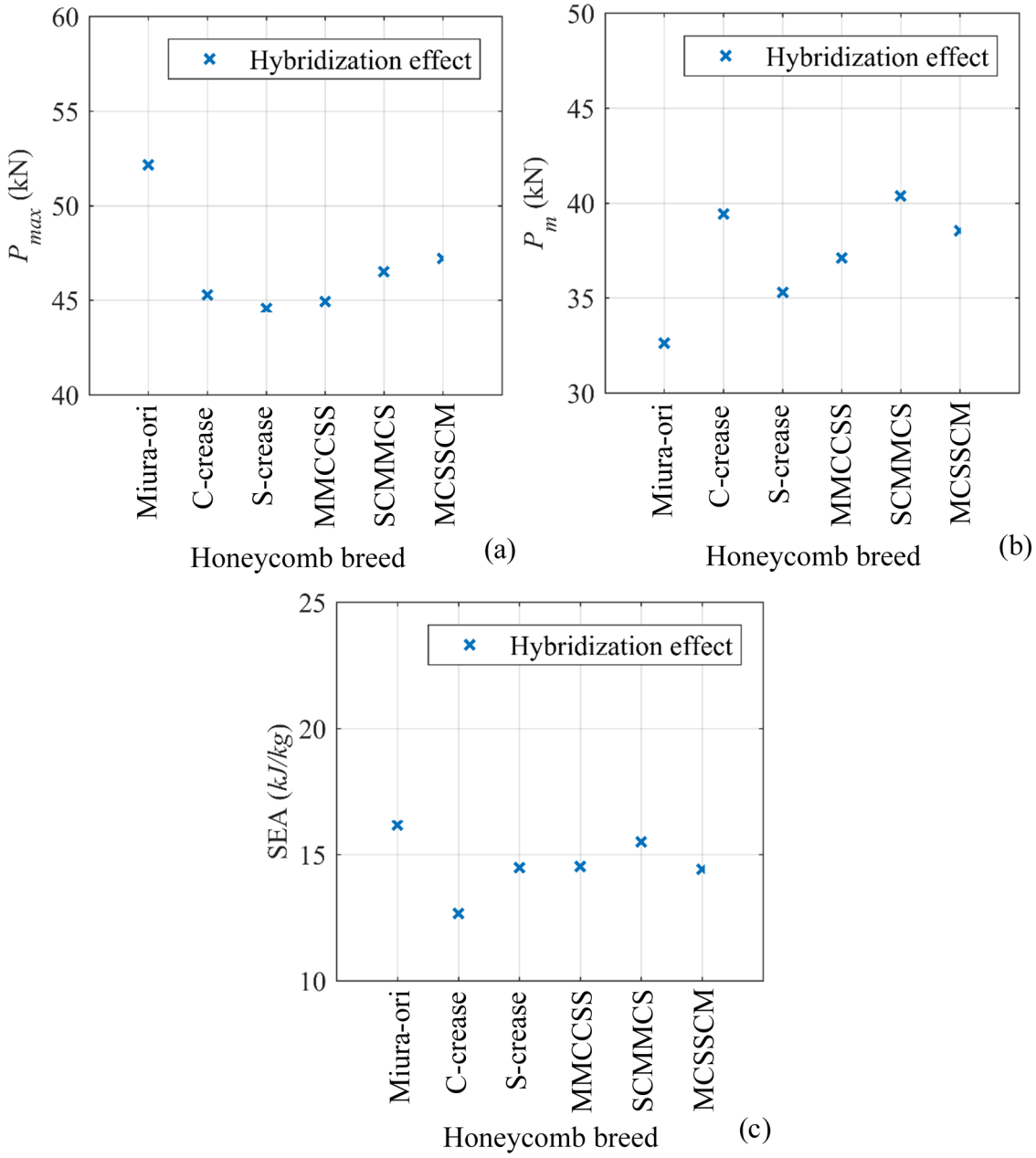

Fig. 4.18 Results of hybridization: (a) P_{max} vs honeycomb breed; (b) P_m vs honeycomb breed; (c) SEA vs honeycomb breed.

From these results, it can be noted that the hybridization has a significant influence on the peak force and SEA of derivative cores. Under static load, it can not only reduce the peak force but also increase the SEA comparing to the individual cores.

4.4 Summary

Two unique derivative Miura-ori-based honeycomb cores with hybrid honeycombs have been designed as a family of novel metamaterial in order to obtain low peak force and efficient energy absorption capacity. Experimental and numerical results are presented to study the mechanical behaviors of the honeycomb. Especially it is found that under static loading condition, the hybridization of derivative Miura-ori-based honeycomb cores can reduce the impact force and meanwhile increase the energy absorption efficiency. Effects of design parameters are summarized as follows:

1) When the values of side edge a, b and sector angle ϕ are determined, the side angle η controls deployment stage of derivative cores. The larger the value of η is, the less deployed the structure will be, as a result, the SEA and P_m will be increased correspondingly. However the relevant P_{max} will also be raised. Thus, proper design needs to be considered to meet the actual situation.
2) The sector angle ϕ plays the most important role of controlling the deformation pattern as well as SEA and P_{max}. When the values of side edge a, b and side angle η are determined, it is apparent that the greater the value of ϕ is, the higher SEA and P_{max} will be. In order to maintain reasonable high SEA and achieve relatively low P_{max}, proper design needs to be selected.
3) The hybridization can notably affect the peak force and SEA when compared to the individual core that is constructed in the same form. It seems that the hybridization built in

a weak-strong-weak manner can lead to a decrease in P_{max} and meanwhile an increase in SEA.

In conclusion, this Chapter has proposed a novel concept of hybridization of the derivative Miura-ori-based honeycomb cores that can decrease the peak load during crush and meanwhile increase the energy absorption capacity. It is shown that the concept of hybridization can be efficiently adopted to design new and ideal energy absorbing materials.

Chapter 5

Effects of dynamic loading on origami honeycombs

This chapter investigates the energy absorption capacity of Miura-ori-based honeycomb cores and hybrid honeycombs under different crushing speed. Theoretical prediction of the dynamic mean crushing stress of the origami honeycomb cores are proposed. FEM is used to study and evaluate the effects of dynamic loading on the contact force, transmitted force, and SEA of the origami honeycombs. Discussions are made to compare failure behaviors of the origami honeycombs under different dynamic loadings.

5.1 Theoretical prediction

This section proposes the theoretical prediction of the dynamic mean crushing stress of the origami honeycombs cores. By idealizing the origami honeycomb core (Miura-ori, C-crease or S-crease core) as an isotropic, one-dimensional and rigid-perfect-plastic-locking (RPPL) continuum proposed by Reid and Peng (1997), and applying the shock theory (Meyers, 1994), the dynamic crushing stress of origami honeycomb core is derived as following:

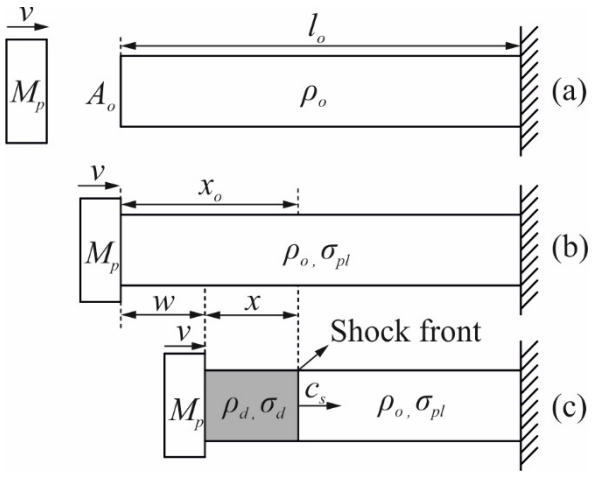

Fig. 5.1 The shock model: (a) Initial condition; (b) the initial moment of impingement; (c) shock wave propagation.

Fig. 5.1 (a) shows the idealized origami honeycomb core with the initial length of l_o, density ρ_o, area of the cross-section A_o, stroke by the rigid projectile with mass of M_p and impact velocity of v. A shock wave is assumed to be initiated and travels through the core when the impact occurs, and because of the rigid property of the initial response, the stress in all the material ahead of the shock wave is increased to σ_{pl}, as shown in Fig. 5.1 (b) and (c). σ_{pl} is the static plateau stress of the RPPL model and it equals to the static mean crushing stress σ_m. As the shock wave passes through the material, the portion behind the shock is compacted up to the densification strain ε_d with the density increased to ρ_d and the dynamic stress is raised to σ_d, as shown in Fig. 5.1 (c).

Assume at time t, as shown on Fig. 5.1 (b) and (c), the original length x_o of the crushed portion can be expressed as:

$$x_o = w + x \tag{5.1}$$

where w is the crush distance of the rigid projectile and x is the deformed length of the crushed origami honeycomb core.

By using the conservation of mass, it gives:

$$\rho_d A_o x = \rho_o A_o (w + x) \tag{5.2}$$

where ρ_d is the densification density.

Thus, it gives:

$$\frac{\rho_o}{\rho_d} = \frac{x}{w+x} = \lambda \tag{5.3}$$

Hence, the densification strain is:

$$\varepsilon_d = \frac{x_o - x}{x_o} = \frac{w}{w+x} \tag{5.4}$$

Therefore,

$$\lambda = 1 - \varepsilon_d \tag{5.5}$$

Thus,

$$x = \frac{\lambda}{1-\lambda} w = \frac{1-\varepsilon_d}{\varepsilon_d} w \tag{5.6}$$

The shock speed is defined as $c_s=dx/dt$ and the velocity of the material particles in the compressed volume is defined as $v=dw/dt$.

Thus, it gives:

$$c_s = \frac{dx}{dt} = \frac{\lambda}{1-\lambda}\frac{dw}{dt} = \frac{\lambda}{1-\lambda} v \tag{5.7}$$

The momentum at time t is the product of the mass of crushed portion of the origami honeycomb core and the velocity of the material particles in the compressed volume. Thus, by applying the conservation of momentum, it gives:

$$A_o(\sigma_d - \sigma_{pl})t = A_o \rho_d c_s t v = \frac{A_o \rho_o t c_s}{\lambda} v \tag{5.8}$$

where σ_d is the dynamic crushing stress.

Thus, the dynamic crushing stress of the origami honeycomb core is given as:

$$\sigma_d = \sigma_{pl} + \frac{\rho_o c_s}{\lambda} v = \sigma_{pl} + \frac{\rho_o}{\varepsilon_d} v^2 \tag{5.9}$$

When the crushing speed is constant, the dynamic stress obtained above equals to the dynamic mean crushing stress of the densified portion of the core ($\sigma_d = \sigma_m^d$).

5.2 Finite element model

Abaqus/explicit was employed to simulate the dynamic compression events, and to investigate the influence of dynamic loading on the derivative Miura-ori-based honeycombs. All numerical 3D models were built in PTC Creo before implanted into Abaqus for analysis.

The crushing scenario of derivative Miura-ori-based honeycombs was modelled by placing the numerical sample between two rigid panels with the bottom plate fixed completely, whereas all degrees of freedom of the moving upper plate were constrained except for the uniaxial loading direction, as indicated in Fig. 5.2. All samples were modelled with the material of Ti-Al-4V titanium alloy (TC4) and its properties are: $\rho = 4400$ kg/m^3, $E = 110$ GPa, $\sigma_y = 900$ MPa, $\nu = 0.3$ and $f = 0.28$ (ASM, 2007). Four-node shell elements with reduced integration S4R was employed for meshing. Self-contact was defined, which took into account hard contact and friction between panels and honeycomb samples. A small gap of 0.1mm was left between the upper plate and the specimen to avoid initial penetration. Constant velocity of 4.6m/s, 23m/s and 46m/s was assigned to the upper plate respectively to simulate the dynamic crushing process and the crushing distance was set to be 46mm (around 83% of the specimen height).

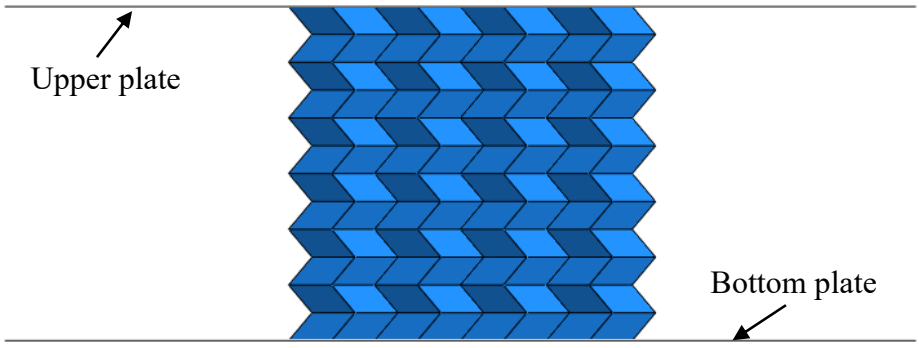

Fig. 5.2 Dynamic model.

Two groups of derivative tetragonal honeycombs were investigated when subjected to dynamic compression with different constant crushing speed. Group 1 comprises three derivative cores of Miura-ori, C-crease and S-crease honeycomb cores in order to study the mechanical

characteristics and energy absorption capacity of the cores under different dynamic loading speed. These three core models are the same reference models as introduced in Chapter 4 (M_core-Ref, C_core-Ref and S_core-Ref) and they are illustrated in Fig. 5.3.

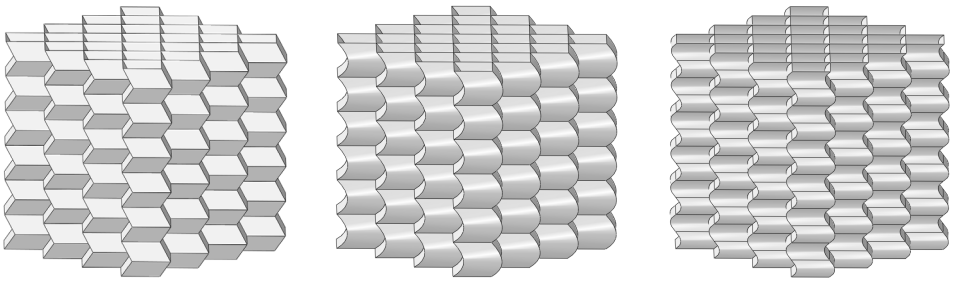

(a) (b) (c)

Fig. 5.3 Derivative cores of Group 1: (a) Miura-ori core; (b) C-crease core; (c) S-crease core.

Group 2 contains three hybrid honeycombs in order to study the influences of different stiffness gradients under different dynamic loading speed, as shown in Fig. 5.4. These three hybrid models are also the same ones that have been studied in Chapter 4 (MMCCSS, SCMMCS, and MCSSCM). In addition, there is a reversed model of MMCCSS in Group 2 labelled as SSCCMM. The specimen MMCCSS is built with a stiffness gradient of strong to weak manner, the weaker layers (S-crease layers) are placed to face the impingement at the front while the stronger layers are at the distal end. Hereby, the specimen SSCCMM is a reversed version of MMCCSS that the stronger layers (Miura-ori layers) are placed in the front to face the impingement at the very beginning. The other two hybrid honeycombs SCMMCS and MCSSCM are built in manners of weak-strong-weak and strong-weak-strong, respectively. Dimensions of all numerical models are listed in Table 5.1.

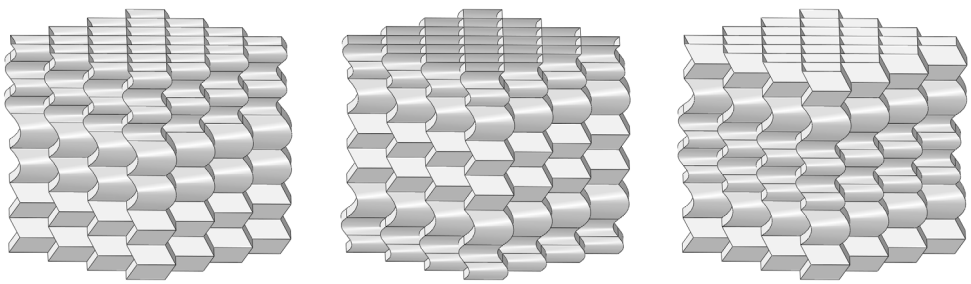

(a) (b) (c)

Fig. 5.4 Hybrid models in Group 2: (a) MMCCSS; (b) SCMMCS; (c) MCSSCM.

Table 5.1: Dimensions of specimens.

Group_1	ϕ	ζ	η	a (mm)	b (mm)	Mass (g)	Height (mm)
Miura-ori core	63.00°	100.00°	90.00°	6.00	10.00	90.30	55.20
C-crease core	63.00°	100.00°	90.00°	6.00	10.00	93.20	55.20
S-crease core	63.00°	100.00°	90.00°	3.00	10.00	93.20	55.20
Group_2	ϕ	ζ	η	a (mm)	b (mm)	Mass (g)	Height (mm)
MMCCSS	63.00°	100.00°	90.00°	3&6	10.00	92.23	55.20
SSCCMM	63.00°	100.00°	90.00°	3&6	10.00	92.23	55.20
SCMMCS	63.00°	100.00°	90.00°	3&6	10.00	92.23	55.20
MCSSCM	63.00°	100.00°	90.00°	3&6	10.00	92.23	55.20

5.3 FE analyses and results

5.3.1 Derivative cores

The FEA results of derivative Mira-ori-based honeycomb cores under dynamic loading are summarized in this section. In order to analyse and evaluate the dynamic results, predictions based on the FEA results of derivative cores under quasi-static compression were primarily conducted and summarized in sub-section 5.3.1.1.

5.3.1.1 Theoretical predictions of derivative cores

By idealizing the derivative cores as homogenous continuums, the relevant elastic wave speed c_{el} and the yield velocity v_y can be calculated using (Meyers, 1994)

$$c_{el} = \sqrt{E / \rho_o}\,, \tag{5.10}$$

and

$$v_y = \sigma_{pl} / c_{el}\rho_o\,. \tag{5.11}$$

Based on the results in Chapter 4, the static engineering stress-strain curves of Miura-ori, C-crease and S-crease cores can be obtained, and they are shown in Fig. 5.5.

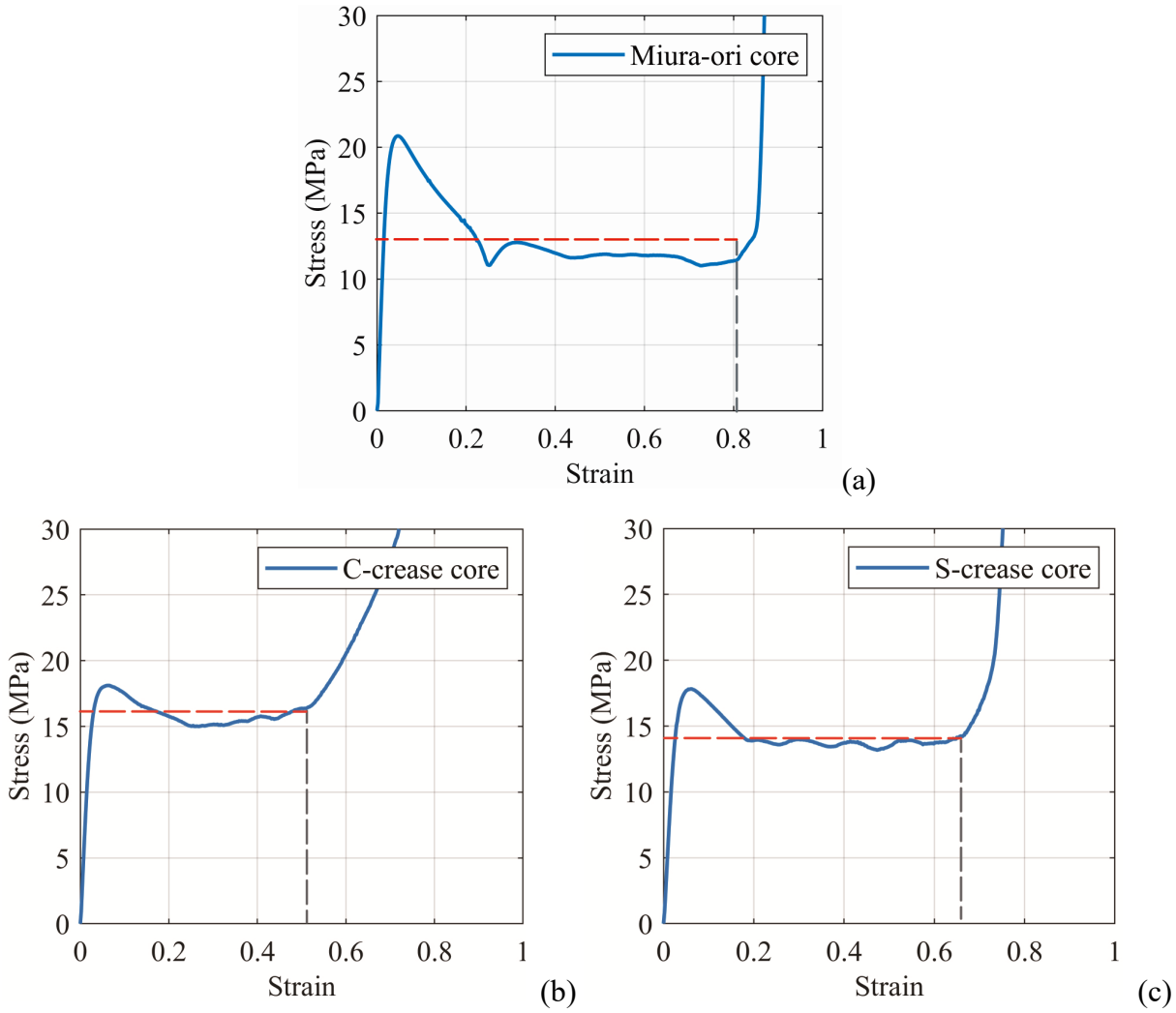

Fig. 5.5 Static stress-strain curves: (b) Miura-ori core; (b) C-crease core; (c) S-crease core.

The static plateau stress σ_{pl} (mean crushing stress) of the origami honeycomb core can be calculated by the definite integral equation (5.12),

$$\sigma_{pl} = \frac{\int_0^{x_0} \sigma(x)dx}{\varepsilon_d} \tag{5.12}$$

where ε_d is the densification strain and $x_0 = \varepsilon_d$.

Hence, the relevant mechanical properties of derivative cores can be obtained according to Eqs. (5.10) ─ (5.12) and Figs. 5.5. The results are summarized in Table 5.2.

Table 5.2: Mechanical properties of derivative Mira-ori-based cores.

	E (Mpa)	ρ_o (kg/m3)	c_{el} (m/s)	σ_{pl} (MPa)	v_y (m/s)
Miura-ori core	832	654	1128	13.05	17.7
C-crease core	678	675	1002	15.77	23.31
S-crease core	544	675	898	14.12	23.29

5.3.1.2 Miura-ori core

The FEA results of Miura-ori core are listed in Table 5.3 ($P_{max\text{-}imp}$ is the peak contact force at the impinged end of the specimen, $P_{max\text{-}dis}$ is the peak reaction force at the distal end of the specimen.). The force-displacement cures and deformation patterns of Miura-ori core under quasi-static and dynamic loadings are plotted in Fig. 5.6. It can be observed that when the compressive loading velocity is 4.6 m/s, the failure mode remains identical to the quasi-static condition. Under this condition, dynamic effects are negligible and the contact force at the loaded region is constant with the distal reaction force.

Table 5. 3: FEA results of Miura-ori core.

	$P_{max\text{-}imp}$ (kN)	P_m (kN)	$P_{max\text{-}dis}$ (kN)	SEA (kJ/kg)	Densification Strain
Miura-ori_QS	52.16	32.62	52.16	16.17	0.81
Miura-ori_4.6m/s	52.02	31.47	52.08	16.39	0.85
Miura-ori_23m/s	75.87	32.02	68.10	16.72	0.85
Miura-ori_46m/s	186.90	36.16	70.55	18.49	0.84

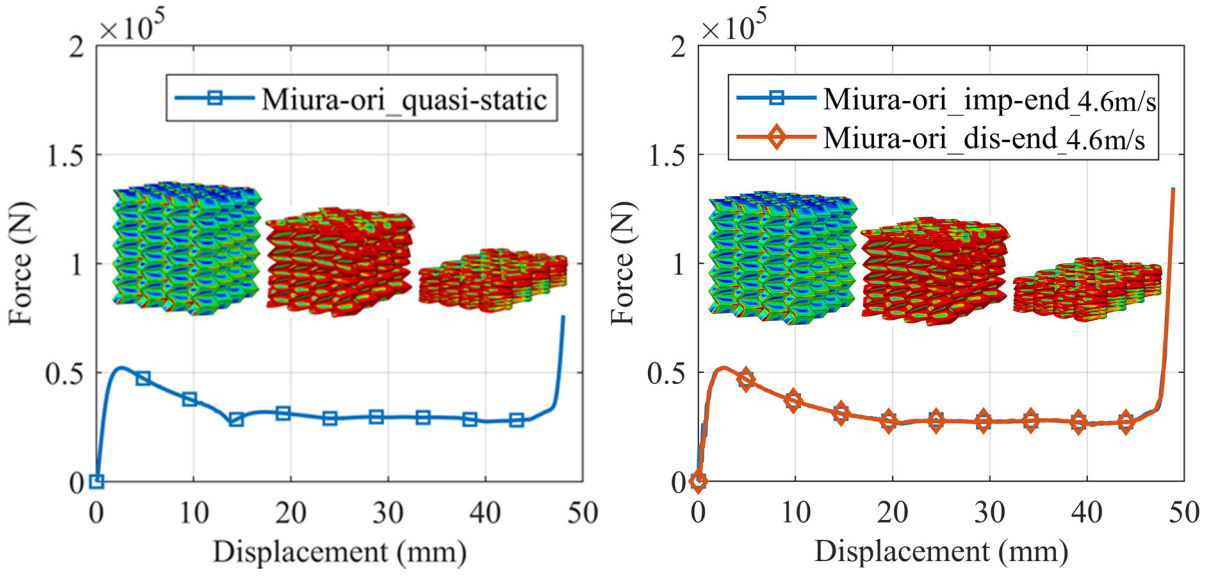

(a) (b)

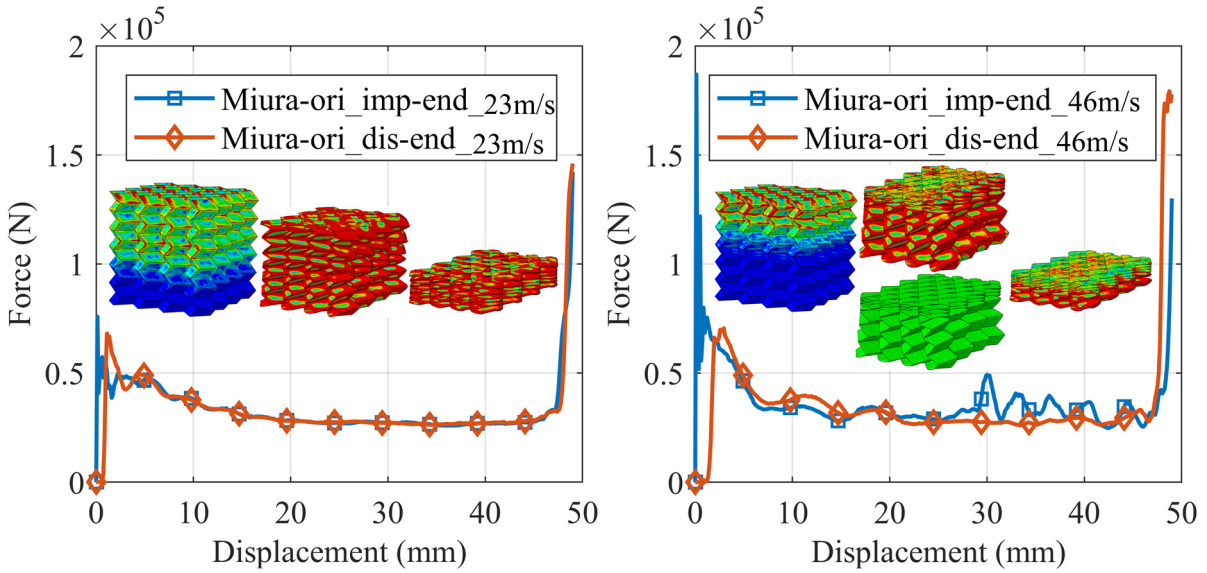

Fig. 5.6 Numerical results of Miura-ori core: (a) Results under quasi-static loading condition. Results under dynamic loading condition with the loading velocity of (b) 4.6m/s, (c) 23m/s and (d) 46m/s.

It can be observed from Fig. 5.6 (c) that when the impact velocity is increased to 23 m/s, at the very beginning of the collision, the contact force at the impinged end increases notably all of a sudden. While the compressive elastic stress wave is still travelling through the structure at this very moment, the reaction force at the distal end remains zero. As the dynamic loading velocity exceeds the approximate theoretical yield velocity of 17 m/s, the plastic wave shall be generated. However, there are no obvious signs of local plastic deformation at the loaded end of the core. When the compressive elastic wave reaches the distal surface where no displacement is allowed, the reflected wave is also compressive, resulting in the magnitude of the compressive force being doubled. As a result, the distal layer of the core collapses simultaneously with a notable high peak reaction force depicted in the force-displacement curve. As the stress waves die out within a brief time period and the loading speed is relatively low, the inertia and strain rate effect are also minor. It can be seen that shortly after the collision, the contact and reaction force remains stable and constant, and there is no obvious change in deformation mode when compared to the static loading condition.

When the Miura-ori core is subjected to the impact with the velocity of 46m/s, an obvious shock front is formed at the impinged end. As shown in Fig. 5.6 (d), the core is separated by the shock front into two portions: the condensed portion at the impinged end and the uncondensed portion at the distal end. It can be also seen from the force-displacement curve in Fig. 5.6 (d) that a significant sudden increase of contact force at the impinged end appeared at the beginning of the impact, followed by notable fluctuations. The peak of the contact force is also around three times higher than the distal reaction force.

5.3.1.3 C-crease core

The FEA results of C-crease core are listed in Table 5.4. The force-displacement cures and deformation patterns of C-crease core under quasi-static and dynamic loadings are plotted in Fig. 5.7. It can be observed that when the compressive loading velocity is 4.6 m/s, the failure mode remains identical to the quasi-static condition. Under this condition, dynamic effects are negligible and the contact force at the loaded region is constant with the distal reaction force.

Table 5.4: FEA results of C-crease core.

	$P_{max\text{-}imp}$ (kN)	P_m (kN)	$P_{max\text{-}dis}$ (kN)	SEA (kJ/kg)	Densification Strain
C-crease_QS	45.28	39.43	45.28	12.66	0.54
C-crease_4.6m/s	45.23	39.13	45.19	12.55	0.54
C-crease_23m/s	53.02	39.67	51.53	13.41	0.57
C-crease_46m/s	65.92	43.20	59.10	16.42	0.64

When the impact velocity is increased to 23 m/s, at the very beginning of the collision, the contact force at the impinged end increases notably while the reaction force at the distal end remains zero. The peak force at the impinged end is only slightly higher than the distal end and it has increased 17.5% when compared to static loading condition. Meanwhile the mean crushing force has no significant changes, as well as the SEA and failure mode.

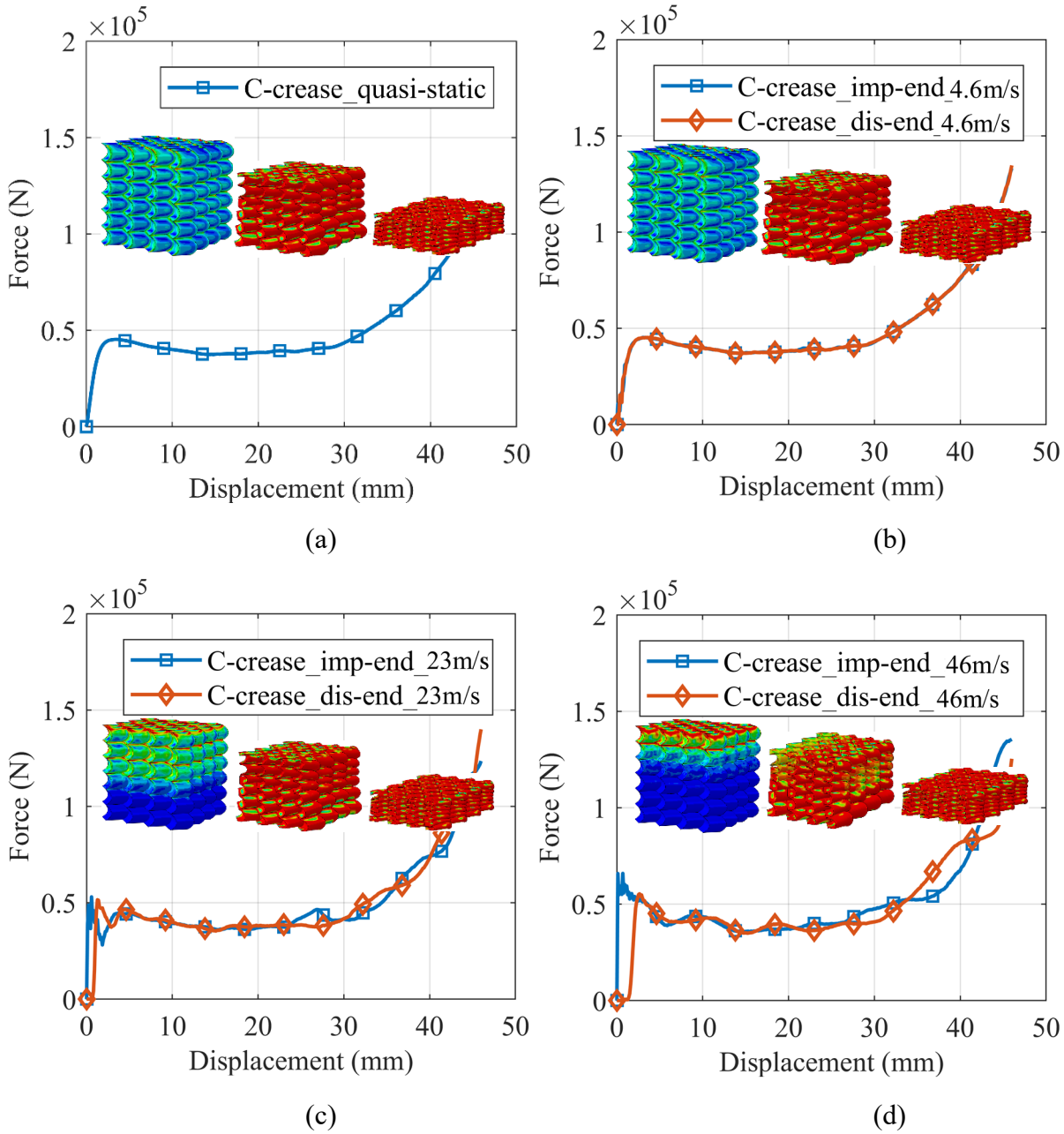

Fig. 5.7 Numerical results of C-crease core: (a) Results under quasi-static loading condition. Results under dynamic loading condition with the loading velocity of (b) 4.6m/s, (c) 23m/s and (d) 46m/s.

When the C-crease core is subjected to the impact with the velocity of 46 m/s, a notable sudden increase of contact force at the impinged end appeared at the beginning of the impact, followed by some fluctuations. The peak of the contact force has been increased over 45% and the peak of the distal reaction force has been increased over 30% when compared to the static loading

condition. The mean crushing force has also been increased about 9.6% but the failure mode has not been notably influenced.

5.3.1.4 S-crease core

The FEA results of S-crease core are listed in Table 5.5. The force-displacement cures and deformation patterns are plotted in Fig. 5.8. When the compressive loading velocity is 4.6 m/s, the failure mode remains identical to the quasi-static condition. Under this condition, dynamic effects are negligible and the contact force at the loaded region is constant with the distal reaction force.

Table 5.5: FEA results of S-crease core.

	$P_{max\text{-}imp}$ (kN)	P_m (kN)	$P_{max\text{-}dis}$ (kN)	SEA (kJ/kg)	Densification Strain
S-crease_QS	44.55	35.29	44.55	14.48	0.69
S-crease_4.6m/s	44.86	35.58	44.77	14.27	0.68
S-crease_23m/s	48.16	36.21	53.41	15.24	0.71
S-crease_46m/s	65.77	38.38	69.17	16.95	0.75

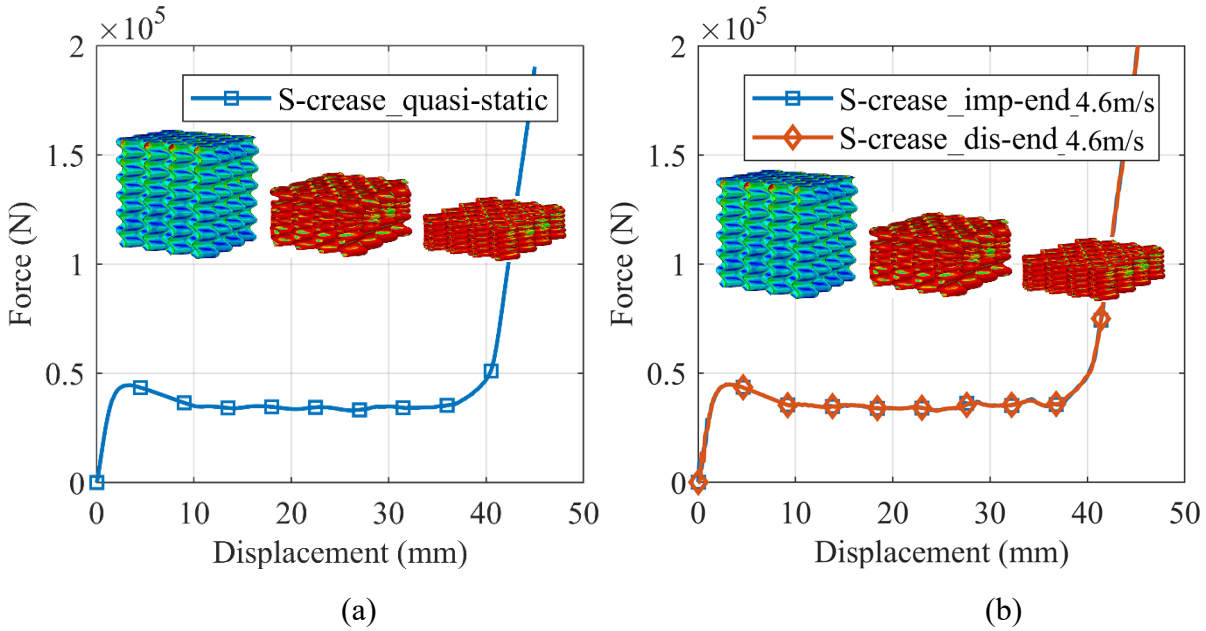

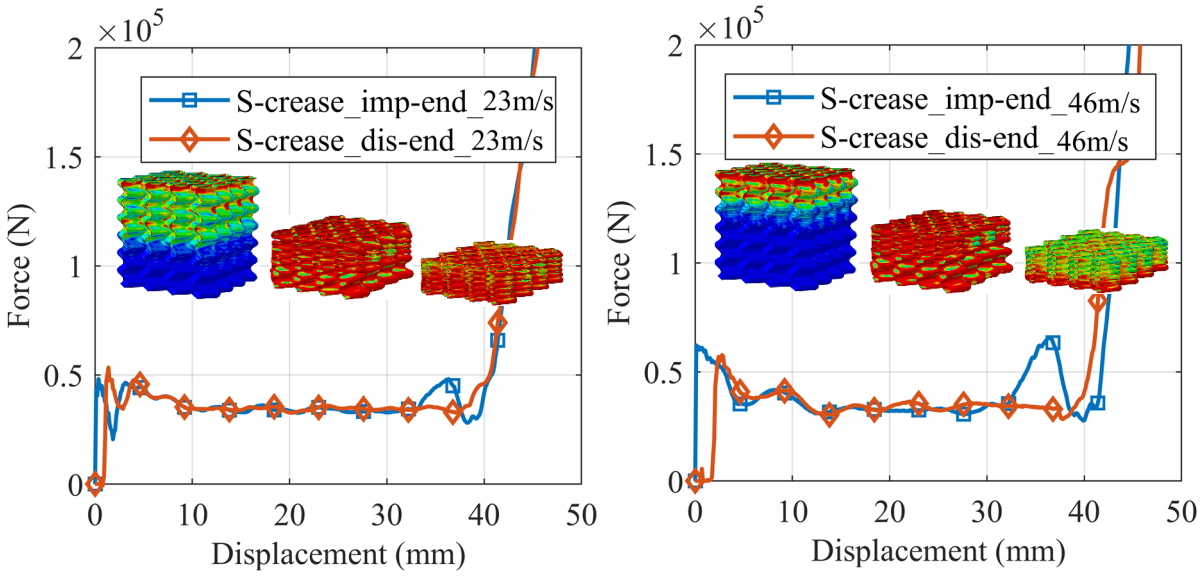

Fig. 5.8 Numerical results of S-crease core: (a) Results under quasi-static loading condition. Results under dynamic loading condition with the loading velocity of (b) 4.6m/s, (c) 23m/s and (d) 46m/s.

When the impact velocity is increased to 23 m/s, the peak force at the impinged and the reaction force at the distal end have increased 8.1% and 19.9% respectively comparing to the static loading condition. Meanwhile the mean crushing force and the SEA has not been affected much. However the deformation mode is slightly different when compared to the static loading condition as the top layers of the C-crease core tends to be crushed prior to the bottom layer.

When the impact velocity is increased to 46 m/s, an obvious shock front is formed at the impinged end. As shown in Fig. 5.8 (d), the core is separated by the shock front into two portions: the condensed portion at the impinged end and the uncondensed portion at the distal end.

Comparing to the static loading condition, the peak contact force has been increased by 47.6% and the peak reaction force has been increased by 55.3%. The mean crushing force has been increased by 8.8% and the SEA has been increased by 17.1%.

5.3.2 Hybrid origami-honeycombs

5.3.2.1 MMCCSS and SSCCMM

The FEA results of MMCCSS and SSCCMM are summarized in Table 5.6 and Fig. 5.9. For both cases of MMCCSS and SSCCMM, the $P_{max\text{-}imp}$, P_m, $P_{max\text{-}dis}$ and SEA have all been increased with the increase of impact velocity. Especially for the specimen SSCCMM when subjected to the impact with the velocity of 46 m/s, the peak contact force at the impinged end has increased dramatically. While for the specimen MMCCSS when the S-crease layers are placed at the impinged end, the peak contact forces under different loading conditions are even less than the respective individual S-crease core. It can be also discovered that the S-crease layers will always be crushed prior to other layers in both cases (MMCCSS and SSCCMM) under different crushing speed.

Table 5.6: FEA results of hybrid MMCCSS and SSCCMM.

	$P_{max\text{-}imp}$ (kN)	P_m (kN)	$P_{max\text{-}dis}$ (kN)	*SEA* (kJ/kg)	Densification Strain
MMCCSS_QS	44.92	37.11	44.92	14.53	0.65
MMCCSS_4.6m/s	44.69	37.07	44.90	14.75	0.66
MMCCSS_23m/s	50.08	37.54	60.69	15.07	0.67
MMCCSS_46m/s	62.85	40.57	66.19	15.94	0.66
SSCCMM_QS	44.92	37.11	44.92	14.53	0.65
SSCCMM_4.6m/s	45.02	36.71	44.89	14.42	0.66
SSCCMM_23m/s	75.63	37.46	55.31	14.53	0.65
SSCCMM_46m/s	149.21	37.38	58.44	14.31	0.64

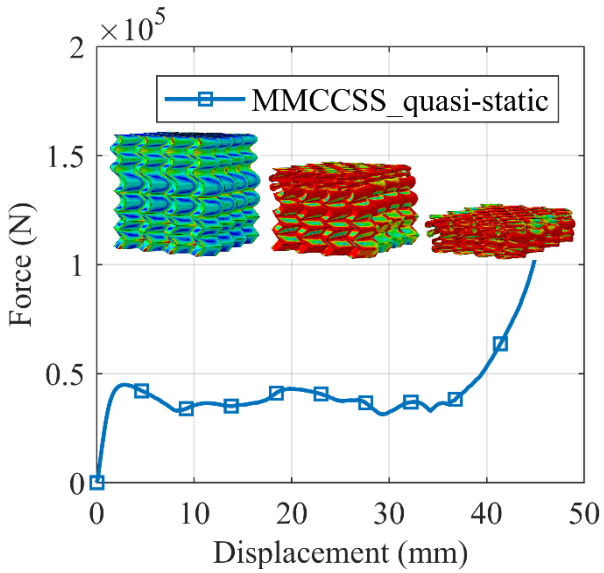
×10^5
2
1.5
1
0.5
0
Force (N)
MMCCSS_quasi-static
0
10
20
30
40
50
Displacement (mm)

(a)

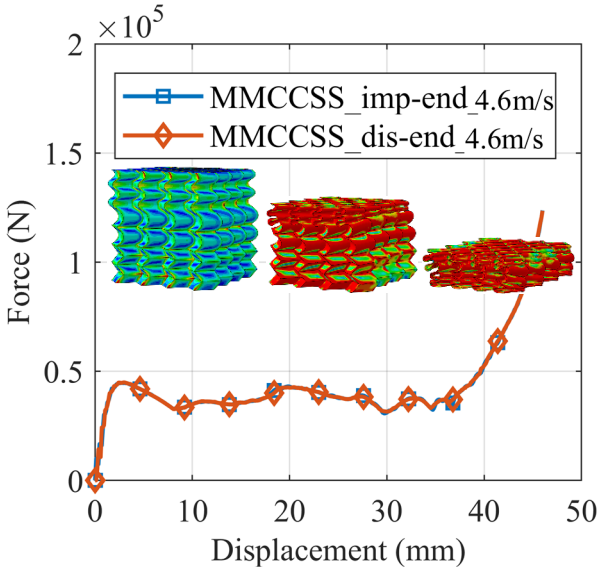
×10^5
2
1.5
1
0.5
0
Force (N)
MMCCSS_imp-end_4.6m/s
MMCCSS_dis-end_4.6m/s
0
10
20
30
40
50
Displacement (mm)

(b)

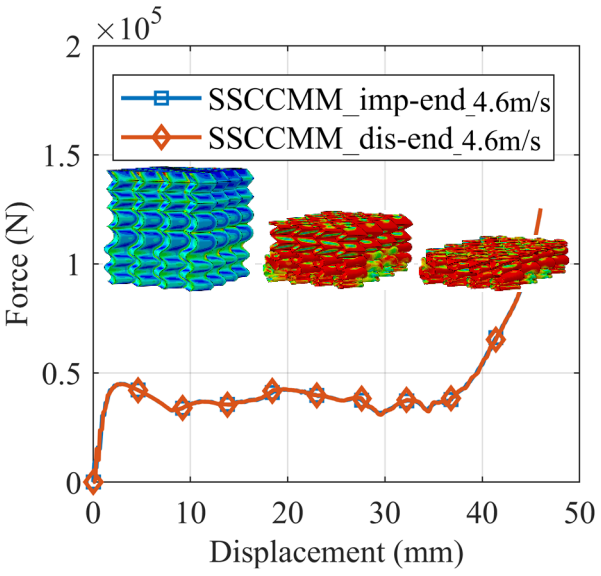
×10^5
2
1.5
1
0.5
0
Force (N)
SSCCMM_imp-end_4.6m/s
SSCCMM_dis-end_4.6m/s
0
10
20
30
40
50
Displacement (mm)

(c)

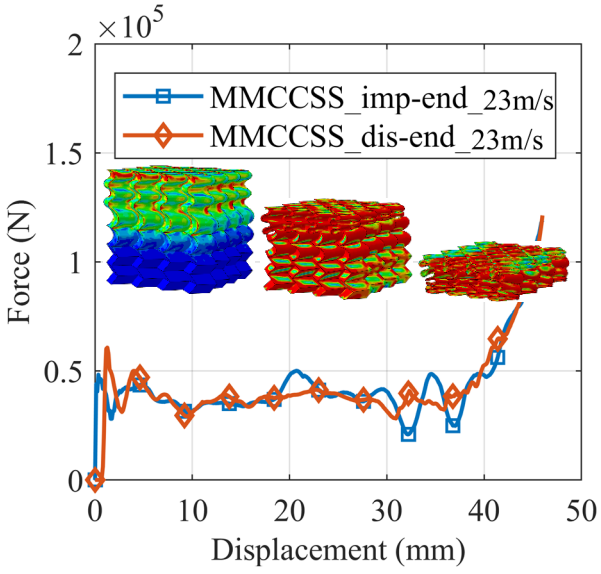
×10^5
2
1.5
1
0.5
0
Force (N)
MMCCSS_imp-end_23m/s
MMCCSS_dis-end_23m/s
0
10
20
30
40
50
Displacement (mm)

(d)

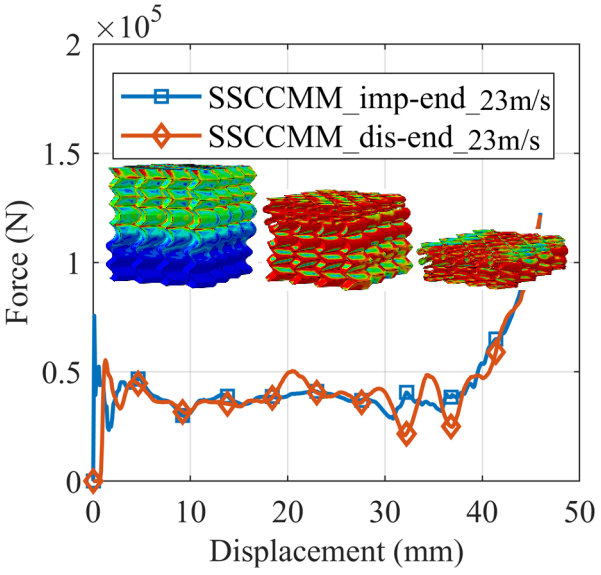
×10^5
2
1.5
1
0.5
0
Force (N)
SSCCMM_imp-end_23m/s
SSCCMM_dis-end_23m/s
0
10
20
30
40
50
Displacement (mm)

(e)

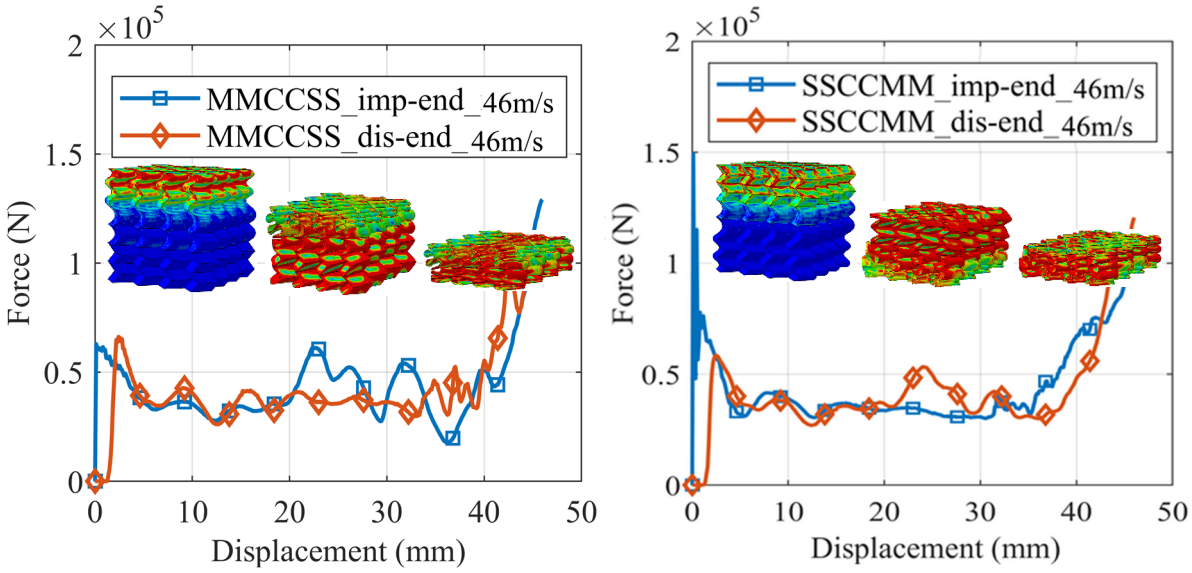

(f) (g)

Fig. 5.9 Numerical results of hybrid MMCCSS and SSCCMM: (a) Results of MMCCSS under quasi-static loading condition. Results of MMCCSS under dynamic loading condition with the velocity of (b) 4.6 m/s, (d) 23 m/s and (f) 46 m/s. Results of SSCCMM under dynamic loading condition with the velocity of (c) 4.6 m/s, (e) 23 m/s and (g) 46 m/s.

5.3.2.2 SCMMCS

The FEA results of SCMMCS are summarized in Table 5.7 and Fig. 5.10. It can be seen that the peak contact and reaction forces have an obvious increase when the loading speed is increased to 23m/s and 46m/s respectively. However, the mean crushing forces and the failure modes have not been influenced notably, despite there are some obvious fluctuations in the force-displacement curves when the loading speeds are 23m/s and 46m/s. While due to the notable increase of the densification strain when the loading speed is increase to 46m/s, the SEA of SCMMCS has been increased by 12% when comparing to the static condition.

Table 5.7: FEA results of hybrid SCMMCS.

	$P_{max\text{-}imp}$ (kN)	P_m (kN)	$P_{max\text{-}dis}$ (kN)	*SEA* (kJ/kg)	Densification Strain
SCMMCS_QS	46.50	40.37	46.50	15.50	0.64
SCMMCS_4.6m/s	46.99	40.24	46.91	15.50	0.64
SCMMCS_23m/s	52.52	40.34	56.52	16.05	0.66
SCMMCS_46m/s	70.89	40.92	58.84	17.35	0.71

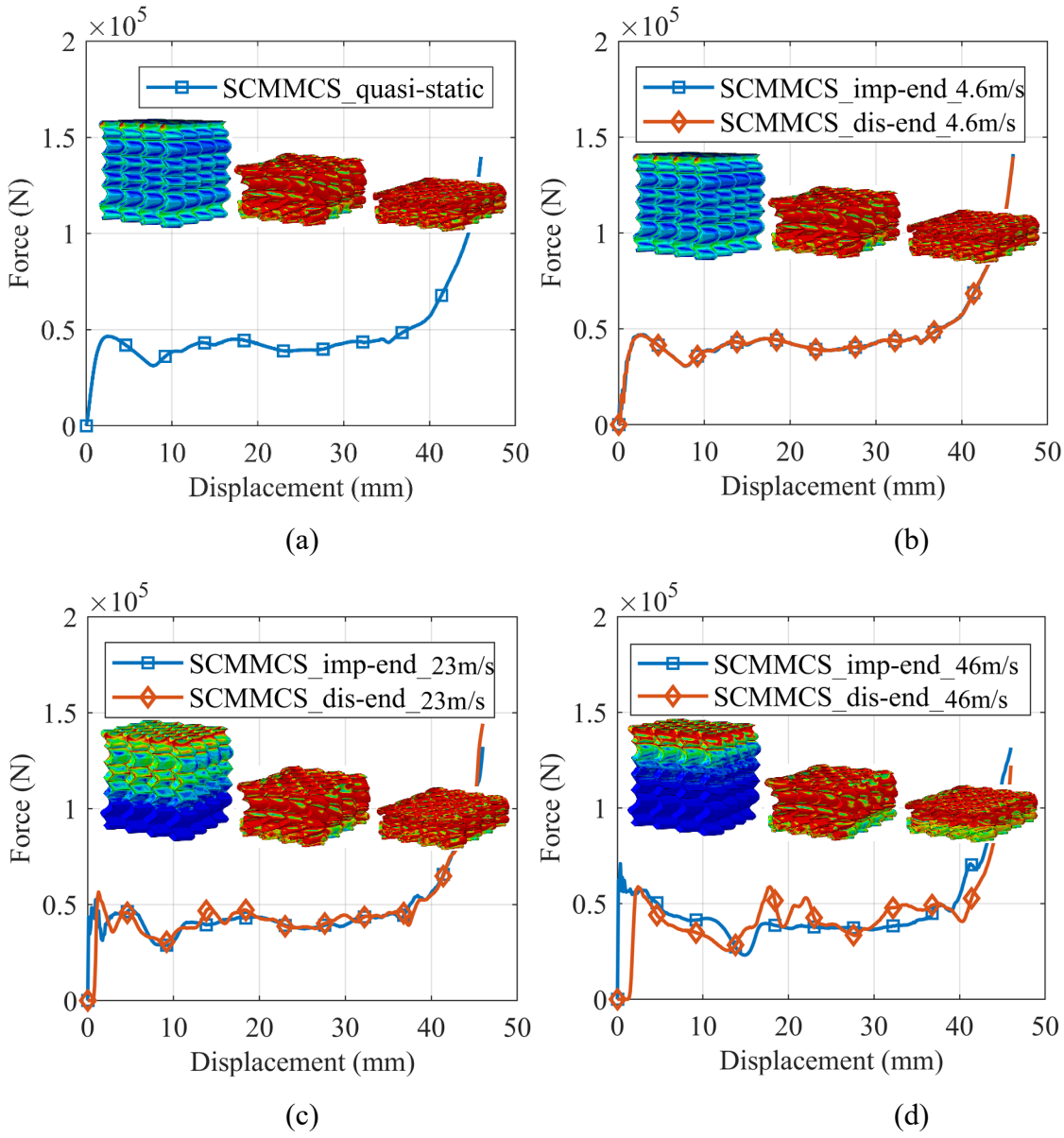

Fig. 5.10 Numerical results of hybrid SCMMCS: (a) Results under quasi-static loading condition. Results under dynamic loading condition with the loading velocity of (b) 4.6m/s, (c) 23m/s and (d) 46m/s.

5.3.2.3 MCSSCM

The FEA results of MCSSCM are summarized in Table 5.8 and Fig. 5.11. It can be seen that the $P_{max\text{-}imp}$, P_m, $P_{max\text{-}dis}$ and SEA have all been increased with the increase of impact velocity. The results of the force-displacement curves and failure modes of MCSSCM are quite similar to the case of SSCCMM. When the specimen MCSSCM is subjected to the impact with the velocity of 46m/s, the peak contact force at the impinged end has increased significantly and the S-crease layers will always be crushed prior to other layers under different crushing speed.

However the failure modes have not been changed significantly with the increase of loading speed.

Table 5.8: FEA results of hybrid MCSSCM.

	$P_{max\text{-}imp}$ (kN)	P_m (kN)	$P_{max\text{-}dis}$ (kN)	*SEA* (kJ/kg)	Densification Strain
MCSSCM_QS	47.20	38.55	47.20	14.42	0.63
MCSSCM_4.6m/s	47.06	38.16	46.92	14.42	0.63
MCSSCM_23m/s	75.45	38.56	61.50	15.29	0.66
MCSSCM_46m/s	204.18	40.39	65.74	17.02	0.70

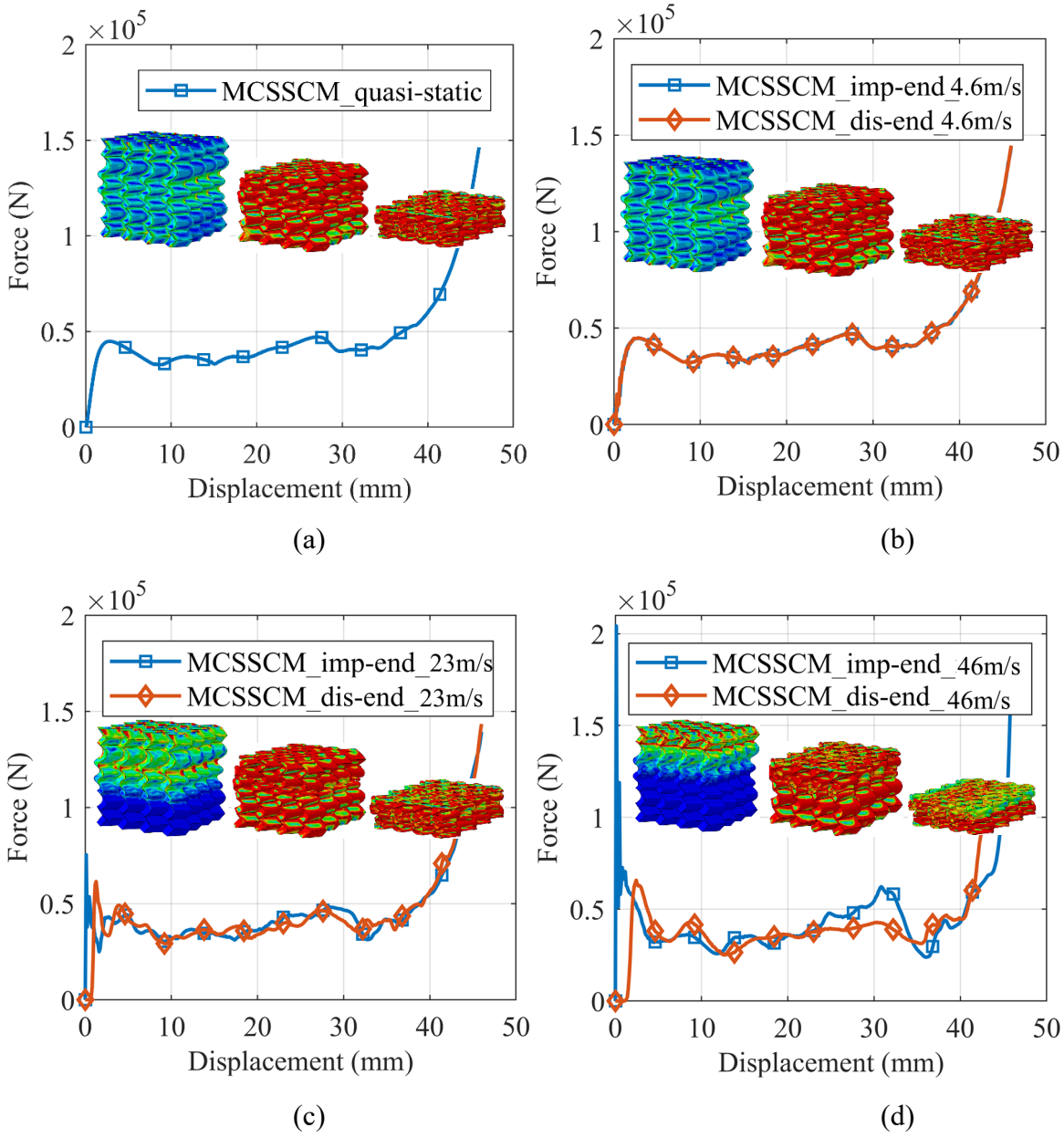

Fig. 5.11 Numerical results of hybrid MCSSCM: (a) Results under quasi-static loading condition. Results under dynamic loading condition with the loading velocity of (b) 4.6m/s, (c) 23m/s and (d) 46m/s.

5.4 Discussion

5.4.1 Loading speed

It can be seen from the results shown in Fig. 5.12 that in general, low velocity impact with the crushing speed of 4.6m/s has no apparent influence to these innovative origami-honeycombs when comparing to the static loading condition. When the loading speed is increased to 23m/s and 46m/s, the dynamic effects are rather apparent and P_{max}, P_m and SEA are all increased correspondingly. Especially when the Miura-ori layers are constructed at the impinged end, the contact force at the impact end will always be much higher than those of the other types. However in the case of SCMMCS when the S-crease layers are constructed in both top and bottom layers, P_m and SEA are the highest among all loading conditions and the contact and reaction forces are relatively lower than those of any other origami-honeycombs.

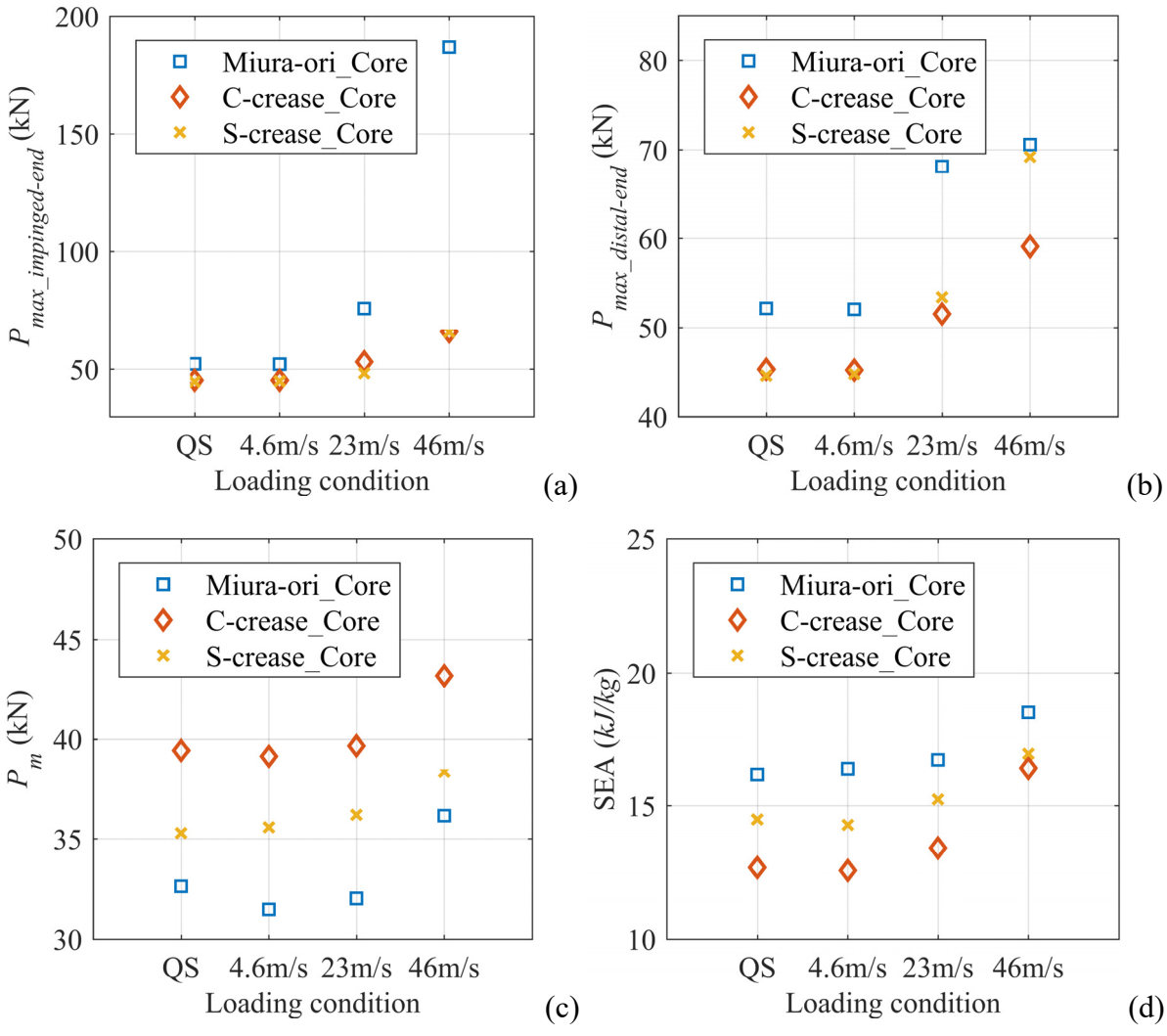

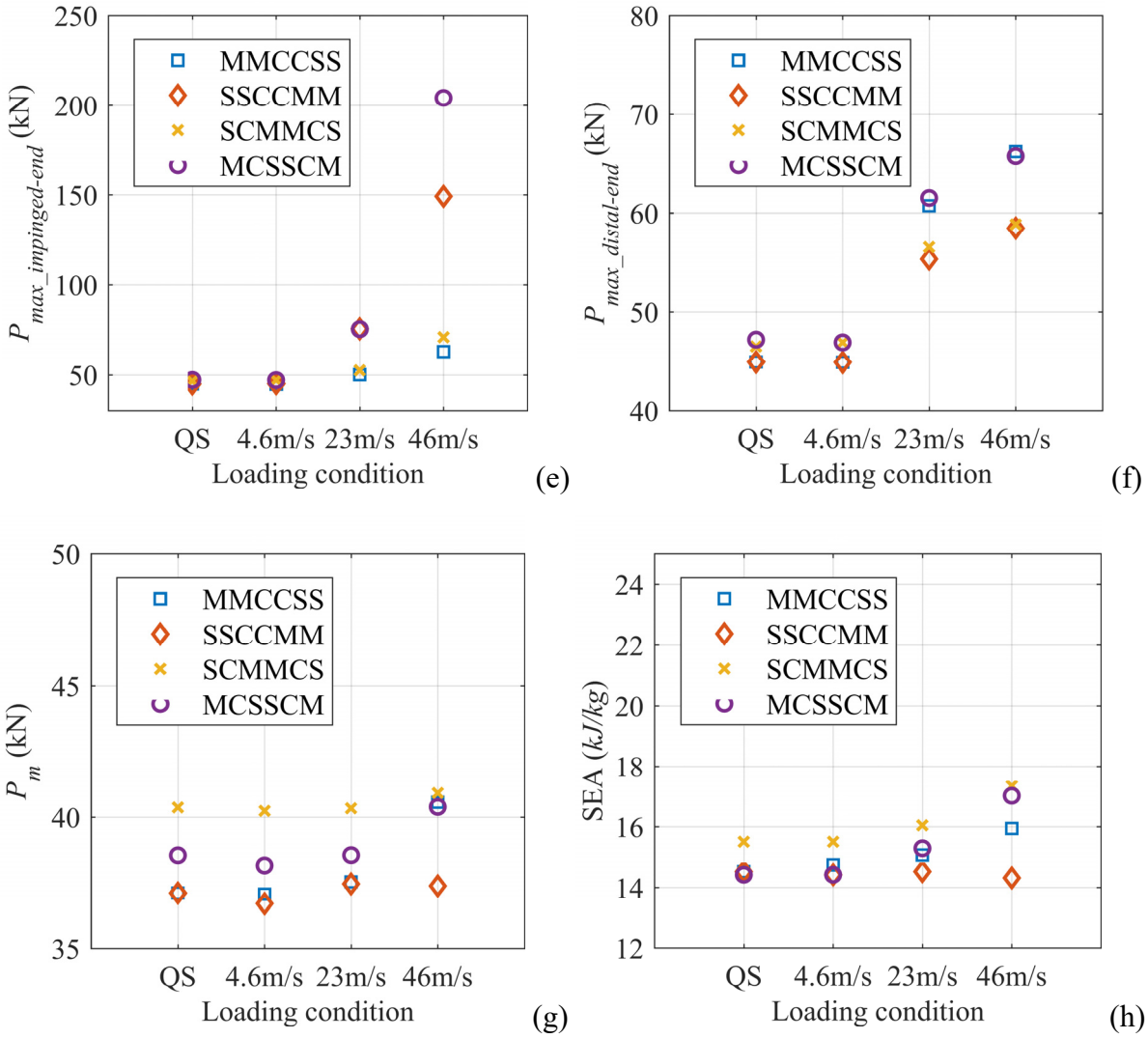

Fig. 5.12 Effect of loading speed: (a) P_{max} at impinged end vs loading condition (derivative cores); (b) P_{max} at distal end vs loading condition (derivative cores); (c) mean crushing force vs loading condition (derivative cores); (d) SEA vs loading condition (derivative cores); (e) P_{max} at impinged end vs loading condition (hybrids); (f) P_{max} at distal end vs loading condition (hybrids); (g) mean crushing force vs loading condition (hybrids); (h) SEA vs loading condition (hybrids).

The results has illustrated that for the proposed novel derivative Miura-ori-based honeycombs, with the increase of compressive loading speed, the contact and reaction forces, as well as the SEA will all be increased. In order to increase the SEA and minimize the damage caused by the impact, origami-honeycomb constructed in a stiffness gradient of weak-strong-weak order will

be ideal and effective. For example under the impact with the velocity of 46m/s, the hybrid origami-honeycomb SCMMCS reduced $P_{max\text{-}imp}$ by 62% comparing to the Miura-ori core.

5.4.2 Hybridization

It can be seen from Fig. 5.13 that under dynamic loading, when the Miura-ori layers are placed the impinged end, the peak contact forces and the peak reaction forces will always be excessively higher than other cases. While for the lowest peak reaction force always occurred when the C-crease or S-crease layers are placed at the distal end. By comparing the results, it can be found that by far, the hybrid model SCMMCS has the best functionality among other specimens in terms of relatively higher SEA and lower contact and reaction forces. This shows that the process of hybridization indeed can manipulate the functionality of the material, and furthermore when the energy absorbing material is constructed with the stiffness gradient of weak-strong-weak order, it will help to increase the SEA while reducing the peak forces at the same time.

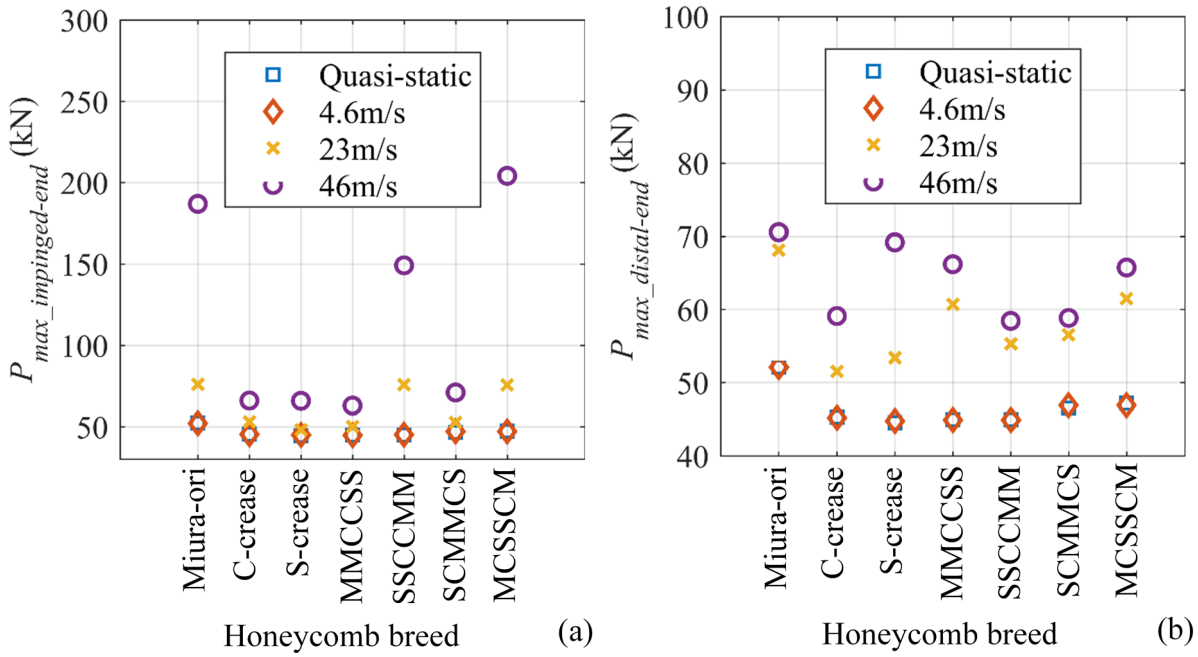

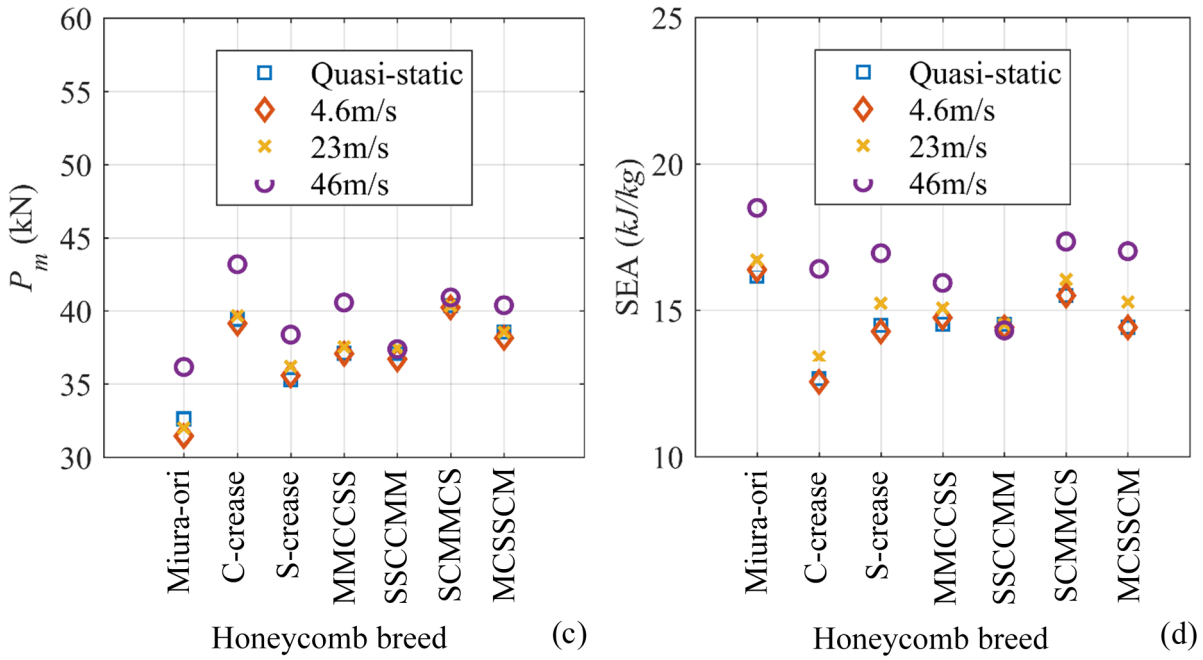

Fig. 5.13 Effect of hybridization under different loading conditions: (a) P_{max} at impinged end vs honeycomb breed; (b) P_{max} at distal end vs honeycomb breed; (c) mean crushing force vs honeycomb breed; (d) SEA vs honeycomb breed.

5.4.3 Theoretical prediction vs. FE result

Previously, the theoretical prediction of the dynamic mean crushing stress of the origami honeycomb cores were proposed. According to section 5.1 and sub-section 5.3.1, the theoretical predictions of σ_d were summarized and compared with the FE results in Table 5.9. A group of additional simulations of origami honeycomb cores under impact were conducted with a higher crushing speed (92mm/s), in order to evaluate the applicable range of the theoretical prediction qualitatively.

Table 5.9 Dynamic mean crushing stress under different crushing velocities.

	σ_d (Mpa)							
	4.6 mm/s		23 mm/s		46 mm/s		92 mm/s	
	FE	Theory	FE	Theory	FE	Theory	FE	Theory
Miura-ori	12.6	13.1	12.8	13.5	14.5	14.7	20.1	19.6
C-crease	15.7	15.8	15.9	16.4	17.3	18.0	22.3	24.4
S-crease	14.2	14.1	14.5	14.6	15.4	16.0	20.5	21.6

By comparing the results in Table 5.9, it can be found that in most cases the theoretical predictions are slightly higher than the FE results, but the differences are only around 5%. Hence, it can be concluded that the proposed theoretical prediction is able to qualitatively predict the dynamic mean crushing stress.

5.5 Summary

Six types of unique derivative Miura-ori-based honeycombs, including three hybrid origami-honeycombs with different stiffness gradients, have been studied numerically under different compressive loading conditions. Especially, it has been found that under dynamic loading condition, the hybrid origami-honeycombs with certain stiffness gradient can reduce the impact and transmitted force, and meanwhile the gradient can also help to increase the energy absorption efficiency. Finally, conclusions are summarized as follows:

1) When the impact speed is relatively low, there is not apparent influence towards the derivative Miura-ori-based honeycombs in terms of contact and reaction forces, as well as the SEA. The failure modes are also respectively identical to the ones under static loading condition.
2) When the derivative Miura-ori-based honeycombs are subject to impact with intermediate and relatively higher velocity, The SEA, P_m and P_{max} will all be increased correspondingly due to the dynamic effect. Meanwhile the failure modes of Miura-ori and S-crease layers are more sensitive to the dynamic loading, as when the loading speed is increased to 46m/s, those layers placed at the impinged end will be crushed and densified prior to the distal layers.
3) The Miura-ori layers possesses the highest value of SEA under dynamic loading condition, however the relative impact and transmitted forces are excessively higher than any other types of derivative Miura-ori-based honeycombs.

4) The hybrid origami-honeycombs with stiffness gradient in weak-strong-weak order can noticeably reduce the impact and transmitted force under dynamic loadings. Meanwhile, they can also increase the energy absorption efficiency, which is quite desirable for ideal energy absorbing structures and materials.
5) The theoretical prediction of the dynamic mean crushing stress of the origami honeycomb cores is able to predict the FE result qualitatively.

In conclusion, this work has proved that the proposed novel derivative Miura-ori-based honeycombs with the unique function of hybridization can decrease the impact transmission and meanwhile increase the energy absorption capacity during crush. It is shown that the concept of hybridization can be efficiently adopted to design novel and ideal energy absorbing structures and materials under dynamic loadings.

Chapter 6

Conclusion

This thesis has been primarily concerned with the development and improvement of origami-inspired honeycombs suitable for high-performance energy absorption applications. The major findings of this thesis can be summarized with the following conclusions.

6.1 Summary of findings

6.1.1 Miura-ori honeycomb

Chapter 3 has introduced a unique origami-inspired Miura-ori honeycomb with stiffness gradient and self-locking feature has been designed as a high-performance energy absorbing material. Experimental and numerical analyses are conducted to study the mechanical behaviors of the honeycomb. It is found that with proper design, this unique honeycomb with special self-locking feature can reduce the peak force of more than 50% and remain efficient in energy absorption.

The wall thickness of Miura-ori honeycomb can influence the deformation mode, as well as the SEA in a great manner, and it is shown from the obtained results that properly increasing wall thickness can optimize the deformation pattern of the structure and enhance the SEA significantly.

The mechanical properties of the base material also play an important role in terms of deformation mode and peak force. It is likely that the material with more elastic dominated properties can lead the Miura-ori honeycomb to a more desired deformation mode. However, typical metal materials are more efficient in term of SEA when a proper design is selected.

6.1.2 Derivative Miura-ori-based honeycombs

Chapter 4 has presented the Miura-ori honeycomb core, as well as the C-crease and S-crease honeycomb cores that derived from the Miura-ori. All origami-honeycomb cores can be assembled along the out-of-plane direction and create the hybrid origami-honeycombs with different stiffness gradient.

Static analyses have been carried out on the derivative Miura-ori based honeycombs experimentally and numerically. It has been found that under static loading condition, the hybridization of Miura-ori extended honeycomb cores with the stiffness gradient in the weak-strong-weak order can reduce the peak force and meanwhile increase the energy absorption efficiency.

6.1.3 Effects of dynamic loading on origami-honeycombs

Numerical analyses of derivative Miura-ori-based honeycombs under dynamic compressive loadings have been carried out in Chapter 5. It has been found that when the impact speed is relatively low, there is no apparent influence towards the derivative Miura-ori-based honeycombs in terms of contact and reaction forces, as well as the SEA. The failure modes are also similar to the ones under static loading condition.

It has also been found that when the derivative Miura-ori-based honeycombs are subject to impact with intermediate and relatively higher velocity, the SEA, P_m and P_{max} will all be increased correspondingly due to the dynamic effect. Meanwhile the failure modes of Miura-ori and S-crease layers are more sensitive to the dynamic loading.

Most importantly, it has been shown that the hybrid origami-honeycombs with stiffness gradient in weak-strong-weak order can reduce the impact transmission under dynamic loadings and at the same time it can also increase the energy absorption efficiency.

6.2 Future work

This thesis has created and developed several origami-inspired novel honeycombs for energy absorption applications, and has made preliminary studies on the mechanical behaviors of these novel metamaterials based on experimental and numerical approaches. However, in order to have deeper understanding of the behavior of these origami-honeycombs, and to develop more innovative energy absorbing materials by using existing origami patterns, the following areas of studies can be carried out in the future.

- **Geometric design**

  The hybrid origami-honeycombs studied in this thesis are constructed with different derivative Miura-oir-based cores, but without intentional self-locking features. It will be interesting to add flange layers or assign steeper stiffness gradient to the hybrid origami-honeycombs and to study the mechanical behavior of the subsequent hybrid honeycombs.

  This thesis has proved that the concept of Miura-ori can be efficiently adopted to serve as an ideal energy absorbing material. However, there are numerous origami patterns created by origami artists could also be potentially beneficial for the design of innovative energy absorbing structures and materials. Therefore, different origami patterns shall be adopted to serve as the innovative concept of optimized energy absorbing structures and materials in the future.

- **Dynamic test**

  The dynamic response of origami-inspired honeycombs has been only studied numerically in the present work. In the future work, experiments of origami-inspired honeycombs under different impact velocities shall be conducted. For low and intermediate velocity impact tests, drop hammer technique shall be used. Typical instrumentation includes an accelerator

attached to the impact hammer, a device for measuring the velocity just before impact, a displacement transducer to record the movement of the hammer and a dynamic load cell. For high velocity impact tests, where the strain rates are ranging from 10^2-$10^4 s^{-1}$, the split Hopkinson pressure bar (SHPB) shall be adopted to investigate the energy absorption capability and the impact resistance of origami honeycombs experimentally. For extremely high velocity impact, usually with the impact velocities in the range of 100-8000m/s, the Taylor impact technique has been widely employed. In this technique, the experimental specimen will be shot out from a gas gun and cause an impact on a rigid flat anvil, and high speed camera is used to record the displacement. However, the SHPB and Taylor impact techniques have a limitation that the size of the experimental specimen requires to be small, as the general inside diameters of the gas gun barrel are ranging from 10-100 mm (ASM, 2000). Due to the geometric complexity of origami honeycombs, it is rather difficult to manufacture small-sized specimens without using 3D-printing, but the cost of 3D-printed metal specimens is significantly high at the moment. Thus, new fabricating approaches shall be developed in the future, and the conventional manufacturing techniques shall be attempted to fabricate origami honeycombs.

- **Manufacturing feasibility**

  The Stamping technique can be potentially feasible of manufacturing the wall layers of Miura-ori honeycombs and attempts should be made in the future. The stamp-formed wall layers can be herby welded together to form the honeycomb. However, detrimental geometric imperfections will be introduced during this manufacturing process which will significantly increase the difficulty of numerical modeling and affect the accuracy of relevant FE analysis. In this case, 3D scanning technique shall be used to scan and generate actual geometries of the 3D-printed models, then the scanned model will be imported to CAE software for subsequent FE analysis.

- **Numerical Model**

  In the present FE analysis of origami honeycombs under impact, material damage was not considered and only an elastic-perfectly plastic material model was assigned to the simulation. In the future, an improved FE model shall be created with added re-mesh and material damage. A more advanced plasticity model ─ the Johnson-Cook model with strain rate effects, shall be used in the FE analysis, and the variables of the Johnson-Cook model can be obtained by conducting SHPB impact experiments of the base material of which the origami honeycomb was made. With the improved FE model, an adequate amount of simulations of origami honeycombs under high velocity impact can be conducted, and the relations of relevant parameters against impact speed can be obtained qualitatively. For example the relation of transmitted force vs. impact velocity, or SEA vs. impact velocity.

- **Theoretical analysis**

  The effective crushing distance, or the equivalent densification strain, plays an important role in determining the P_m and SEA of origami honeycombs. When there is a clear boundary in between the plateau and densification regions, the effective crushing distance can be easily identified. When there is no clear boundary, as the onset of densification is vague, an empirical equation (Eq. (3.10)) to describe the densification strain for conventional cellular materials was proposed by Gibson and Ashby (1997). However, as discussed previously that this equation is not valid for the origami-honeycombs in the present work. The current technique used to determine the effective crushing distance is the combination of reading load-displacement curve and visually observing the deformation of the model. This method has been concluded to be effective in the present work, for example in Chapter 5, the dynamic mean crushing stresses obtained by FEM vary only around 5% from the theoretical predictions. However, this method is not practically efficient and may lead to misleading results. Thus, a standardized analytical approach that used to define the

effective crushing distance or the equivalent densification strain of certain origami honeycomb shall be developed in the future.

With the help of experiments and FE analyses, it shall be able to develop the theoretical model and give analytical solutions for origami-inspired honeycombs under dynamic loading in the future. For example the analytical solution of 'SEA vs Impact velocity' of origami honeycombs. Meanwhile, dynamic response of origami-inspired honeycombs with self-locking feature can also be studied numerically, experimentally and analytically. However, because of the self-locking feature, the stress wave propagations in origami-inspired honeycombs will be extraordinarily more complex than those in conventional honeycombs. Therefore, the related theoretical analyses would be rather challenging.

References

Abaqus, version 2016. Abaqus Analysis User's Guide, SIMULIA corp., RI, USA, 2016.

Ajdari, A., Nayeb-Hashemi, H., Vaziri, A. Dynamic crushing and energy absorption of regular, irregular and functionally graded cellular structures. International Journal of Solids and Structures, 2011, 48 (3-4), 506-516.

Alghamdi, A.A.A. Collapsible impact energy absorbers: an overview. Thin-Walled Structures, 2001, 39 (2), 189-213.

Al-Hassani, S.T.S., Johnson, W., Lowe, W.T. Characteristics of inversion tube under axial loading. Mech. Engng. Sci., 1972, 14, 370-381.

Ashby, M.F., Evans, A., Fleck, N.A., Gibson, L.J., Hutchinson, J.W., Wadley, H.N.G. Metal Foams: A Design Guide. Butterworth-Heinemann, Boston MA, 2000.

ASM. Materials properties handbook: Titanium Alloys. ASM International, 2007, 483-636.

ASM. Handbook Volume 8: Mechanical testing and evaluation. ASM International, 2000.

ASTM D638, Standard Test Method for Tensile Properties of Plastics, ASTM International, West Conshohocken, PA, 2014.

Baranger, E., Cluzel, C., Guidault, P.A. Modelling of the behavior of aramid folded cores up to global crushing. Strain, 2011, 47, 170-178.

Baroutaji, A., Sajjia, M., Olabi, A.G. On the crashworthiness performance of thin-walled energy absorbers: Recent advances and future developments. Thin-Walled Structures, 2017, 118, 137-163.

Besant, T., Dacies, GAO., Hitchings, D. Finite element modelling of low velocity impact of composite sandwich panels. Composites: Part A, 2001, 32, 1189-1196.

Bates, S.R.G., Farrow, I.R., Trask, R.S. 3D printed polyurethane honeycombs for repeated railored energy absorption. Materials and Design, 2016, 112, 172-183.

Chen, C., Lu, TJ., Fleck, NA. Effect of inclusions and holes on the stiffness and strength of honeycombs. International Journal of Mechanical Sciences, 2001, 43, 487-504.

Chen, D.H., Ushijima, K. Estimation of the initial peak load for circular tubes subjected to axial impact. Thin-Walled Structures, 2011, 49 (7), 889-898.

Chirwa, E.C. Theoretical-analysis of tapered thin-walled metal inverbuck tube. International Journal of Mechanical Sciences, 1993, 35 (3-4), 325-351.

Crupi, V., Epasto, G., Guglielmino, E. Comparison of aluminium sandwiches for lightweight ship structures: Honeycomb vs. foam. Marine Structures, 2013, 30, 74-96.

Department for Transport, Vehicles involved in reported personal injury road accidents, RAS20009, 27 Sep. 2018.

Department for Transport, Licensed vehicles at the end of the quarter by body type, VEH0101, 27 June 2019.

Duan, S.Y., Tao, Y., Lei H., Wen, W., Liang, J., Fang, D.N. Enhanced out-of-plane compressive strength and energy absorption of 3D printed square and hexagonal honeycombs with variable-thickness cell edge. Extreme Mechanics Letters, 2018, 18, 9-18.

Elgalai, A.M., Mahdi, E., Hamouda, A.M.S., Sahari, B.S. Crushing response of composite corrugated tubes to quasi-static axial loading. Composite Structures, 2004, 66 (1-4), 665-671.

Fan, Z., Shen, J., Lu, G. Investigation of Lateral Crushing of Sandwich Tubes. In Proceedings of the Twelfth East Asia-Pacific Conference on Structural Engineering and Construction, Vol. 14, 2011.

Fathers, R.K., Gattas, J.M., You, Z. Quasi-static crushing of eggbox, cube, and modified cube foldcore sandwich structures. International Journal of Mechanical Sciences, 2015, 101, 421-428.

Gattas, JW., Wu, W., You, Z. Miura-base rigid origami: Parameterizations of first-level dericative and piecewise geometries. Journal of Mechanical Design, 2013, 135, 111011.

Gattas, J. M. & You, Z. Quasi-static impact of indented foldcores. International Journal of Impact Engineering, 2014a, 73(11), 15-29.

Gattas, J. M. & You, Z. Miura-base rigid origami: Parametrizations of curved-crease geometries. Journal of Mechanical Design, 2014b, 136(12), 121404.

Gattas, J.M., You, Z. Geometric assembly of rigid-foldable morphing sandwich structures. Engineering Structures, 2015, 94 149-159.

Gattas, J.M., You, Z. Design and digital fabrication of folded sandwich structures. Automation in Construction, 2016, 63 79-87.

Garrett, D., You, Z. & Gattas, J. M. Curved crease tube structures as an energy absorbing crash box. Proceedings of the ASME International Design Engineering Technical Conferences and Computers and Information in Engineering Conference (IDETC/CIE), 2016, 1-9, Charlotte, North Carolina.

Gibson, L.J. and Ashby, M.F. Cellular Solids: Structure and Properties. 2nd Edition, 1997, Cambridge University Press, Cambridge.

Gilkie, R.C., Sundararaj, P. Impact resistance of plastic sandwich constructions using low density urethane cores. Journal of Cell Plastics, 1971, 7.

Grzebieta, RH. & Murray, NW. The static behavior of struts with initial kinks at their centre point. International Journal of Impact Engineering, 1985, 3, 155-165.

Gupta, N.K., Abbas, H. Lateral collapse of composite cylindrical tubes between flat platens. International Journal of Impact Engineering, 2000, 24 (4), 329-346.

Hill, R. Mathematical theory of plasticity. Oxford University Press, 1950.

Horrigan, DPW, Aitken, RR, Moltschaniwskyj, G. Modeling of crushing due to impact in honeycomb sandwiches. Journal of Sandwich Structure and Materials, 2000, 2(2), 131-151.

Hu, L.L., Yu, T.X. Mechanical behavior of hexagonal honeycombs under low-velocity impact - theory and simulations. International Journal of Solids and Structures, 2013, 50 (20-21), 3152-3165.

Hu, L.L., He, X.L., Wu, G.P., Yu, T.X. Dynamic crushing of the circular-celled honeycombs under out-of-plane impact. International Journal of Impact Engineering, 2015, 75 150-161.

Jones, N. Recent studies in the dynamic plastic behavior of structures. Appl Mech Rev, 1989, 42.

Karagiozova, D., Jones, N. Dynamic elastic-plastic buckling of circular cylindrical shells under axial impact. International Journal of Solids and Structures, 2000, 37 (14), 2005-2034.

Karagiozova, D., Jones, N. On dynamic buckling phenomena in axially loaded elastic-plastic cylindrical shells. International Journal of Non-Linear Mechanics, 2002, 37 (7), 1223-1238.

Karagiozova, D., Alves, M., Propagation of compaction waves in cellular materials with continuously varying density. International Journal of Solids and Structures, 2015, 71, 323-337.

Lefebvre, LP, Banhart, J., Dunand DC. Porous metals and metallic foams: Current status and recent developments. Advanced Engineering Materials, 2008, 10(9), 775-787.

Liu, H., Ding, S., Feng, B. Impact response and energy absorption of functionally graded foam under temperature gradient environment. Composites Part B: Engineering, 2019, 172, 516-532.

Li, Y., You, Z. Thin-walled open-section origami beams for energy absorption. Proceedings of the ASME IDETC/CIE, 2014, 1-9, Buffalo, New York.

Li, Y., You, Z. Multi-corrugated indented foldcore sandwich panel for energy absorption. Proceedings of the ASME IDETC/CIE, 2015, 1-7, Boston, Massachusetts.

Liu, J., Hou, B., Lu, F., Zhao, H. A theoretical study of shock front propagation in the density graded cellular rods. International Journal of Impact Engineering, 2015, 80, 133-142.

Ma, J., Thin-walled tubes with pre-folded origami patterns as energy absorption devices. Ph.D Dissertation, University of Oxford, 2011.

Ma, J., You, Z. Energy absorption of thin-walled beams with a pre-folded origami pattern. Thin-Walled Structures, 2013a, 73, 198-206.

Ma, J., Hou, D., Chen, Y., You, Z. Quasi-static axial crushing of thin-walled tubes with a kite-shape rigid origami pattern: Numerical simulation. Thin-Walled Structures, 2016, 100, 38-47.

Martin, J.B. Plasticity: Fundamentals and general problems. M.I.T. Press Cambridge, 1975.

Meyers, M.A. Dynamic Behavior of Materials. John Wiley & Sons, Inc. 1994.

Miura, K. Zeta-core sandwich-Its concept and realization. Inst. Space Aeronaut. Sci., Univ. Tokyo. 1972, 480, 137-164.

Muhammad, A. Study of a compact energy absorber. Ph.D Dissertation, Iowa State University, 2007.

Murray, NW. The determination of the collapse loads of rigidly jointed frameworks with members in which the axial forces are large. 1956, Proc. Inst. Civ. Engrs. Pt. III, Vol. 5.

Murray, NW. The static approach to energy dissipation in some thin-walled steel structures. Structure crushworthness (Jones. N. and Wierzbicki. T. Eds), Butterworth, London. 1983.

Nemat-Nasser, S., Kang, W.J., McGee, J.D., Guo, W.G., Isaacs, J.B. Experimental investigation of energy-absorption characteristics of components of sandwich structures. International Journal of Impact Engineering, 2007, 34 (6), 1119-1146.

Pang, T., Kang, H.H., Yan, X.L., Sun G.Y., Li, Q. Crashworthiness design of functionally graded structures with variable diameters. International Journal of Crashworthiness, 2017, 22 (2), 148-162.

Papka, S.D., Kyriakides, S. Biaxial crushing of honeycombs - Part I: Experiments. International Journal of Solids and Structures, 1999a, 36 (29), 4367-4396.

Papka, S.D., Kyriakides, S. In-plane biaxial crushing of honeycombs - Part II: Analysis. International Journal of Solids and Structures, 1999b, 36 (29), 4397-4423.

Prager, W., Hodge, P.G., Jr. Theory of perfect plastic solids. John Wiley, New York.

PTC Creo 4.0, Parametric Technology Corp. 2018. Boston, USA.

Rajabiehfard, R., Darvizeh, A., Alitavoli, M., Sadeghi, H., Noorzadeh, N., Maghdouri, E. Experimental and numerical investigation of dynamic plastic behavior of tube with different thickness distribution under axial impact. Thin-Walled Structures, 2016, 109 174-184.

Rawat, S., Narayanan, A., Nagendiran, T., Upadhyay, A.K. Collapse behavior and energy absorption in elliptical tubes with functionally graded corrugations. In Plasticity and Impact Mechanics, Gupta, N. K.,Iqbal, M. A., Eds. 2017, 173, 1374-1381.

Reid, S.R., Peng, C. Dynamic uniaxial crushing of wood. Int. J. Impact. Eng, 1997, 19, 531-570.

Santosa, S., Wierzbicki, T. Crash behavior of box columns filled with aluminum honeycomb or foam. Computers & Structures, 1998, 68 (4), 343-367.

Santosa, S., Wierzbicki, T. Effect of an ultralight metal filler on the bending collapse behavior of thin-walled prismatic columns. International Journal of Mechanical Sciences, 1999, 41 (8), 995-1019.

Shen, C. J., Lu, G., Yu, T. X. Dynamic behavior of graded honeycombs – A finite element study. Composite Structures, 2013a, 98(3), 282-293.

Shen, C. J., Yu, T. X., Lu, G. Double shock mode in graded cellular rod under impact. International Journal of Solids and Structures, 2013b, 50(1), 217-233.

Song, J., Chen, Y., Lu, G. Axial crushing of thin-walled structures with origami patterns. Thin-Walled Structures, 2012, 54, 65-71.

Stronge, W.J., Yu, T.X., Johnson, W. Long stroke energy dissipation in splitting tubes. International Journal of Mechanical Sciences, 1983, 25 (9-10), 637-647.

Sun, G., Wang, E., Wang, H., Xiao, Z., Li, Q. Low-velocity impact behavior of sandwich panels with homogeneous and stepwise graded foam cores. Material & Design, 2018, 160, 1117-1136.

Tai, Y.S., Huang, M.Y., Hu, H.T. Axial compression and energy absorption characteristics of high-strength thin-walled cylinders under impact load. Theoretical and Applied Fracture Mechanics, 2010, 53 (1), 1-8.

Wang, A., Tian, W. Mechanism of buckling development and strain reversal occurrence in elastic-plastic cylindrical shells under axial impact. International Journal of Non-Linear Mechanics, 2008, 43 (8), 722-732.

Wang, E., Li, Q., Sun, G. Computational analysis and optimization of sandwich sandwich panels with homogeneous and graded foam cores for blast resistance. Thin-Walled Structures, 2020, 147: 106494.

Wang, Z., Tian, H., Lu, Z., Zhou, W. High-speed axial impact of aluminum honeycomb-Experiment and simulations. Composites: Part B, 2014, 56, 1-8.

Wierzbicki, T., Abramowicz, W. On the crushing mechanics of thin-walled structures. Transactions of the ASME. Journal of Applied Mechanics, 1983, 50 (4A), 727-734.

Xie, W.H., Meng, S.H., Ding, L., Jin, H., Du, S.Y., Han, G.K., Wang, L.B., Xu, C.H., Scarpa, F., Chi, R.Q. High-temperature high-velocity impact on honeycomb sandwich panels. Composites Part B Engineering, 2017, 138, 1-11.

Xu, M.M., Huang, G.Y., Feng, S.S., Qin, X.Y., McShane, G.J., Stronge, W.J. Perforation resistance of aluminum / Polyethylene sandwich structure. Materials and Design, 2016, 100, 92-101.

Xu, S., Beynon, J.H., Ruan, D., Lu, G.X. Experimental study of the out-of-plane dynamic compression of hexagonal honeycombs. Composite Structures, 2012, 94 (8), 2326-2336.

Xue, Z.Y., Hutchinson, J.W. Preliminary assessment of sandwich plates subject to blast loads. International Journal of Mechanical Sciences, 2003, 45 (4), 687-705.

Yamada, Y., Banno, T., Xie, Z., Wen, C. Energy absorption and crushing behavior of foam-filled aluminium tubes. Materials Transactions, 2005, 46(12), 2633-2636.

Yang, K., Xu, S.Q. Shen, J.H., Zhou, S.W., Xie, Y.M. Multi-objective optimization of multi-cell tubes with origami patterns for energy absorption. Thin-Walled Structures, 2018, 123, 100-113.

Yang, K., Xu, S.Q. Shen, J.H., Zhou, S.W., Xie, Y.M. Energy absorption of thin-walled tubes with pre-folded origami patterns: Numerical simulation and experimental verification. Thin-Walled Structures, 2016, 03, 33-44.

Yasui, Y. Dynamic axial crushing of multi-layer honeycomb panels and impact tensile behavior of the component members. International Journal of Impact Engineering, 2000, 24 (6-7), 659-671.

Ying, L., Dai, M.H., Zhang, S.Z., Ma, H.L., Hu, P. Multiobjective crashworthiness optimization of thin-walled structures with functionally graded strength under oblique impact loading. Thin-Walled Structures, 2017, 117, 165-177.

Yu, T., Lu, G. Energy absorption of structures and materials. WP Ltd & CRC Press LLC, 2003.

Zahran, M.S., Xue, P., Esa, M.S., Abdelwahab, M.M., Lu, G.X. A New Configuration of Circular Stepped Tubes Reinforced with External Stiffeners to Improve Energy Absorption Characteristics Under Axial Impact. Latin American Journal of Solids and Structures, 2017, 14 (2), 292-311.

Zakirov, I., Nikitin, A., Alekseev, K.A., Mudra, C. Folded structures: Performance, technology and production. Latest Advancements of Applied Composite Technolygies. In proceeding of the 27th indernatinal SAMPE and Process Engineering, 2006, Paris, France.

Zakirov, I., Paimushin, V.N., Alekseev, K. Composite structures from polymer matrix materials for the aerospace sector. In proceeding of the 3rd congress for the polymer composite materials technologies, 2010, Modena, Italy.

Zhang, X., Cheng, G., You, Z., Zhang, H. Energy absorption of axially compressed thin-walled square tubes with patterns. Thin-Walled Structures, 2007, 45 (9), 737-746.

Zhang, X., Zhang, H., Wen, Z. Experimental and numerical studies on the crush resistance of aluminum honeycombs with various cell configurations. International Journal of Impact Engineering, 2014, 66, 48-59.

Zheng, J., Xiang, J., Luo, Z., Ren, Y. Crashworthiness design of transport aircraft subfloor using polymer foams. Internationl Journal of Crashworthiness, 2011, 16(4), 375-383.

Zhou, X., Zang, S.X., Wang, H., You, Z. Geometric design and mechanical properties of cylindrical foldcore sandwich structures. Thin-Walled Structures, 2015, 89, 116-130.

Zhou, C.H., Wang, B., Ma, J.Y., You, Z. Dynamic axial crushing of origami crash boxes. International Journal of Mechanical Sciences, 2016, 118, 1-12.